UNIVERSITY OF CALIFORNIA
Merced

Photo-thermal effect of carbon dispersions in water: augmenting community scale desalination with solar stills

A Dissertation submitted in partial satisfaction
of the requirements for the degree of

Doctor of Philosophy

in

Mechanical Engineering

by

Hota Venkata Soma Sai Phani Kiran

Committee in Charge:

Dr. Min Hwan Lee, Chair

Dr. Gerardo Diaz, Advisor

Dr. James Palko

Dr. Sarah Kurtz

May 2021

The Dissertation of
Hota Venkata Soma Sai Phani Kiran is approved:

Dr. Gerardo Diaz, Advisor

Dr. James Palko

Dr. Sarah Kurtz

Dr. Min Hwan Lee, Committee Chairperson

February 2021

Photo-thermal effect of carbon dispersions in water: augmenting community scale desalination with solar stills

by

Hota Venkata Soma Sai Phani Kiran

Acknowledgements

This journey was possible with selfless support from many people in my life. With Sadhguru Shirdi Sai as an eternal guide, my parents love has made me persist through some of the tough times. I would be eternally indebted to my advisor Dr. Gerardo Diaz for considering my research interests and mentoring me through this journey. I will be grateful to Dr. Edbetho Leal-Quiros for his continuous guidance. I have had the opportunity to work in high profile solar thermal research, and for that I am grateful to Dr. Roland Winston and his group. I have matured as an applied experimental researcher under the expert guidance of Dr. Lun Jiang and Dr. Bennett Widyolar, and likewise working with my colleagues from Dr. Diaz's group and Dr. Winston's group. I would like to sincerely thank Dr. Yanbao Ma, Dr. Min-Hwan Lee, Dr. Elliott Campbell, Dr. Marc Beutel, Dr. Catherine Keske, Dr. Marie-Odile Fortier, Dr. Sarah Kurtz and Dr. James Palko. I have had great friends who have supported me through this journey, I will forever be indebted to them.

Curriculum Vitæ

Hota Venkata Soma Sai Phani Kiran

Education

2014-2016	**Master of Technology** in Mechanical Engineering, specialization of Thermal Science and Engineering, National Institute of Technology (NIT) - Agartala, Agartala.
2010-2014	**Bachelor of Technology** in Mechanical Engineering, GITAM University.

Experience

2017-present	Graduate Research Assistant, University of California, Merced.
2016-2017	Teaching Assistant, University of California, Merced.
2014-2016	Graduate Research Assistant, National Institute of Technology (NIT) - Agartala, Agartala.

Publications

Journal Articles

1. **Sai Kiran Hota**, Gerardo Diaz, Activated carbon dispersion as absorber for solar water evaporation: A parametric analysis. *Solar Energy 184, 2019.*

2. ***Sai Kiran Hota***, *Gerardo Diaz, Influence of Optical Constants in Carbon-based Dispersions for Enhanced Solar Evaporation. Journal of Thermal Analysis and Calorimetry 2020*

3. ***Sai Kiran Hota***, *Gerardo Diaz, Enhancing solar water evaporation with activated carbon. MRS Advances, 5(50), 2020.*

4. ***Sai Kiran Hota***, *Gerardo Diaz, Assessment of Pyrolytic Biochar as a Solar Absorber Material for Cost-Effective Water Evaporation Enhancement. Environmental Engineering Science*

5. ***Sai Kiran Hota***, *Carlos Mata-Torres, Jose Miguel Cardemil, Gerardo Diaz, Assessing the competitiveness of nanofluid solar still for coastal locations . Desalination*

6. ***Sai Kiran Hota***, *Van Duong, Gerardo Diaz, Two Phase Flow Performance Prediction for Minichannel Solar Collectors. Heat and Mass Transfer 56, 2020.*

7. *Bennett Widyolar, Lun Jiang, Jordyn Brinkley,* ***Sai Kiran Hota***, *Jonathan Ferry, Gerardo Diaz, Roland Winston, Experimental performance of an ultra-low-cost solar photovoltaic-thermal (PVT) collector using aluminum minichannels and nonimaging optics. Applied Energy 268, 2020.*

8. *Jordyn Brinkley, Lun Jiang, Bennett Widyolar,* ***Sai Kiran Hota***, *Yogesh Bhusal, Gerardo Diaz, Roland Winston, Thermal, elec-*

trical, and cost study of advanced optical photovoltaic thermal system (ADOPTS). Applied Energy 269, 2020.

Conference Proceedings

1. ***Sai Kiran Hota**, Gerardo Diaz, Advection Diffusion Model for Particle Assisted Solar Water Evaporation. Solar World Congress, 2019.*

2. ***Sai Kiran Hota**, Julio Perez, Gerardo Diaz, EFFECT OF GEOMETRIC CONFIGURATION AND BACK PLATE ADDITION IN MINICHANNEL SOLAR COLLECTORS. Proc. of ASME Int. Mech. Engr. Congress and Exposition, 2018*

3. *Julio Perez, **Sai Kiran Hota**, Gerardo Diaz, ANALYSIS OF PHASE CHANGE THERMAL STORAGE CONFIGURATIONS FOR MINICHANNEL-BASED SOLAR COLLECTORS. Proc. of ASME Int. Mech. Engr. Congress and Exposition, 2018*

4. ***Sai Kiran Hota**, Bennett Widyolar, Jordyn Brinkley, Lun Jiang, Gerardo Diaz, Roland Winston, Experimental Performance of a Hybrid PV/T Collector. Solar World Congress, 2019.*

5. *Bennett K. Widyolar, Lun Jiang, Jordyn Brinkely, **Sai Kiran Hota**, Jonathan Ferry, Gerarod Diaz, Roland Winston, Low cost solar photovoltaic-thermal (PVT) collector using aluminum minichannels and nonimaging optics. Proc. of SPIE 2020.*

6. ***Sai Kiran Hota***, *Marie-Odile Fortier, Gerardo Diaz, Life cycle assessment of a solar still for community scale desalination. F&R Energy, 2021 (communicated).*

Abstract

Photo-thermal effect of carbon dispersions in water: augmenting community scale desalination with solar stills

Hota Venkata Soma Sai Phani Kiran

Solar stills are simple desalination systems which are capable of producing low-cost freshwater for small community requirements. But the commercialization is limited from their low daily productivity. It is expected that by adding low-cost black carbon particles, the desalination rate can be enhanced due to their photo-thermal effect.

These black carbon particles have strong solar absorption coefficient in the solar spectrum, and when used as dispersions in water, they increase the photo-thermal conversion effect which results in an increase in local fluid temperature. A higher surface temperature increases the evaporation rate due to localized heating. Experiments with biochar dispersions show that, while, the evaporation rate of water is mostly limited below 0.6 kg/m^2-h, these low-cost dispersions can increase the evaporation to more than 1 kg/m^2-h in open environments.

The influence of these particles with regards to solar still productivity and its feasibility is then assessed for community scale desalination. Solar stills are compared against photovoltaic seawater reverse osmosis (PV-SWRO) and solar

flat plate collector integrated humidification dehumidification (FPC-HDH), and found to be cost competitive for small volumes of freshwater production. The feasibility assessment of a solar still system was performed for a 10000 m^2 solar still with California as a reference location. It is estimated that freshwater can be produced at a rate of 27.7 m^3/day to 30.8 m^3/day for at least 100 households. The corresponding cost of water produced using levelized cost of water approach was found to be between \$ 6.47/m^3 and 7.14/m^3 for nominal investment. With feasible investment options, the cost of water produced can be of only \$ 1.58/m^3 to 1.74/m^3. In a supply system, the desalination cost has the major share, and if other costs such as feed intake costs, water treatment and brine disposal are to be added, the cost of water increases, but still expected to be close to marginal cost of freshwater supplied. Also, from the application standpoint, solar stills are much simpler to install, operate and maintain than other competing technologies which are more complex, thereby requiring constant supervision. The analysis performed indicates the feasibility of installing low-cost solar stills successfully in rural communities to produce low-cost freshwater.

Contents

List of Figures

List of Tables

Nomenclature

A_{abs}	Surface area, m^2
A_{sol}	Weighted solar absorption coefficient
C_p	Specific heat capaity
$D_{v,air}$	Diffusivity of vapor into air, m^2/s
d	Discount rate, %
d_p	Diamter of the particle
EE	Embodied energy, MJ
EF	Emission factor, kg $CO_{2\text{-eq}/}$kWh (MJ)
E_{out}	Annual energy out from the solar still, MJ
f_v	Volume dispersion concentration
g	Mass transfer coefficient, kg/m^2-s
H	Heat capacity, J
h	Heat transfer coefficient, W/m^2-K
h_{fg}	Latent heat of vaporization, J/kg
I_λ	Intensity of solar spectrum, W/m^2/m
K	Thermal conductivity, W/m-k
k	Absorption (attenuation) coefficient
$\dot{m}$"	Mass evaporation rate, kg/m^2-s

m_{1s}	Mass fraction at the evaporating surface
m_{1e}	Mass fraction far away from the evaporating surface
m_{hour}	Hourly freshwater productivity, kg/h
n	Refractive index/ plant life, years
P	Pressure, Pa
PVF	Present value function, years
$Q_{abs}, Q_{ext}, Q_{sca}$	Absorption, extinction, scattering efficiency
$\dot{q}$"	Heat flux, W/m^2
R	Reflectivity
RH	Relative humidity, %
r_p	Radius of the particle
T	Temperature, °C/K
t	Time, s
U	Overall heat transfer coefficient, W/m^2-K
u	Wind velocity, m/s
X	Size parameter/ salinity, g/kg (or %)
y	Depth of travel

Greek symbols

α	Absorptivity
β_{ext}	Extinction coefficient, m^{-1}
δ	Thicness, m
ϵ	Emissivity
η	Efficiency
ϵ	HDH effectiveness
λ	Incident wavelength, nm
ϕ	Net $CO_{2\text{-eq}}$ emissions abated, kg/kg
ω	Specific humidity, kg/kg
ρ	Density, kg/m^3
σ	Stefan Boltzmann constant, 5.67×10^{-8} W/m^2K^4

Abbreviations

$CAPEX$	Capital cost of the system, $
$EPBT$	Energy payback time, year
FPC	Solar flat plate collector
HDH	Humidification dehumidification system
$LCOW$	Levelized cost of water, $\$/m^3$
$LCEC$	Life cycle energy conversion

MED	Multi effect distillation
MSF	Multi stage flash
$OPEX$	Operational cost of the system, $/year
PP	Ponderosa pine biochar sample
PV-SWRO	Photovoltaic seawater reverse osmosis
SEC	Specific energy consumption, kWh/m^3
WS	Walnut shell biochar sample

Chapter 1

Introduction

Water and energy security are key for a sustainable and prosperous future. Significant ongoing efforts are transforming their production and use in an efficient and sustainable form. Moreover, the water-energy-environment nexus (WEEN) forms the basis for emerging freshwater production technologies that can benefit low-income and disadvantaged rural remote communities.

1.1 Motivation

Freshwater for human consumption and other activities such as agriculture and industrial operations is essential. The demand for drinking water is increasing, however around 97% of available water is saline, leading to water scarcity. A

recent United Nations report [1] sates that around 2 billion people live in countries with high water stress, and around 785 million people live in places with no access to drinking water. Recent estimates suggest that about 60% of the global population could face severe water scarcity [2]. This increases the need for installing desalination plants to address the increasing demand of freshwater. A number of desalination technologies with different operating principles have been developed in the past [3]. Jones et. al [1] noted that, over the last two decades, the capacity of freshwater produced from desalination plants has increased from 24.7 MMD to 95 MMD (MMD: million m^3/day) with over 15900 desalination plants in operation as of 2019, as shown in Fig. 1.1. Unfortunately, many of these technologies require high investments costs and, therefore, are inaccessible for rural communities. Thus, it is imperative to develop low-cost technologies that can produce potable water for small low-income communities.

About 60% of world's desalination plants are based on reverse osmosis (RO) technology as shown in Fig. 1.1, followed by thermal desaliantion technologies such as multi-stage flash (MSF) at 26% and then by multi-effect distillation (MED) at less than10% [4]. The cost of desalination by reverse osmosis increases with the salinity of raw water intake. The thermal technologies are preferable for very high salinity (greater than 45000 ppm) and where high feed water temperatures are

[1] https://www.un.org/sustainabledevelopment/water-and-sanitation/

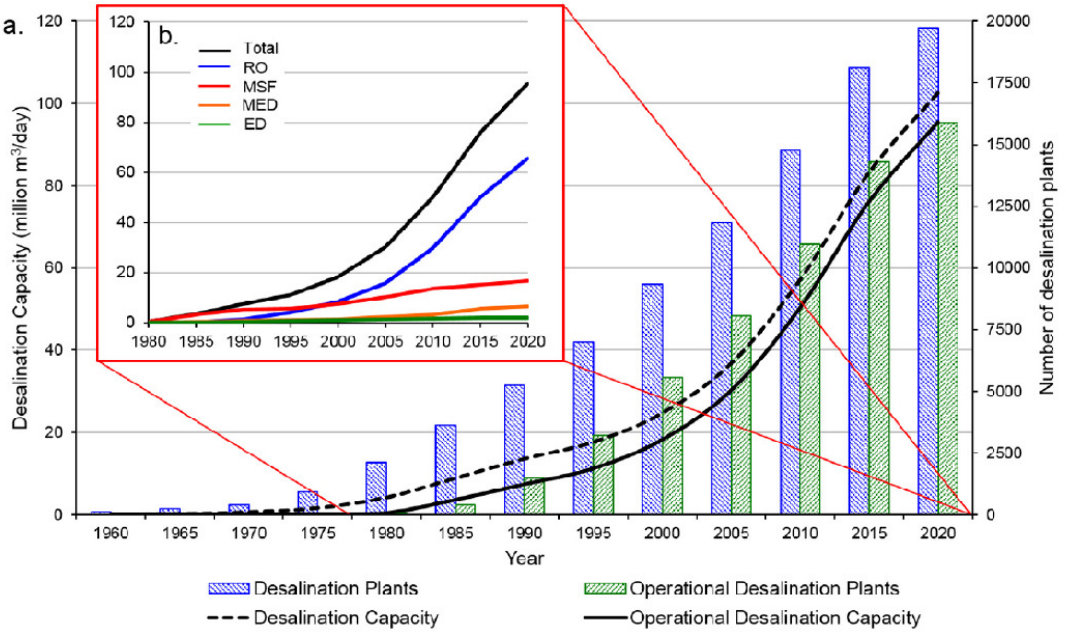

Figure 1.1: Total number of world's desalination plants and the desalination capacity [1]

involved [2]. These plants are usually installed in locations where the freshwater requirements are greater than million liters per day. Due to the high capital costs and complex operations involved [5, 6], these plants are not suitable for small community scale requirements where the demand for freshwater is much lower.

Among places that have access to water, it is observed that only a little over 50% have access to improved (safe) water sources. In these communities, freshwater requirements are typically lower than 100-200 m^3/d. Downsizing the PV-RO system or the other thermal desalination might not be feasible as they are com-

[2]https://www.advisian.com/en/global-perspectives/the-cost-of-desalination

plex systems requiring continuous supervision for maintenance, while at the same time, the economics might not justify the scale of freshwater production. With the possibility of the lack of expert supervision, any sudden maintenance in the system would potentially stop the supply of freshwater. Hence, simple desalination technologies such as solar stills which are low-maintenance systems can be easily installed for freshwater production at low costs [7]. Figure 1.2 shows a conventional single-slope single-basin solar still. A solar still is a simple desalination system that uses the concept of solar water evaporation and vapor condensation, where the sunlight transmitted through a thin condensing glass cover heats the saline water in the basin causing it to evaporate from the pool due to the absorption of solar energy. A solar still is inexpensive to produce and operate, but is limited by its applicability due to the low freshwater productivity rate, which is around 2 L/m^2-d.

A conventional approach for improving solar still productivity is to paint the basin of the solar still black. Several other advancements have been made to increase the solar still productivity for passive and active configurations: double-slope solar stills [8, 9], concentrated solar stills [10, 11], extended condenser section [12, 13], tubular and pyramid shaped solar still [14, 15], stepped solar stills with reflectors [16, 17], which have shown promise in increasing distillate productivity. Rufuss et. al have reviewed recent design and geometrical advancements in solar

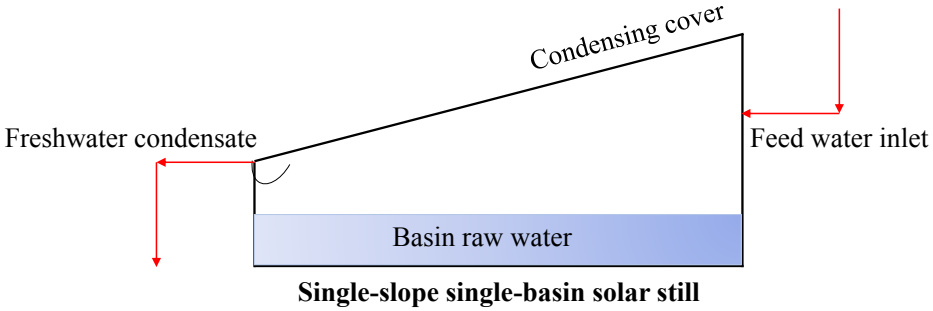

Figure 1.2: Conventional single-slope single-basin solar still

stills [18]. However, the increase in system capital often does not justify the increase in productivity and hence these improvements may not be feasible for community scale adoption.

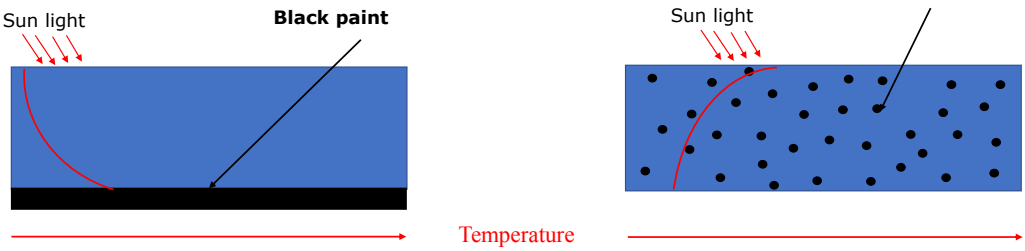

Figure 1.3: Expected water temperature profile in a solar still with black paint, and a solar still using dispersions employing photo-thermal effect

Black paint on the solar still basin is the conventional method that is widely followed for improving the productivity. However, in a solar still basin depth of 2 cm or higher, the basin is the first region that gets heated due to solar absorption and conversion to heat, leading to a temperature profile as shown in Fig. 1.3 (a). The energy is distributed within the volume increasing its temperature, and therefore, increasing the rate of evaporation. Simultaneously, the basin loses heat since its temperature is significantly higher than the environment. On the other hand, employing low-cost black carbon dispersions in water absorbs solar energy near the evaporating surface due to enhanced photo-thermal conversion resulting in a high evaporating water temperature near the surface, while the bulk volume remains at a lower temperature. This augments the evaporation rate of water from the water pool. Table 1.1 shows enhancement in distillate productivity (thermal efficiency (η_{th})) from the solar stills with these dispersions over the black-painted basin that has been observed in the literature.

Table 1.1: Enhancement of solar still performance with dispersions over black painted solar still

Type of solar still	**Basin condition**	**Reporting form**	**No dispersions**	**Dispersions**	**Gain**	**Note & Source**
Single slope	Black basin	Daily η_{still}	30%	40%	43.1%	Graphite microflakes [19]
Single slope	Black	Daily yield (ml)	665	935	29.95%	Al_2O_3 nanofluid [20]
Single slope	Black	Daily yield (ml/m^2)	4580	5400	820 ml/m^2	MWCNT [21]
Modified pyramid	Black	Daily η_{still}	50%	64.5%	14.5%	CB nanoparticle [22]
Double slope	Black	-	-	-	43.1%	MWCNT [23]
Single slope	Black	Daily productivity (ml)	531.28	798.15	50.3%	Graphite microflakes [24]

It is estimated theoretically that adding low-cost black solar absorbing materials have been found to increase the freshwater productivity considerably while keeping the system cost low. It is hypothesized that almost 66% of freshwater yield can be increased with less than 10% increase in system cost over a conventional solar still. Over a solar still with a black paint, as presented in the Table 1.1, significant freshwater productivity enhancement can be observed. Biochar and activated carbon are two such materials with an optically black appearance that can be used for strong solar absorption in solar stills. Biochar is a co-product produced after pyrolysing biomass. At just 0.1% dispersion concentration, biochar dispersion cost can be only around \$ 0.1/m^2, as compared to a black paint. The main objective of the dissertation, thereby can be summarized as, analyze the photo-thermal effect for carbon particles, such as biochar and activated carbon, in order to enhance water evaporation. This physical phenomenon can be applied for the production of freshwater using solar stills for small low-income communities. This dissertation describes the process of photo-thermal conversion with black carbon dispersions in water, analyzing the effects of optical constants, dispersion concentration and particle sizes in the context of water evaporation rate enhancement, and introduces biochar as a low-cost carbon dispersion alternative for high solar absorption. From the application point of view, with the solar stills for low-cost desalination, low-cost materials have been identified to be used as

solar still components, and the analysis showed that solar stills can be successfully installed in remote rural areas with a high population of low-income families to produce freshwater at low-costs, thereby increasing the access to safe and improved water sources in these disadvantaged communities.

1.2 Dissertation outline

Chapter 1 describes the goals and objectives of the research work.

In Chapter 2, the process of photo-thermal conversion by carbon particle dispersion in water is explained. Effects of optical constants i.e., refractive index (n) and absorption coefficient (k), dispersion volume concentration (f_v) are discussed. Since particle size parameter is sensitive to solar spectrum, three different light-scattering theories are applied accordingly. The influence of particle size with activated carbon is extensively investigated to determine the optimal size of the dispersion.

Chapter 3 discusses the increase in water evaporation rate with the enhanced photo-thermal conversion observed in Chapter 2. Theoretical heat and mass balance equations are solved to understand the process of water evaporation by adding local volumetric heat generation obtained from the solar light absorption.

Parametric influence of dispersion optical constants, particle size and ambient conditions are investigated.

In Chapter 4, biochar is introduced as a low-cost carbon rich material for application as a solar absorber for enhancing evaporation rate of water. Biochar is physico-chemically characterized and optical measurements for solar absorption are recorded. Outdoor experiments are performed to verify the enhancement in water evaporation rate with biochar.

In Chapter 5, the feasibility of solar still with dispersions as a low-cost, community scale freshwater production system is investigated in comparison to other feasible desalination technologies of solar collector integrated humidification dehumidification (FPC-HDH) and photovoltaic seawater reverse osmosis (PV-SWRO) systems. Two reference coastal locaions of Big Sur in USA (northern hemisphere) and Chañaral in Chile (Southern hemisphere) were selected for the analysis. Hourly spaced real time solar irradiation and ambient data are taken to estimate freshwater productivity theoretically by energy and mass balances, and the levelized cost of water (LCOW) approach is used to calculate the cost of freshwater.

In Chapter 6, different solar still materials combinations are investigated economically and environmentally to produce a low-cost solar still with faster energy payback time. The cost of freshwater produced in a 10000 m^2 area is calculated

as a means of providing fit-for-consumption freshwater for 100 households, with California as the reference location.

Chapter 7 summarizes the findings of the proposed dissertation. Several recommendations for future research directions are noted.

In Appendix A, all possible combinations of existing convection heat transfer and evaporation mass transfer correlations between evaporating water pool and condensing glass cover for estimating freshwater productivity rate and the system temperatures are presented against experimental data. The results for the best possible correlations combination for predicting the experimental observations for different water column depths between 1 and 10 cm are presented.

In Appendix B, life cycle assessment of a low-cost solar still system for the configuration shown in Chapter 6 is presented to determine the life cycle greenhouse gas impacts (emissions) from the system following the cradle-to-grave system boundary.

Chapter 2

Photo-thermal conversion of carbon based dispersions in water

Solar driven evaporation and steam generation which involves the conversion of the energy of photons in to thermal energy has several applications such as desalination, medical sterilization and energy storage [25, 26]. Water has good absorption properties in the near infrared (NIR) spectrum $>$ 1100 nm wavelength, but almost 80% of the solar energy is in the UV-Vis-NIR region between 300-1100 nm [27], where water is almost transparent. Hence, to enhance the photo-thermal conversion process, strong solar absorber in this range of the spectrum is needed. Photo-thermal conversion enhancers such as plasmons, semi-conductors, carbon materials and composite particles have been investigated as nanoparticle disper-

sions (nanofluids) in water and also as floating solar absorbers. Nanofluids absorb the sunlight through the fluidic volume resulting in volumetric heat generation. In the case of surface solar absorbers, solar energy is absorbed at the top surface, while the underlying water is wicked by a hydrophilic low-thermal conductivity material. Hydrophobic solar absorbers are also be used as a floating medium allowing steam generation.

While the applications of nanofluids span across several fields, the photo-thermal effect of nanofuids is also being investigated as heat transfer fluids in direct absorption solar collectors [28, 29]. Composite nanoparticles are a relatively recent discovery, hence the performance and economics are yet to be justified in its case. On the other hand, semi-conductors are limited in the band gap of electron excitation, and plasmons are limited to the peak obtained in the localized surface plasmon resonance effect (LSPR), and they are far more expensive in comparison to carbon forms of particle dispersions. Black carbon dispersions display a broadband solar absorption which can be qualitatively judged by their optically black appearance, and they are significantly more economical than other forms of possible dispersions. One comparative experiment performed by Zeiny et. al [26], showed that the cost of vapor produced by carbon black nanofluids was about 300 times lower than gold nanofluid.

2.1 Modeling approach

The process of photo-thermal conversion by these dispersions involves optical interaction of the disperison particles and the base fluid medium with the incident wavelength spectrum. Three scattering regimes are used in calculating the spectral extinction efficiency of the dispersion-fluid system based on the corresponding size parameter (X) of the particle which is the product of the wavenumber and the radius of the particle in a given medium, and is calculated as [28, 30, 31]:

$$X = \frac{2\pi n_f}{\lambda} r_p \tag{2.1}$$

Here, n_f is the base fluid refractive index (water) and r_p is the radius of the dispersion particle.

Three different scattering regimes are identified based on the particle size parameter, which explicitly calculates absorption efficiency (Q_{abs}) and scattering efficiency (Q_{sca}), and are briefly mentioned here under.

Rayleigh scattering

Rayleigh scattering is feasible for particle sizes $X \ll 1$, and was proposed by Lord Rayleigh. The absorption efficiency and scattering efficiency, can be calculated as a function of size parameter and the ratio of the complex refractive index of the dispersion particle and the base fluid ($m = \frac{n_p + ik_p}{n_f}$), where the symbol

'i' refers to the imaginary unit, $\Re$ corresponds to the real part of the complex number, and $\Im$ corresponds to the imaginary part.

$$Q_{abs} = 4X\Im\left[\frac{m^2-1}{m^2+2}\Big[1+\frac{X^2}{15}\frac{m^2-1}{m^2+2}\Big[\frac{m^4+27m^2+38}{2m^2+3}\Big]\Big]\right] \tag{2.2a}$$

$$Q_{sca} = \frac{8}{3}X^4\Re\left[\frac{m^2-1}{m^2+2}\right]^2 \tag{2.2b}$$

Mie scattering

Mie scattering is widely used for particles whose size parameter is comparable to the wavelength spectrum ($X \approx 1$). The absorption and scattering efficiency are calculated as:

$$Q_{abs} = \frac{2}{X^2}\sum_{n=1}^{\infty}(2n+1)\Re(a_n+b_n) \tag{2.3a}$$

$$Q_{sca} = \frac{2}{X^2}\sum_{n=1}^{\infty}(2n+1)(|a_n|^2+|b_n|^2) \tag{2.3b}$$

Where, a_n, and b_n are mie coefficients, which are algebraic combinations of Bessel and Henkel functions:

$$a_n = \frac{m^2 j_n(mx)[xj_n(x)]' - j_n(x)[mxj_n(mx)]'}{m^2 j_n(mx)[xh_n(x)]' - h_n(x)[mxj_n(mx)]'} \tag{2.4a}$$

$$b_n = \frac{j_n(mx)[xj_n(x)]' - j_n(x)[mxj_n(mx)]'}{j_n(mx)[xh_n(x)]' - h_n(x)[mxj_n(mx)]'} \tag{2.4b}$$

The terms $j_n(z)$ and $h_n(z)$ are spherical Bessel functions and spherical Henkel functions, respectively. Here the subscript n refers to the order and z represents the argument. The spherical Henkel function is a linear combination of spherical Bessel functions given as:

$$h_n(z) = j_n(z) + iy_n(z) \tag{2.5}$$

The spherical Bessel functions are related to the Bessel function as

$$j_n(z) = \sqrt{\frac{\pi}{2z}} J_{n+\frac{1}{2}}(z) \tag{2.6a}$$

$$y_n(z) = \sqrt{\frac{\pi}{2z}} Y_{n+\frac{1}{2}}(z) \tag{2.6b}$$

Here J_v and Y_v are Bessel functions of the first and second kind, respectively. The derivatives of the spherical Bessel functions are given as:

$$[zj_n(z)]' = zj_{n-1}(z) - nj_n(z) \tag{2.7a}$$

$$[zh_n(z)]' = zh_{n-1}(z) - nh_n(z) \tag{2.7b}$$

For order n =0, the spherical Bessel functions are satisfied by the trigonometric equations:

$$j_0(z) = \sin(z)/z \tag{2.8a}$$

$$y_0(z) = -\cos(z)/z \tag{2.8b}$$

The spherical Bessel functions are known to follow the recurrence formula given by the expression:

$$f_{n-1}(z) + f_{n+1}(z) = \frac{2n+1}{z} f_n(z) \tag{2.9}$$

To reduce the complexity of infinite series calculation, an upper limit of n_{max} is used which is given as

$$n_{max} = 2 + X + 4X^{1/3} \tag{2.10}$$

Geometric optics

Geometric optics is suitable for size parameters larger than the incident wavelengths, and usually considered if $X \gg 1$, but typically used for $X \gg 2$. The absorption and scattering efficiency are calculated as a function of reflectivity (ρ_{pref}) as:

$$\rho_{pref} = \frac{(n_p - n_f)^2 + k_p^2}{(n_p + n_f)^2 + k_p^2} \tag{2.11}$$

The absorption efficiency and scattering efficiency are then computed as:

$$Q_{abs} = 1 - \rho_{pref} \tag{2.12a}$$

$$Q_{sca} = \rho_{pref} \tag{2.12b}$$

The terms n and k refer to the refractive index and the attenuation (absorption) coefficient, respectively and the subscripts p and f stand for particle and the base fluid, which is water in this case. Some of the assumptions internalized for the use of above mentioned scattering equations are:

1. Dispersion particles are approximated as having spherical shape and are of uniform size (80 nm).

2. These dispersions are uniformly distributed through the length of the fluid container and no agglomeration at the bottom is considered.

3. Dispersion concentration is very small in comparison to the volume of fluid, that independent scattering holds valid, i.e., volume fraction $f_v \leq 0.6\%$.

4. It is assumed that the back scattering of light from the particles on the surface is negligible in comparison to the light scattering and absorption within the fluid.

The extinction efficiency (Q_{ext}) is then calculated as the summation of absorption efficiency and scattering efficiency:

$$Q_{ext} = Q_{abs} + Q_{sca} \tag{2.13}$$

2.1.1 Size limits for applying Mie scattering, Rayleigh scattering and Geometric optics

The extinction efficiency for large particles, predicted by geometric optics is $(Q_{ext})\rightarrow 2$. It is interesting to note that in the Rayleigh scattering regime, the scattering of light is very small in comparison to absorption of incident light due to the very small particle sizes, and absorption efficiency is almost close to the extinction efficiency. Scattering increases with increasing particle sizes.

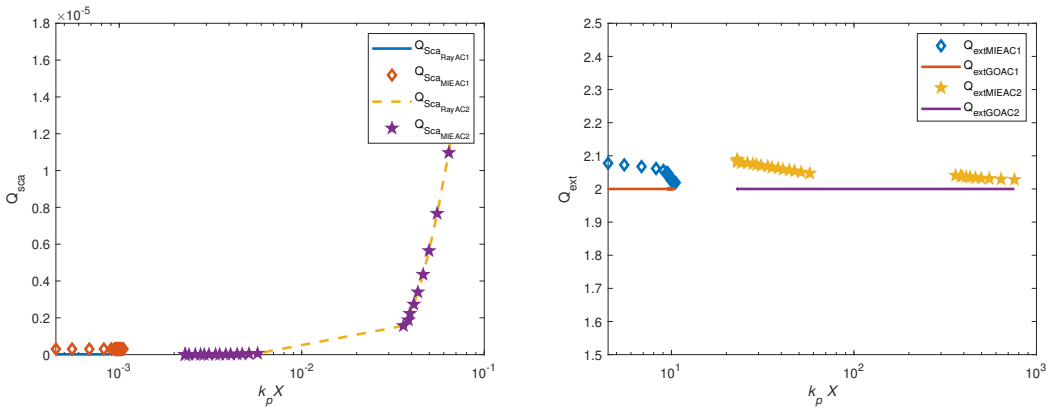

Figure 2.1: Convergence of Mie scattering with (a) Rayleigh scattering and (b) geometric optics

However, the limits for Mie theory, and also Rayleigh theory with regards to particle size is not clearly defined in literature. Hence, the convergence of Mie scattering theory with Rayleigh scattering and geometric optics was performed, to identify the usable size limits and determine the conditions for using a partic-

ular scattering theory based on the size parameter. The convergence criteria was checked for two carbon based particles i.e., activated carbon (AC1) and amorphous carbon (AC2) and is shown in Fig. 2.1.

Figure 2.1(a) shows the approximation of Mie scattering with Rayleigh scattering for smaller particle sizes, and the approximation of Mie scattering with geometric optics for large particles. For very small particle sizes (smaller than $k_p X = 10^{-3}$), Rayleigh scattering is used, and for very large particles ($k_p X > 1$), geometric optics is used. In between this range, Mie scattering is applied.

2.2 Attenuation of sunlight and solar absorption

The extinction coefficient, which indicates the spectral strength of incident light attenuation (in m^{-1}) is calculated as the function of particle extinction efficiency and the corresponding contribution from the base fluid:

$$\beta_{ext} = 1.5\frac{f_v}{d_p}Q_{ext} + (1 - f_v)\frac{4\pi k_f}{\lambda} \tag{2.14}$$

where, d_p is the particle diameter ($d_p = 2r_p$). The total light transmittance through a given depth of base fluid can be calculated from a simplified form of the Beer-Lambert law as:

$$\frac{dI}{dy} = -\beta_{ext} y \tag{2.15}$$

Here, Airmass 1.5 is used as the spectral intensity. The portion of spectral light that is attenuated through the fluid column is the light absorbed by the system, and the volumetric heat generation can be achieved by integrating the above for the given depth of solar light travel (or light penetration depth) (y). The corresponding total weighted solar absorption coefficient or solar absorption fraction (A_{sol}) is calculated as:

$$A_{sol} = \frac{\int_{\lambda_{min}}^{\lambda_{max}} I_\lambda (1 - \exp^{-\beta_{ext} y}) d\lambda}{\int_{\lambda_{min}}^{\lambda_{max}} I_\lambda d\lambda} \tag{2.16}$$

2.2.1 Influence of optical constants

Extinction coefficient for any given dispersion strength depends upon the interaction of particle and the sun light, i.e., particle's optical constants determine the strength of light extinction. Optical constants of carbon particles typically have a refractive index in the range: $1 \leq n \leq 3$, and attenuation coefficient $0.001 \leq k \leq 1$. The optical constants for some of the probable dispersion particles are shown in Fig. 2.2.

While the majority of carbon particles have refractive index (n) around 1.5, some graphitic characteristics in these particles can increase the refractive index to around 3. The spectral extinction coefficient for these two values ($n = 1.5$ and 3) for a range of absorption coefficient (k) from 0.001 to 1 is calculated and shown in Fig. 2.3 and Fig. 2.5. The spectral values for amorphous carbon, reduced

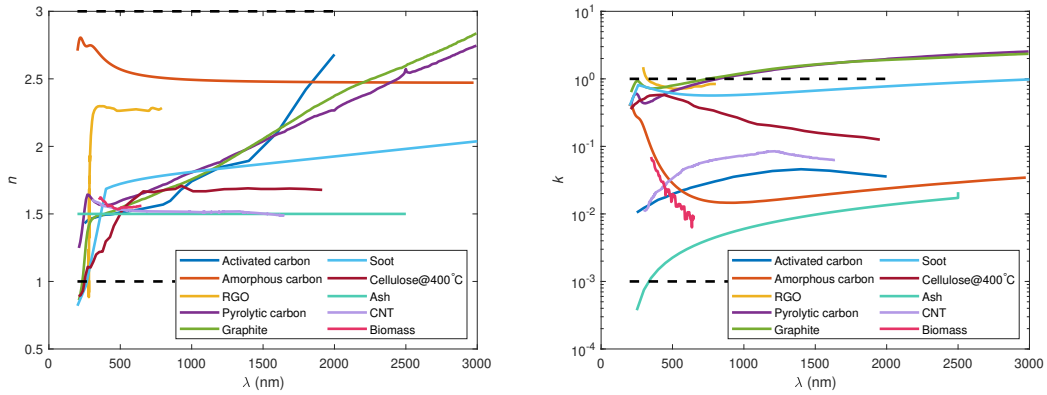

Figure 2.2: (a)The refractive index n, and (b) attenuation coefficient (k) of different carbon based dispersions and their applied upper and lower limits

.

graphene oxide (RGO), pyrolytic carbon and graphite, soot, cellulose, ash and CNT are taken from [32, 33, 34, 35, 36, 37, 38], respectively.

Figure 2.3 shows influence of optical properties on light extinction. It is verified from the figure that low absorption coefficient results in smaller light extinction coefficient. It is interesting to note that in Fig. 2.3(b), the extinction coefficient for absorption coefficients between 0.001 and 0.01 are close to one another for refractive index of 3, while for refractive index of 1.5, the curves are further apart from one another. This indicates that both refractive index and the absorption coefficient play a major role in light extinction. It is observed that in the NIR region greater than 1200 nm, the contribution of light extinction by water becomes

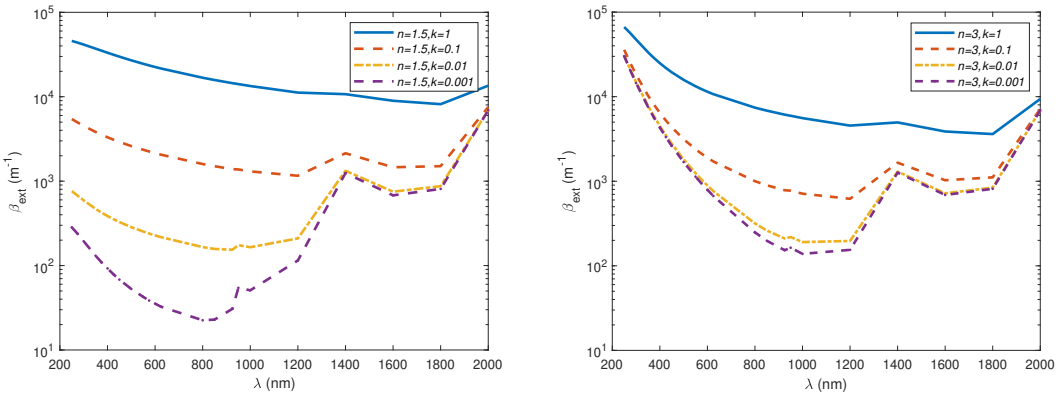

Figure 2.3: Extinction coefficient for refractive index (a) 1.5; and (b) 3

more significant and influences the overall extinction coefficient and is shown in Fig. 2.4 with activated carbon dispersions at different volume concentrations. For volume fraction of 0.1%, the extinction coefficient contribution of dispersion particles is in the same range as that of water in the solar spectrum greater than 1200 nm.

The weighted solar absorption coefficient/ solar absorption fraction (A_{sol}) is shown in Fig. 2.5. It is observed that the refractive index has a strong influence in overall light absorption fraction, especially for small absorption coefficients. At an absorption coefficient of 0.001, the solar absorption fraction is 43.15% even for a 10 mm path length, while for a 50 mm path length is 86.65% for n =1.5, while, for $n = 3$, solar absorption fraction is almost 92% for a 10 mm path length. For

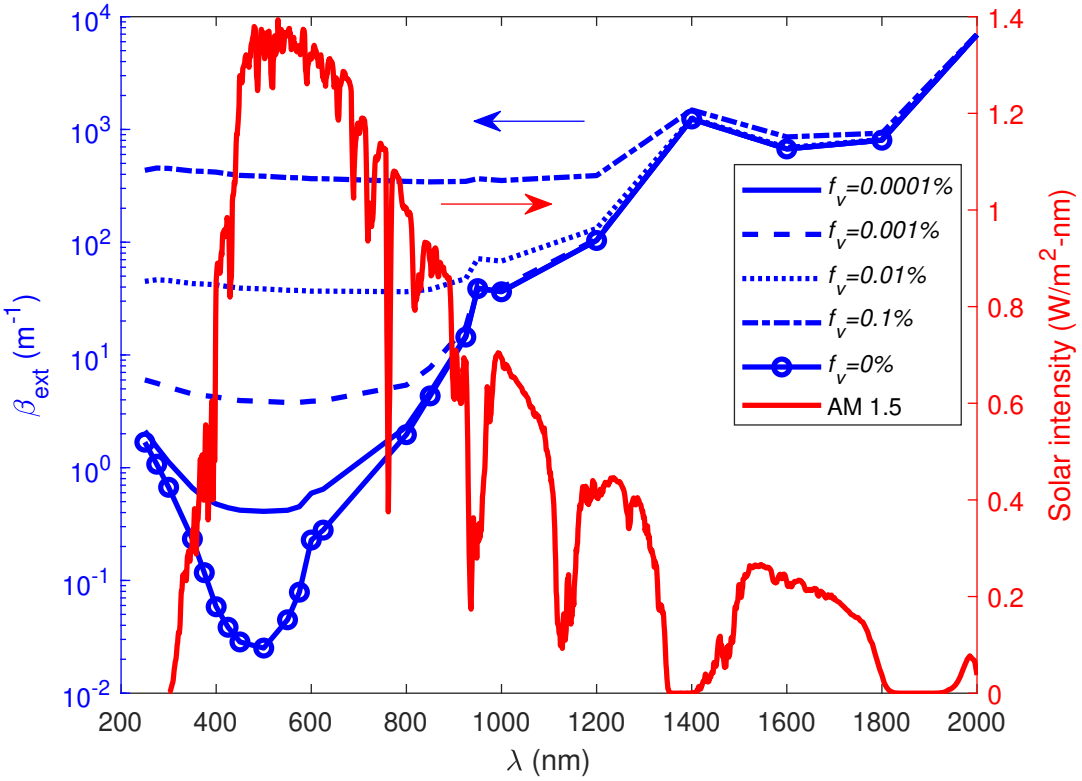

Figure 2.4: Spectral variation of extinction coefficient with volume fraction for activated carbon dispersion

k =0.01, it is observed that almost all of the sun light is absorbed within 20 mm path length for n =1.5. With larger absorption coefficients, as expected, all of the incident sun light is absorbed within 5 mm path length, resulting in a strong and intense localized heat.

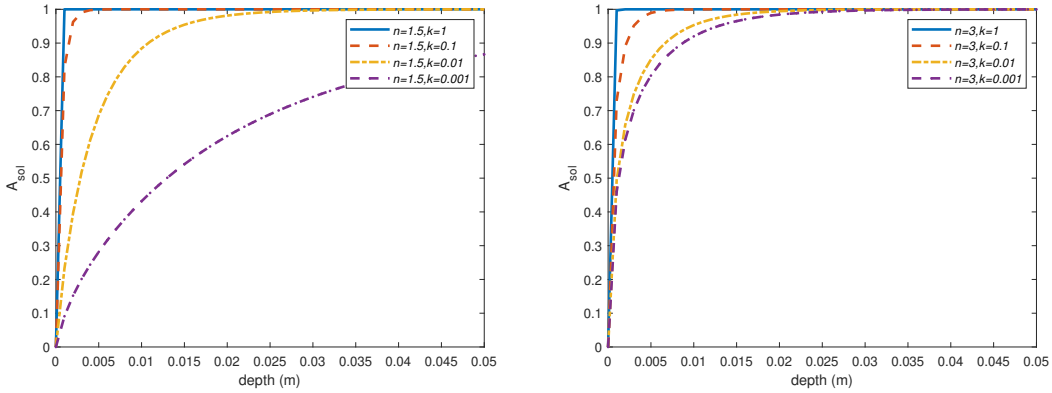

Figure 2.5: Weighted solar absorption for refractive index (n) (a) 1.5; and (b) 3

For a better understanding of light attenuation, the solar absorption fraction for a refractive index range between 1 and 3 ($\Re(m) = 0.75$ to 2.25) was calculated for a path length of 10 mm.

It is observed from Fig. 2.6 that the refractive index of the particle and that of the base fluid are the same, i.e., $\Re(m)$ =1, then the total solar absorption fraction is lower. The absorption coefficient dictates the strength of light attenuation, and thereby, the magnitude of the solar absorption fraction. The reason for the drop in solar absorption fraction is that the scattering efficiency at $\Re(m) = 1$ is very low, and therefore negligible when compared to the other values of $\Re(m)$. The incident light, passes through the particle and the base-fluid without undergoing

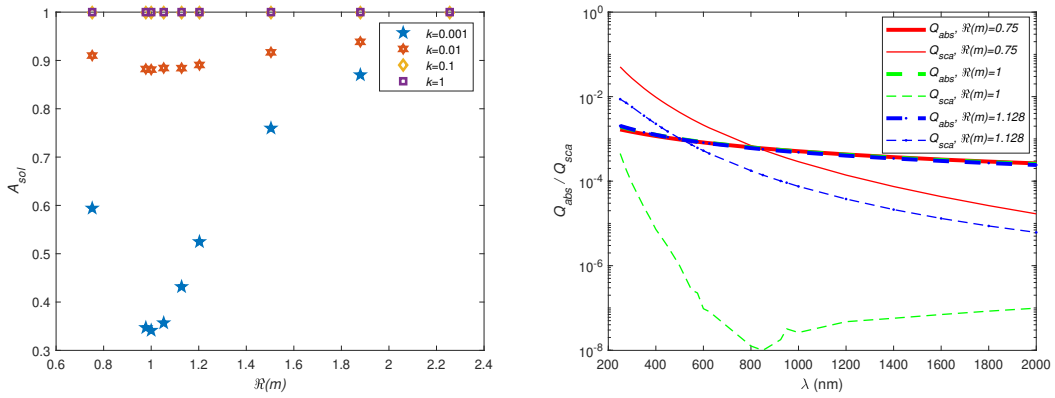

Figure 2.6: (a) weighted solar absorption coefficient for carbon dispersions in the selected range of n =1 to 3 ($\Re(m) = 0.75$ to 2.25); (b) Absorption and scattering efficiency of dispersions for $n = 1$ ($\Re(m) = 0.75$), $n = 1.33$ ($\Re(m) = 1$) and $n = 1.5$ ($\Re(m) = 1.128$)

any scattering, thereby resulting in lower extinction coefficient, and thereby lower light extinction.

2.3 Particle concentration and size effects

It is evident from Eqs. 2.14, 2.15 and 2.16 that the particle concentration i.e., volume fraction plays a major role in influencing the photo-thermal concentration. Similarly, particle size also plays a significant role in the light scattering and light extinction, as is defined by the Rayleigh scattering/ Mie scattering / Geometric optics regime. Due to the availability of optical properties, the influence of particle

concentration and size effects, were investigated for activated carbon dispersion, and it is hypothesized that the other carbon particles follow a similar trend.

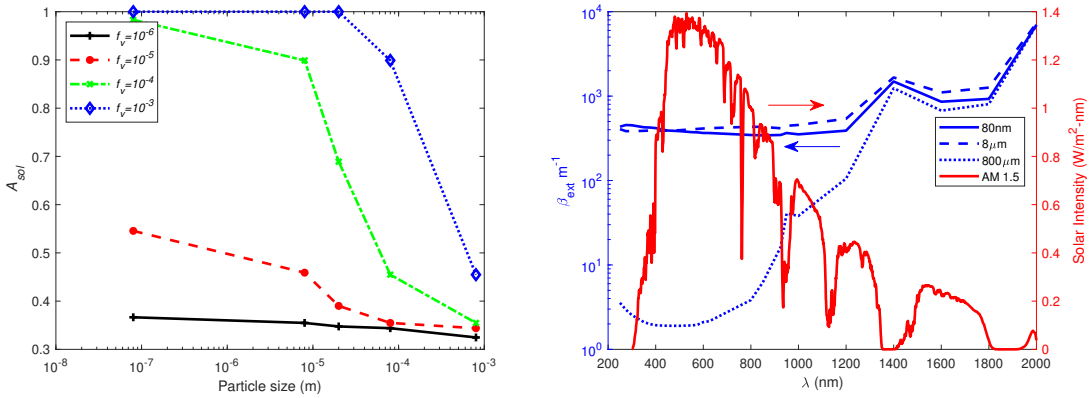

Figure 2.7: (a) Particle size and concentration effects on solar absorption fraction; (b) Extinction coefficient of 80 nm, 8 μm, and 800 μm particle dispersion at 0.1% f_v

Particle concentration and size effects of activated carbon dispersion in water are shown in Fig. 2.7. Increasing the particle concentration increases the solar absorption fraction since the extinction coefficient increases as explained previously. On the other hand, it is observed that smaller particle sizes are favorable, probably because, for a given volume concentration, the total number concentration of particles is very high in nano-sized particles in comparison to larger particles. While a volume fraction less than 10^{-4} (0.01%) is practically not useful, a smaller particle can absorb almost all of the incident sunlight at concentration higher than

0.01% as shown in Fig. 2.7(a). It is interesting to note that at 0.1% fraction, all of the sunlight is attenuated by particles smaller than 8 μm, and the solar absorption fraction decreases with increasing particle size. The reason, as shown in Fig. 2.7 (b), is that the extinction coefficient is very similar for sizes lower than 8 μm, but increasing the particle size, drastically reduces the extinction coefficient. At 800 μm (0.8 mm) dispersion size, adding particles has no apparent advantage, since the high extinction coefficient that is observed at wavelengths longer than 1200 nm is because of the base fluid (water) itself. At 0.01% volume fraction, the corresponding solar absorption fraction for 10 cm path length of light for 8 μm and 80 nm particle dispersions is 0.9 and 1, respectively. This is considered to be sufficiently strong for good photo-thermal conversion. This dispersion concentration is chosen for further analysis in the following section, and the following Chapter. 3, unless otherwise stated.

Many of these carbon particles come in granular sizes, and crushing the particles to smaller sizes increases the cost of the particle. Hence, the crushing energy (work) potential from granular size to powder sizes is calculated according to the equations mentioned in [39]. The cost of the crushed particle is proportional to this work potential.

Figure 2.8 shows the variation of solar absorption coefficient, and crushing work potential for varying particle sizes. It is observed that the work potential

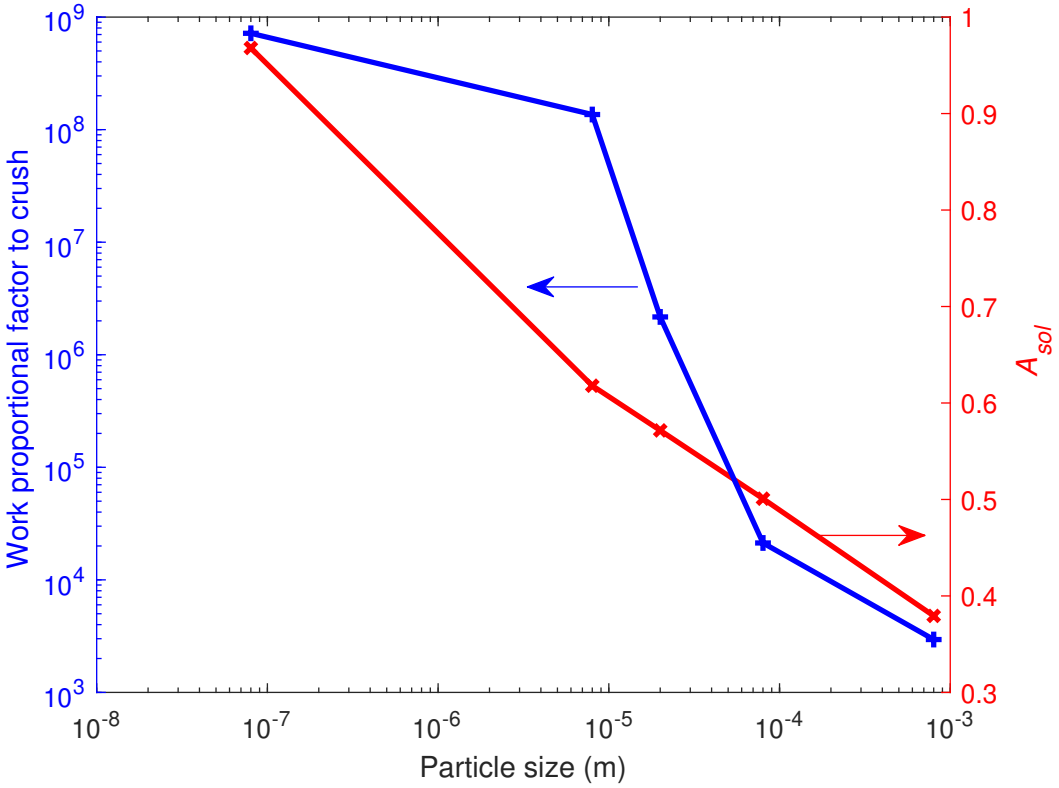

Figure 2.8: Solar absorption fraction and crushing work potential for different particle sizes

needed to crush to micron size of 8 μm is small, while a strong photo-thermal conversion with solar absorption fraction of 0.9 can be obtained. Crushing to even smaller sizes has a smaller gain in solar absorption fraction, while work crushing energy, and thereby the cost increases significantly. Hence, it can be expected that 8 μm size of activated carbon dispersion is sufficient to have a strong photo-thermal conversion with relatively smaller costs in comparison to

nanoparticles. In qualitative terms, it is sufficient to have particle in micrometer or sub-micrometer sizes for superior performance and cost benefits.

2.4 Highlights

- Black carbon particle dispersions augment the photo-thermal conversion due to its desirable optical properties in the solar spectrum.
- Total solar absorption fraction depends on the depth of light penetration, and for any given dispersion particle increases with the dispersion concentration.
- It is identified that if the refractive index of the dispersion particle is the same as that of the base fluid, then the total solar absorption fraction is relatively far lower than for other particle refractive index values because light almost passes through the particle without scattering.
- For a given dispersion concentration, smaller particles absorb the sunlight more effectively over larger particles, and thus, are more desirable.

Chapter 3

Evaporation enhancement of water due to carbon dispersions

Water evaporation from liquid pool occurs due to vapor concentration difference between the evaporating surface and the immediate vicinity, analogous to temperature difference. Vapor concentration difference in mass transfer terms can be modeled as vapor pressure difference by assuming ideal gas laws. At low temperatures, Fick's law of diffusion is applied, while at higher temperatures (T>60°C), advection form of vapor transport dominates the diffusion phenomenon [40]. The differential form of mass transfer process is given as [41]:

$$\dot{m}" = -\frac{\rho D_{v,air}}{1 - m_{1,s}} \frac{dm_1}{dy}\bigg|_{y=0} \tag{3.1}$$

Where, ρ is the average gas density, $D_{v,air}$ is the vapor-air diffusivity and $m_{1,s}$ is water vapor mass fraction at evaporating surface. The enhancement of water evaporation rate in the presence of carbon dispersions will be discussed in the following sections.

3.1 Volumetric heat generation

It was shown in Chapter 2 that adding particle dispersions increases the strength of solar light attenuation. This increase in solar light attenuation increases the volumetric heat generation ($\dot{q}'''_{gen}$) within the fluid column for the depth of light travel.

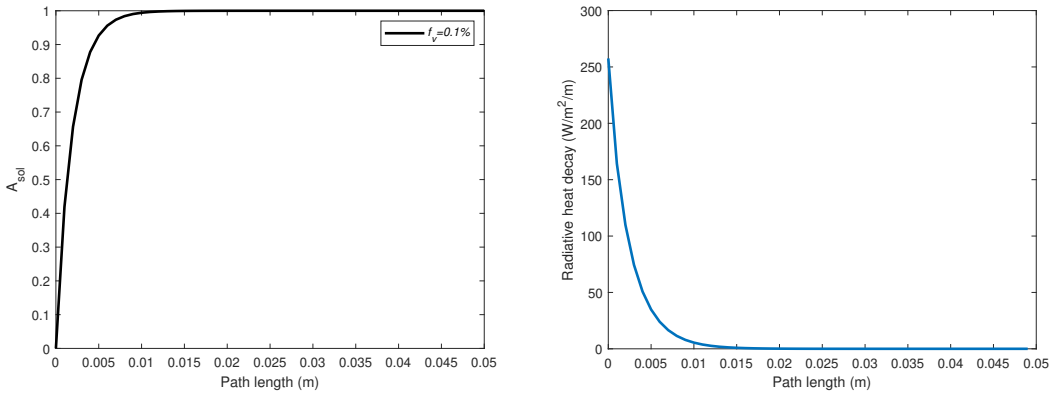

Figure 3.1: (a) Solar absorption coefficient and corresponding (b) volumetric heat generated by 0.1% f_v activated carbon dispersions

The solar absorption coefficient and the corresponding volumetric heat generated are related directly with the strength of light extinction coefficient and the depth of travel. The volumetric heat generated within the fluid column depth for the path travel is obtained by spectrally integrating Eq. 2.15 over the entire wavelength spectrum, and thereby the solar absorption fraction and the volumetric heat generated can be related according to [28]. Figure 3.1 shows the corresponding variation in solar absorption fraction and volumetric heat decay with increasing column depth of fluid at 0.1% f_v activated carbon nanoparticle disperision. It is observed that near the surface, substantial radiative heat energy potential is available since light has not been attenuated yet. After passing through a certain depth of fluid column, solar absorption of light increases and more volumetric heat is generated. After 10-12 mm of depth of light travel, all of the sun light is absorbed, i.e., A_{sol} is 1. This corresponds to no more light energy being available, hence, radiative heat energy generated is zero after 12 mm of fluid column depth. This absorbed energy is the volumetric heat that is generated in the dispersion-fluid system, and is responsible for increasing the fluid temperature. This raise in temperature augments the vapor difference concentration by increasing the evaporating mass fraction ($m_{1,s}$) and thereby, enhance the evaporation rate of water. The following sections will discuss the evaporation rate enhancement of water based on heat and mass balance equations.

3.2 Modeling approach

The governing equations for heat and mass transfer are given as:

1. Top boundary

$$A[\dot{m}'' h_{fg,w}] = A[K_{nf}\frac{dT}{dy} + \dot{q}''_{conv} + \dot{q}''_{rad} + \dot{q}''' y] \tag{3.2}$$

2. Bulk Volume

$$\rho_{nf} C_{p,nf}\frac{\partial T}{\partial t} = K_{nf}\frac{\partial^2 T}{\partial y^2} + \dot{q}''' \tag{3.3}$$

Where, $\dot{m}''$, $h_{fg,w}$ are the water evaporation rate and latent heat of vaporization of water. K, ρ and C_p are the thermal conductivity, density and specific heat capacity, respectively of the nanofluid (subscript 'nf').

The nanofluid thermo-physical properties are computed according to the relations in [42, 43]:

$$\rho_{nf} = f_v\rho_{np} + (1 - f_v)\rho_w \tag{3.4a}$$

$$C_{p,nf} = f_v C_n p + (1 - f_v)C_{p,w} \tag{3.4b}$$

$$\frac{K_{nf}}{K_w} = \frac{2K_w + K_{np} + 2f_v(K_{np} - K_w)}{2K_w + K_{np} - f_v(K_{np} - K_w)} \tag{3.4c}$$

$$h_{fg,nf} = \frac{\rho_w h_{fg,w}(1 - f_v)}{\rho_{np}} \tag{3.4d}$$

The radiation heat transfer between the water at the surface and the ambient is due to long wave emission of water with emissivity of (ϵ_w) 0.96 [44], and is

calculated as:

$$\dot{q}''_{rad} = \epsilon_w \sigma (T^4_{surf,K} - T^4_{\infty}) \tag{3.5}$$

Where, T_∞ is the surrounding ambient temperature is Kelvin.

3.2.1 Convection-evaporation similarity equations

The convection and surface water evaporation governing equations can be generalized as following Newton's law of cooling in terms of convection heat transfer coefficient (h_{conv}) and mass transfer conductance (g_m). The governing differential form of mass transfer equation Eq. 3.1 can be related to g_m using dimensionless Sherwood number (Sh) which is analogous to Nusselt number (Nu). Nusselt number can be computed as a function of dimensionless Grashoff number (Gr) and Prandtl number (Pr), which are based on thermo-physical properties of the evaporating vapor and the existing temperature difference. Likewise, the Sherwood number is a function of the Grashoff number and Schmidt number (Sc), and can be calculated based on the thermo-physical properties of evaporating vapor and existing concentration (mass fraction) difference. Tables 3.1 and 3.2 summarize the sequence of calculating the convective heat transfer coefficient and mass transfer coefficient respectively.

Table 3.1: Heat transfer similarity equations

Dimensionless number [45]	$Nu = (Nu_{free}^n + Nu_{forced}^n)^{1/n}$ n=4
Free condition [45]	Nu_{free}= $\begin{cases} 0.54(Gr_tPr)^{1/4} & \text{if } Gr_tPr < 2\times10^7 \quad \text{Laminar free} \\ 0.14(Gr_tPr)^{1/3} & \text{otherwise} \quad \text{Turbulent free} \end{cases}$
Forced Condition[46]	Nu_{forced}= $\begin{cases} 0.332Re^{1/2}Pr^{1/3} & \text{if } Re < 3\times10^5 \quad \text{Laminar forced} \\ 0.036Re^{0.8}Pr^{1/3} & \text{otherwise} \quad \text{Turbulent forced} \end{cases}$
Grashoff number (Gr)	$Gr_t = \frac{\Delta T\beta_T g L_c^3}{\mu^2}$ $\beta_T = 1/T_{film}$
Gradient	$T_{surf} - T_\infty$

Table 3.2: Mass transfer similarity equations

Vapor-air diffusivity	$D_{v,air} = 1.97\times10^{-5}[\frac{T_1(K)}{256}]^{1.685}$ [44]
Dimensionless number [45]	$Sh = (Sh_{free}^n + Sh_{forced}^n)^{1/n}$ n=2
Free condition [45]	Sh_{free}= $\begin{cases} 0.54(Gr_mSc)^{1/4} & \text{if } Gr_mSc < 2\times10^7 \quad \text{Laminar free} \\ 0.14(Gr_mSc)^{1/3} & \text{otherwise} \quad \text{Turbulent free} \end{cases}$
Forced Condition[46]	Sh_{forced}= $\begin{cases} 0.664Re^{1/2}Sc^{1/3} & \text{if } Re < 5\times10^5 \quad \text{Laminar forced} \\ 0.036Re^{0.8}Sc^{1/3} & \text{otherwise} \quad \text{Turbulent forced} \end{cases}$
Grashoff number (Gr) [40]	$Gr_m = \frac{(\Delta\rho/\rho)gL_c^3}{\mu^2}$ $\Delta\rho = \rho_e - \rho_s$ $\rho = Avg(\rho_e, \rho_s)$ $\rho_{s(e)} = \rho_{s(e),1} + \rho_{s(e),2}$ $\rho_{s,1} = P_s(T_1)/R_vT_1$ $\rho_{s,2} = (P_{tot} - P_s(T_1))/R_{air}T_1$ $\rho_{e,1} = RHP_s(T_{amb})/R_vT_{amb}$ $\rho_{s,2} = (P_{tot} - RHP_s(T_{amb})/R_{air}T_{amb}$
Gradient	$m_{1,s} - m_{1,e}$ $m_{1,s} = \rho_{1,s}/\rho_s$ $m_{1,e} = \rho_{1,e}/\rho_e$

The heat transfer coefficient and mass transfer conductance are calculated as:

$$h_{conv} = Nu\frac{k_n f}{L} \tag{3.6a}$$

$$g_m = Sh\frac{\rho D_{v,air}}{L} \tag{3.6b}$$

The surface mass transfer rate i.e., evaporation rate of water is given as:

$$\dot{m}" = g_m(m_{1,s} - m_{1,e}) \tag{3.7}$$

3.3 System consideration

The geometry of the system considered in this analysis is shown below in Fig. 3.2.

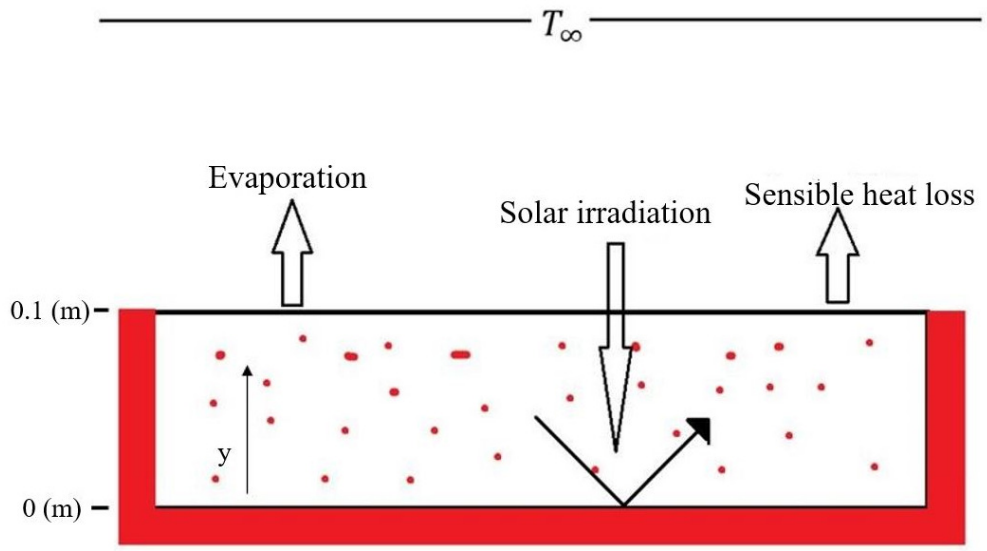

Figure 3.2: System under consideration

A unit surface area with 10 cm depth of water is considered with carbon particle dispersions. The bottom is considered to be purely reflective to increase the depth of solar light penetration in the case of low dispersion concentrations. The bottom and side walls are assumed to be insulated so as to restrict heat loss.

The ambient temperature is considered to be 21°C, and the relative humidity is 50%. The system initial temperature is considered to be the same as the ambient temperature.

Modeling scheme

The governing equations presented above are discretized into finite nodes and solved using unconditionally stable finite difference implicit scheme. The time taken to evaporate a volume of water within a small depth, equal to the node size is calculated, and the time is updated with every iteration. In each time step, the depth of fluid in the column is recalculated and after using the photo-thermal conversion schemes, the volumetric heat generated in each node is obtained. The following assumptions are used in the computations:

- The incident solar light does not undergo any interaction with the ambient environment.
- The ambient conditions, such as ambient temperature, wind velocity and relative humidity are maintained constant.
- Since the rate of evaporation alone is being estimated and no condensing cover is considered, the relative humidity is less than 100%.

- Under 1 sun condition, fluid temperature does not exceed 60°C, and hence, low mass transfer rate theory is employed by using Fick's law of diffusion.

3.4 Model validation

The validity of the selected model is performed by comparing against existing experimental results for silicon based nanofluids by Ishii et. al [47]. They observed evaporation enhancement of water for an average particle size of 80 nm at 21.4±0.2°C ambient temperature and 41±1% relative humidity.

Figure 3.3 shows the results of the numerical model against experimental observations for varying volume concentrations of silicon nanoparticles. It can be observed that for $f_v > 10^{-5}$, the simulations compare well with the experimental results. As explained, the model assumes a uniform size, and equal distribution of the nanoparticles along the fluid column, and this might have contributed to some deviations with respect of experimental results.

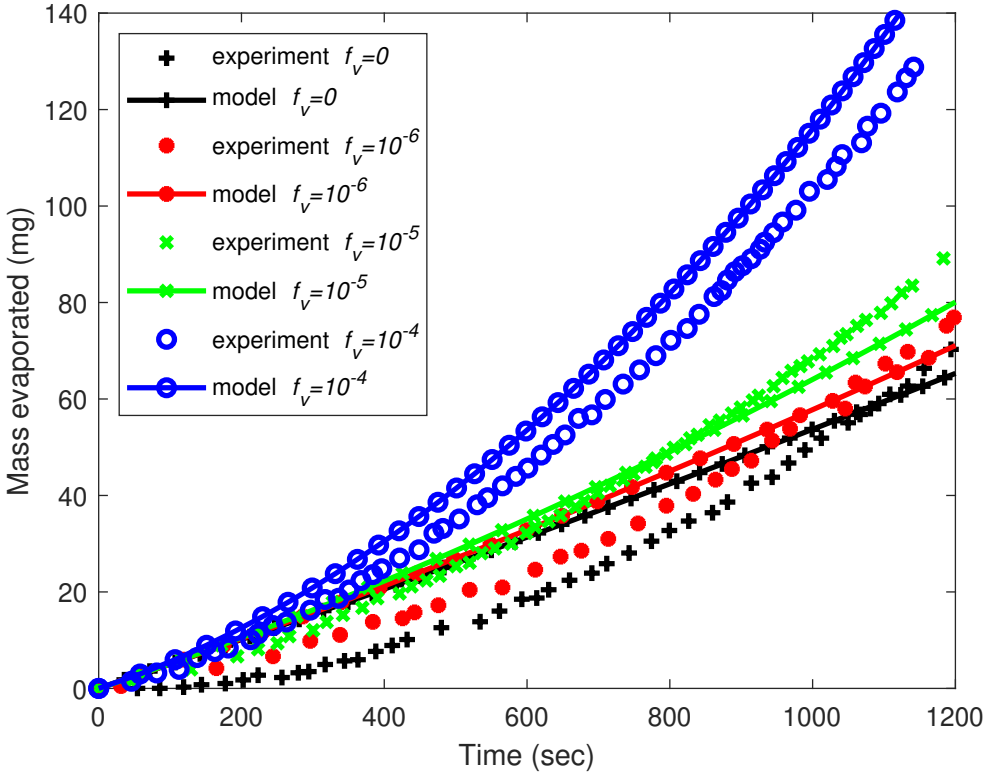

Figure 3.3: Validation of the numerical code

3.5 Influence of carbon dispersion in evaporation of water

The influence of changing the dispersion concentration and size of the particles with regards to light attenuation is already discussed in Chapter 2. The result of increasing light attenuation raises the temperature of the fluid and thereby enhancing the evaporation rate of water.

3.5.1 Evaporation enhancement with activated carbon dispersions

Effect of seeding particles

Firstly, the effect of seeding activated carbon particles (adding dispersions) for two different sizes, 80 nm and 8 μm at 0.01% volume fraction is verified with regards to the increase in the evaporation rate of water.

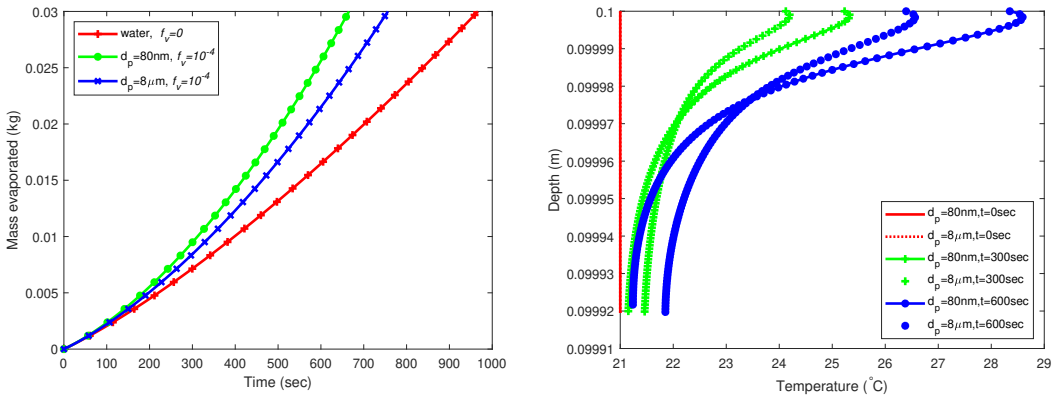

Figure 3.4: (a)Effect of particle seeding, and (b) corresponding variation of fluid temperature during evaporation process

It is observed from Fig. 3.4 that seeding with activated carbon particles, even at a small concentration of 0.01% has a pronounced effect in increasing evaporation rate of water. Since, the A_{sol} of 8 μm particle is slightly lower than that of 80 nm particle, the nanoparticle, comparatively has the best potential among the three choices followed by the microparticle. The corresponding evaporation

enhancement rate for the nanoparticle and the microparticle is 57.3% and 38.2%, respectively. Figure 3.4 (b) shows the temperature profile of the fluid (water) along the depth of the container at 300 s and 600 s, during the evaporation process. It shows that, with time, the temperature of the fluid increases, and after the transient effects, the system temperature reaches uniformity. The small dip of temperature at the top node likely indicates that the evaporating surface experiences heat losses, and hence it's temperature is slightly lower than the immediate node below. A sharp curve can be expected as the concentration fraction increases, which also happens, as water evaporates.

Particle size effect on water evaporation

It was shown earlier in Chapter 2 , Section 2.3 that the particle size influences the light extinction, and thereby it affects the solar absorption fraction for any given concentration. This influences the evaporation rate of water.

Figure 3.5 further attests the influence of particle size on water evaporation rate in accordance to Fig. 2.7 (a). Since the solar absorption fraction decreases as the particle size increases in the dispersion, then the effect of adding larger particles as dispersions in water effectively decreases the evaporation rate enhancement. Smaller particles evaporate faster, and have pronounced effect in evaporation enhancement of water.

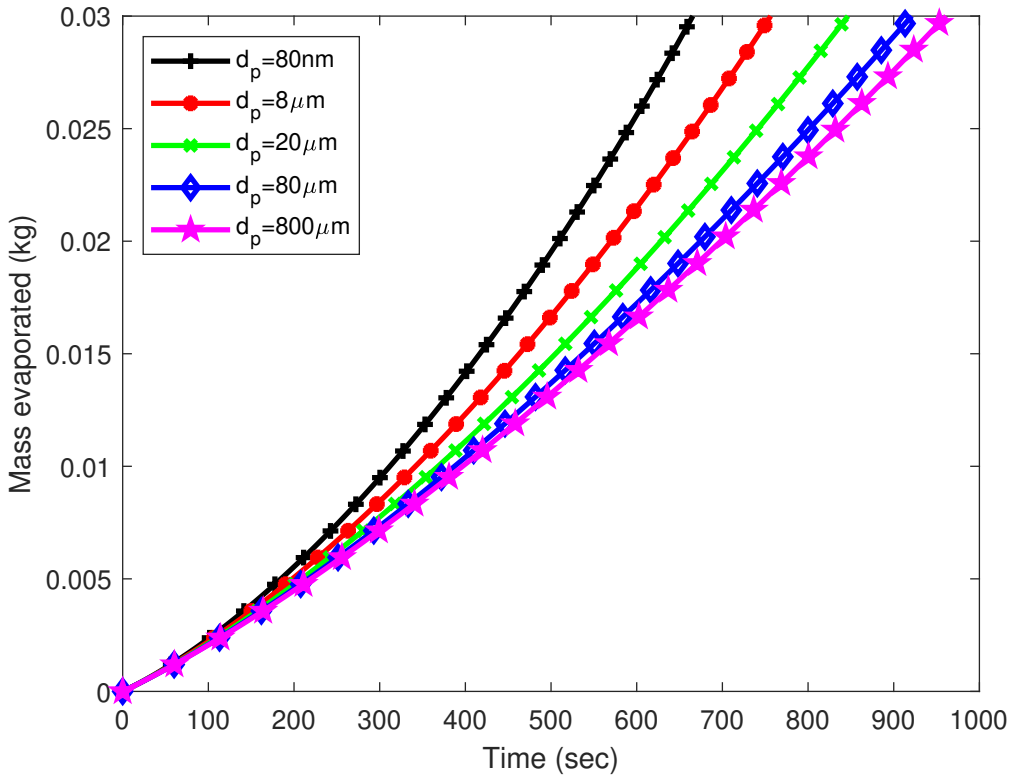

Figure 3.5: Effect of particle size on evaporation of water

Effect of dispersion concentration

Two particle sizes, i.e., 80 nm and 8 μm are considered in order to understand the influence of varying dispersion concentration in augmenting the evaporation rate of water. The volume fraction is varied from 10^{-6} to 10^{-3} (or 0.0001% to 0.1%) for the chosen conditions.

Figures 3.6 (a,b) show the influence of varying dispersion concentration in increasing fluid surface temperature and the evaporation rate of water. It is observed

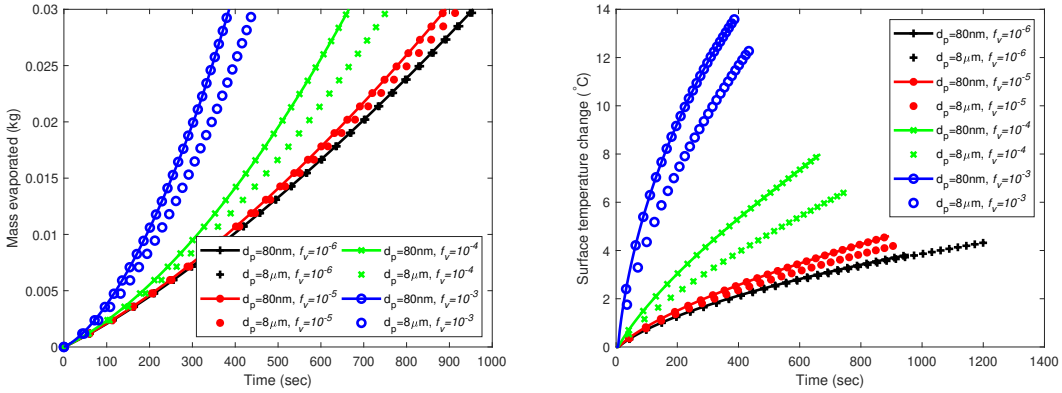

Figure 3.6: (a)Influence of dispersion concentration on evaporation of water, (b) corresponding change in surface temperature

that at volume fractions below 0.001% ($f_v = 10^{-5}$), the evaporation enhancement rate is negligible when adding activated carbon particles. The observed increase in water evaporation rate is less than 10% in comparison to pure water. Increasing the dispersion concentration above 0.01% significantly increases the evaporation rate due to significant increase in solar absorption fraction. The surface temperature is predicted to increase by almost 8°C and 6.5°C for 80 nm and 8μm particle dispersion, respectively. Further increasing the concentration to 0.1%, increases the relative evaporation rate of water by 70% over a 0.01% concentration. The increase in surface temperature is as much as 13.6°C and 12.4°C, respectively for the nanoparticle and microparticle. It is observed that the weighted solar absorption fraction is 1 at this volume fraction.

This significant improvement in evaporation rate of water is due to intense heat localization of absorbed sunlight generated by the particle dispersions.

3.5.2 Influence of optical constants on evaporation rate of water

The influence of optical constants on the evaporation rate of water, and evaporation efficiency is investigated. The evaporation efficiency (η_{evap}) is calculated as [48]:

$$\eta_{evap} = \frac{\dot{m}''[C_{p,nf}\Delta T + h_{fg,w}]}{IA_{abs}} \tag{3.8}$$

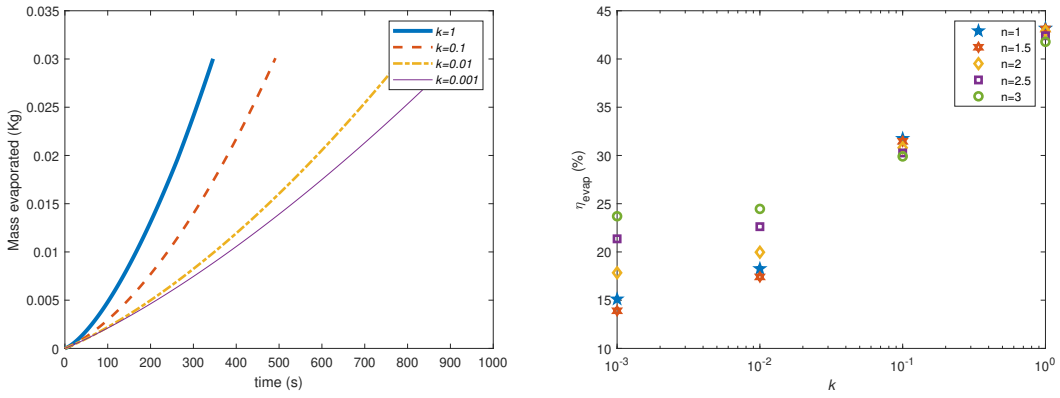

Figure 3.7: (a)Influence of absorption coefficient on evaporation of water at n =1.5; (b) Combined influence of optical constants n and k

Firstly, at n =1.5, the influence of absorption coefficient (k) on evaporation of water is determined, and shown in Fig. 3.7(a). It is observed that a higher absorption coefficient is needed for stronger evaporation of water, and this is evident from strong solar absorption fraction, as observed previously in Fig. 2.5. The times taken to evaporate 30 ml of water are 500 s and 345 s for k =0.1 and k =1, respectively, which are shorter than for pure water (968 s). At very low absorption coefficient of k =0.001, the time taken for evaporation is about 800 s, which is only about a 17.3% of enhancement compared to pure water. Figure 3.7(b) shows the combined influence of optical constants n and k on the evaporation efficiency of water, from n =1 to n =3, and k =0.001 to k =1. With no dispersion, the evaporation efficiency was found to be close to 10%. At low values of k, the evaporation efficiency for higher refractive index is almost 20-24%, while it is lower for smaller refractive index values. For larger attenuation coefficients, the evaporation efficiency increased, but the corresponding increase has comparatively lower gradient than those with lower refractive index. At k =1, the evaporation efficiency is around 43%.

Parametric influence of dispersion concentration

The influence of the variation of dispersion concentration with respect to optical constants is shown in Fig. 3.8. In addition, experimental studies involving

graphene oxide (GO) nanoparticles (at 1.5 suns) [49], reduced graphene oxide (RGO) nanoparticles (at 5 suns) [50], carbon nanotubes (CNT) (at 10 suns) [51], carbon black (CB) nanoparticles (at 11 suns) [52] and the simulated performance for activated carbon have been included for clarity.

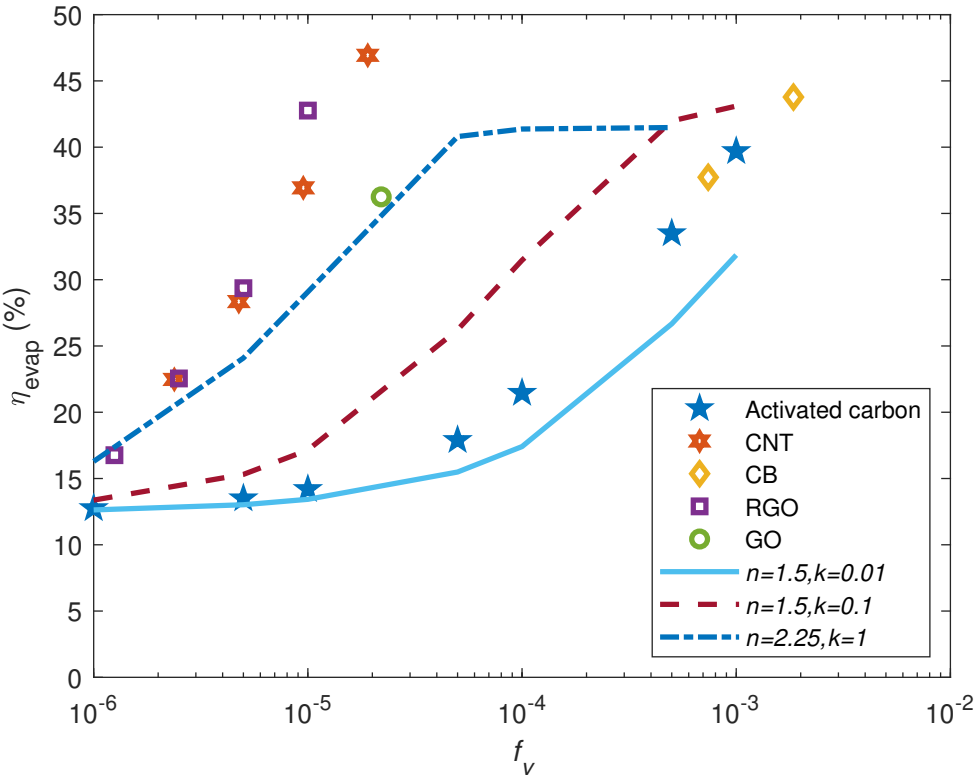

Figure 3.8: Influence of dispersion concentration on evaporation efficiency of water along with experimental data points for CNT, CB, RGO and GO nanofluids

Results for two specific refractive indexes of n =1.5 and n =2.25 are shown here in Fig. 3.8 since the above specific nanoparticles have refractive index values

close to 1.5, except for graphene nanoparticles which is close to 2.25. It is to be noted that the sizes of particles in experiments are different from the prediction model, and also particles in the experiments were not perfectly spherical. In addition, experimental illumination condition, ambient temperature and relative humidity vary with respect to the values used in the simulations. It is observed that increasing the dispersion concentration enhances the evaporation efficiency, and reaches a certain constant value, beyond which, additional concentration does not necessarily influence the evaporation performance. At very high localized heat, there exists a very thin layer of fluid that absorbs all the sun light. To limit the analysis to remain within the independent scattering limits, dispersion concentration in this study is limited to 0.1%. It is also observed observed that, at a nominal volume fraction between 0.01-0.1%, near constant evaporation efficiency can be obtained, for considerably high absorption coefficient.

3.5.3 Parametric influence of ambient conditions

The parametric influence of ambient conditions such as wind velocity, relative humidity, and ambient temperature is investigated. In this section, one parameter is changed at a time, while the rest are kept constant.

Influence of wind velocity and relative humidity

Forced convection from wind is considered here to estimate the evaporation rate enhancement in water. A small departure in wind condition, and relative humidity are considered as parametric influences.

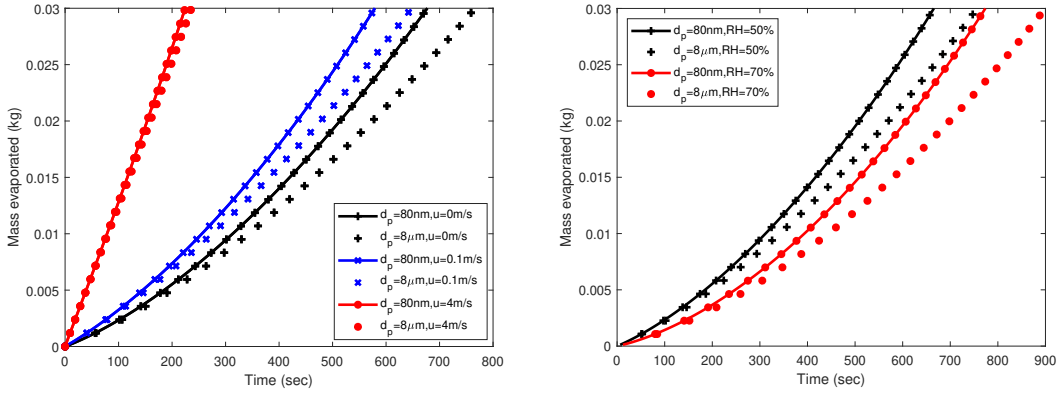

Figure 3.9: Parametric influence of (a) ambient wind velocity and (b) relative humidity on evaporation rate of water

The departure from free convection represents a forced convection scenario, and its effects are shown in Fig. 3.9(a). At higher wind loads, it is observed that the evaporation rate of water increases. Even with a small wind load of 0.1 m/s, the time for evaporating 30 ml of water decreases to 668 s with nanoparticle dispersion and to 774 s with microparticle. At higher wind load of 4 m/s, the time taken reduces from 677 sec at 0 m/s wind load to 227 s with nanoparticle, and for 8 μm, it reduces from 767 s to 234 s. On the other hand, increasing the relative

humidity from 50% to 70% has an opposite trend, as shown in Fig. 3.9(b). The time taken to evaporate water increases to 773 s for 80 nm nanoparticle, and to 901 s for 8 μm microparticles. This occurs because higher relative humidity reduces the moisture carrying capacity of air, and thereby, reduces the evaporation rate of water.

Influence of system temperature

It can be anticipated that warmer fluid temperature increase the evaporation rate. The time for evaporating water is numerically determined here. For low temperature analysis, the initial temperature is assumed to be at 21°C, 25°C and 30°C, respectively. Evaporation rate for high temperature fluid is shown considering system at 40°C and 50°C.

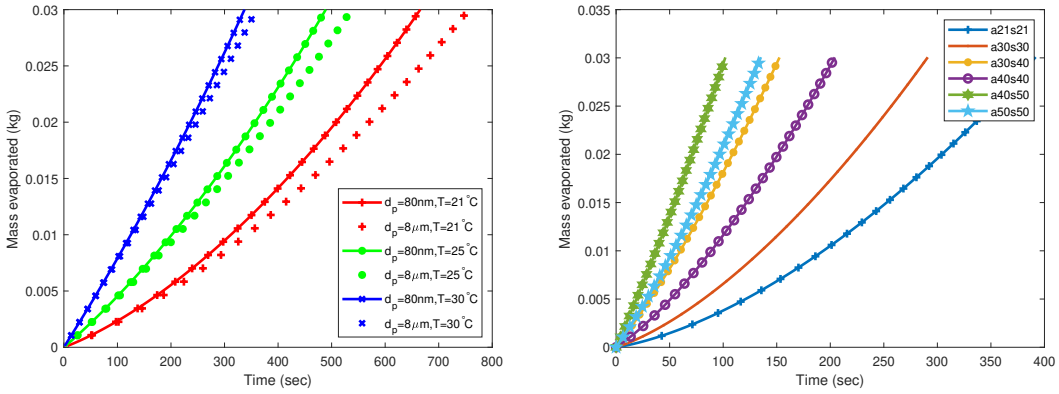

Figure 3.10: Parametric influence of (a) low system temperature and (b) influence of very high fluid temperature

Figure 3.10(a) shows the influence of having the system at 21°C, 25°C and 30°C, respectively, with both ambient and the fluid being at the same temperature. As expected, warmer fluid evaporates faster since the mass fraction of evaporating vapor increases significantly. At 25°C, the time taken for evaporating water is approximately 500 s and at 30°C, it is close to 360 s. At very high temperature, advection starts dominating, but is significant at temperatures above 60°C. However, to capture the combined effects of advection and diffusion, high mass transfer model is adopted to predict the evaporation rate of water at 40°C and 50°C. In the legend, 'a' means ambient temperature, and 's' means fluid initial temperature. It is observed that at higher temperatures, the time taken for evaporating 30 ml of water is reduced significantly, being 100 s.

3.6 Steady state evaporation of water

The simulation for predicting steady state evaporation enhancement rate of water under the solar spectrum for pure water and for activated carbon dispersions at 0.1% concentration was performed for 1 hour and is shown below in Fig. 3.11.

It is observed from Fig. 3.11 that the evaporation rate of water due to efficient photo-thermal conversion of nanoparticle dispersions is much greater than for just pure water which has poor photo-thermal conversion property. For pure water,

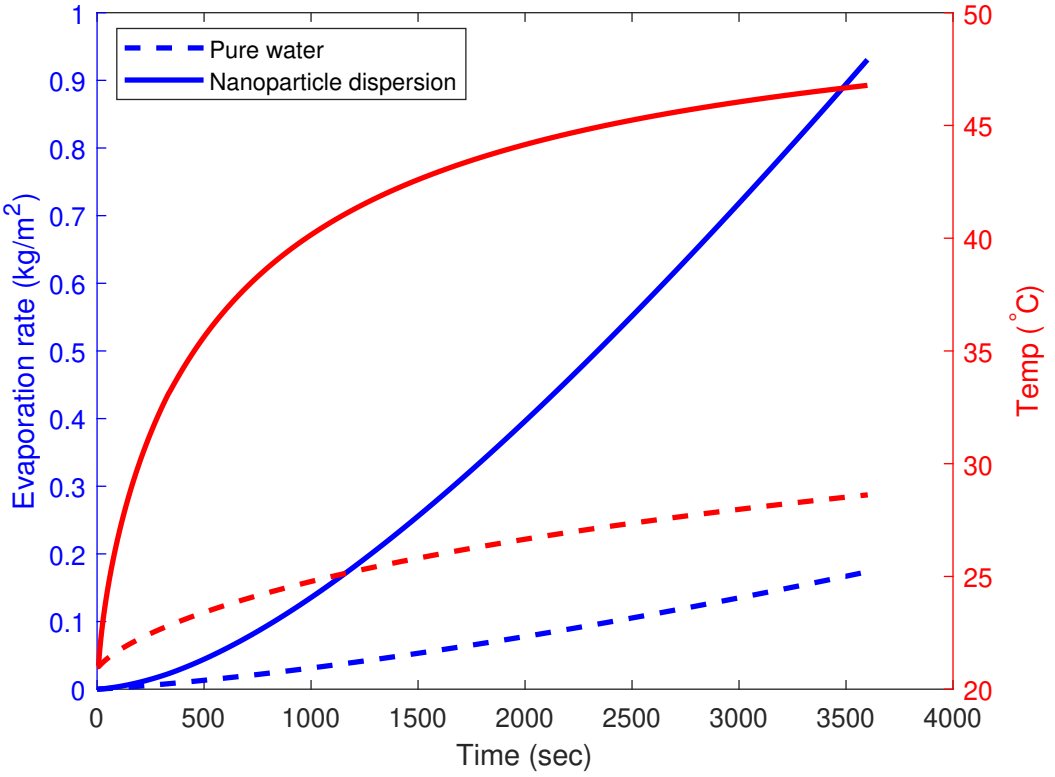

Figure 3.11: Hourly evaporation rate of water under 1 sun conditions for pure water and activated carbon nanoparticle dispersions

total hourly evaporation rate is 0.17 kg/m$^2-$h, while that for the nanoparticle dispersion is 0.93 kg/m$^2-$h. It is estimated that the system achieves steady state within 20 minutes. Steady state evaporation rate of pure water is found to be only 0.18 kg/m$^2-$h with a surface temperature gain of only 7.62 K. On the other hand, it is estimated that the steady state evaporation rate of water with activated carbon dispersions is 1.08 kg/m$^2-$h with a surface temperature gain of 25.7 K.

Experiments with carbon nanotubes (CNT) and reduced graphene oxide (rGO) and rGO with magnetic FO_3O_4 deduced that 1 sun evaporation rate observed was around 1 kg/m$^2-$h to 1.25 kg/m$^2-$h, respectively [51, 50, 53, 54].

3.7 Highlights

- The radiative volumetric heat generation as a result of photo-thermal conversion has a direct correlation to solar absorption fraction.
- Inspecting the relatively very low solar absorption for large particles from Chapter 2, large particles result in a comparatively low water evaporation enhancement rate compared to small particles.
- Ambient conditions of forced convection, relative humidity and system temperature influence the evaporation rate of water.
- Under 1 sun (1000 W/m^2) condition, evaporation efficiency of 43% can be obtained by these particle dispersions as opposed to <10% for pure water.
- Steady state evaporation rate of water with dispersions is expected to be around 1.08 kg/m$^2-$h which is similar to other published experimental studies involving carbon based nanofluids.

Chapter 4

Characterizing Biochar as stable carbon material for use as solar absorber in water

Biochar is a black char-type substance derived from pyrolyzing biomass which is being studied as a material to mitigate climate change in several applications [55]. Some of the widely adopted applications are in soil enrichment and enhanced crop productivity, energy production and management, super capacitors, metal sorption and industrial waste water treatment [56, 57, 58, 59, 60]. Biochar is inexpensive, and its optically black appearance can be used as a potential solar absorber for strong photo-thermal conversion in enhancing evaporation of water

when used in solar stills. Biochar is physico-chemically characterized as a stable carbon material, and the optical spectrum of biochar is measured. An open outdoor experiment is performed with biochar in granular form and as powder dispersions in water, to quantify enhancement in water evaporation rate.

Two biochars i.e., ponderosa pine (PP) and walnut shell (WS) from feedstocks pinus ponderosa and juglans, respectively are selected for this purpose. PP is commercially obtained from Biochar Now, where it is pyrolyzed at very high temperatures of around 750 to 800°C and then cooled by air. WS biochar was procured from a third party source, where it is pyrolyzed at 500°C at a heating rate of 30°C/min, and held at that temperature for 45 min. The samples obtained are then dried in a convection oven at 120°C to remove resident moisture and trapped gases, and characterized. For powdered sample characterization, the biochars are crushed using a mortar and pestle, and then passed through a #325 mesh sieve ($< 40\mu$m). For narrow particle distribution, and even finer sizes, these samples are further crushed in a planetary ball mill for more than 24 hours. Dynamic light scattering (DLS) analysis showed average particle size to be 854±85 nm for PP and 813±88 nm for WS crushed particles.

4.1 Physico-chemical characterization

Biochar is characterized physico-chemically to determine the carbon composition, its physical structure, and stability as a dispersion in water.

4.1.1 Chemical characterization

Ultimate analysis

Ultimate analysis is first performed to obtain the chemical C,H,N,S,O composition of the biochar samples, and the results are shown in Table 4.1. Both samples yielded more than 75% carbon composition while oxygen composition is found to be 9.5% for PP and 13.7% for WS. It is observed that several other inorganic elements are also present as impurities in the samples, as is also noted in [61].

Table 4.1: Ultimate Analysis of PP and WS biochars

Biochar	C (wt%)	H (wt%)	N (wt%)	S (wt%)	O (wt%)
PP	77.73	2.43	0.55	0.025	9.5
WS	75.86	3.48	0.64	0.04	13.7

^{13}C-NMR spectrum

^{13}C CPMAS NMR spectrum is obtained to understand the chemical structure of the biochar samples using an Agilent T3 probe with standard 3.2 mm zirconia

rotor and Agilent DD2 console. The chemical shifts were referenced to tetramethylsilane as 0 ppm using a solid adamantine sample at 38.5 ppm. Figure 4.1 shows the spectrum obtained for PP and WS biochar samples. The high temperature pyrolysis conditions resulted in biochars being predominantly aromatic [62], which is evident with the peaks at 127-128 ppm. Interestingly, some acidic carbonyl group (C$\equiv\!\!=$O) at $\approx$ 182 ppm, some aliphatic groups $<$ 90 ppm, and some carbons assigned to cellulose at 72 ppm were also observed [63, 64].

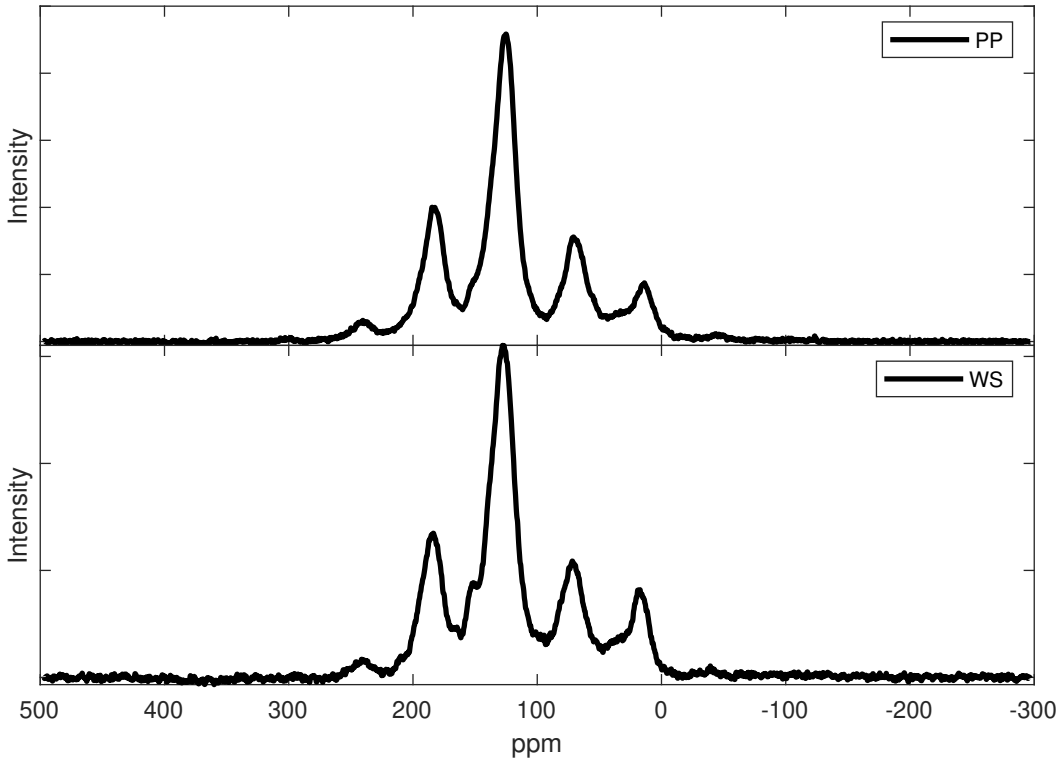

Figure 4.1: ^{13}C-NMR spectrum of (a) PP and (b) WS biochar

Chintala et. al noted that aromatic biochars are predominantly hydrophobic in nature [65]. The corresponding points of O/C and H/C, according to Table 4.1, when plot on a Van Krevelen plot, the points were closer to the origin, indicating a hydrophobic nature.

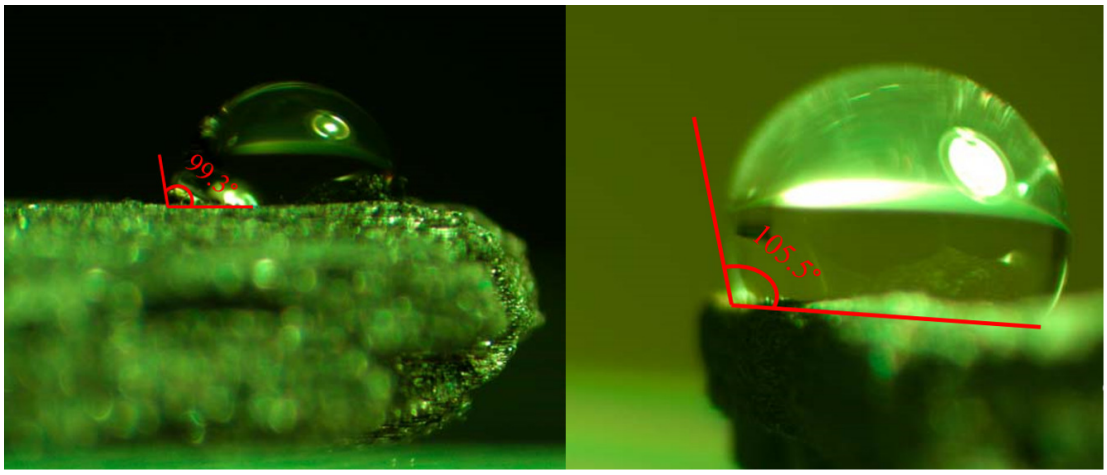

Figure 4.2: Contact angle measurement of of (a) PP and (b) WS biochar

The qualitative contact angle measurements obtained by an Amscope microscope and a high speed camera are shown in Fig. 4.2. The measured contact angles for PP and WS samples are 99.3° and 105.5°, respectively, verifying the hydrophobicity of the biochars. Weber and Quicker [66] noted that increasing pyrolysis temperature above 500°C might result in loss of hydrophobicity, most likely due to decrease in the strength of water repelling chemical bonds.

4.1.2 Physical characterization

Density

The density of the biochar samples is determined to check the possibility of using biochar as a floating as well as a dispersion material. True (skeleton) density is calculated using the helium pycnometry technique in a Ultrapyc 1200e instrument. The measurements recorded at less than 0.05% standard deviation showed that the skeleton density of PP and WS biochar samples are 1622.4 kg/m^3 and 1414.6 kg/m^3, respectively. Higher solid density in PP is partly due to higher pyrolysis conditions compared to WS. Further increase in pyrolysis temperature results in solid density close to that of graphite [36]. Geometric (envelope) density of the samples is measured using the mercury intrusion porosimtery (MIP) technique from ultra low pressures at 4.3 kPa to very high pressures at 412 kPa to ensure that almost all pores from the sizes 340 μm to 3.6 nm are intruded to compute the envelope fraction and the void sizes, i.e., pore content. The measured geometric density for PP and WS samples are 211.5 kg/m^3 and 631.4 kg/m^3, respectively.

The theoretical porosity of the biochar can be computed by using the formula $\phi = \left(1 - \frac{\rho_g}{\rho_t}\right) \times 100\%$, where, ϕ is the pore density, ρ_g is geometric density and ρ_t is the true density of the samples. The calculated porosity for PP and WS samples are 87% and 55.4%, respectively. The MIP calculated the porosity as

88% and 55.7%, respectively. The differential pore volume intruded by mercury with increasing pressure for smaller pores is shown in Fig. 4.3. PP biochar comparatively has more presence of large micron sized pores larger than 1 μm, while on the other hand, WS biochar had pores in the wide range of 10 μm to 100 nm with a significant presence of mesopores, and also some micropores. Water transport is aided by the presence of interconnected macro pores and meso pores [67] through capillary action.

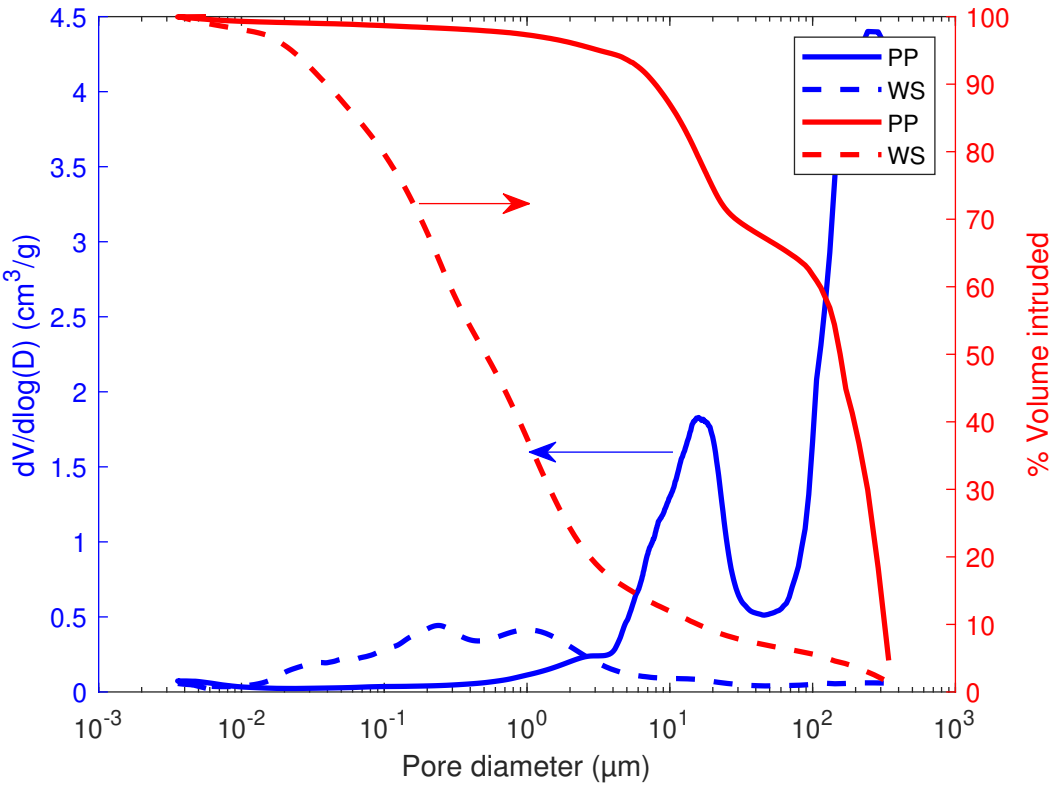

Figure 4.3: Pore size distribution of PP and WS biochars

Dispersion stability

The powdered biochar when suspended in water is required to be stable in dispersion form such that it does not sink to the bottom early in the test i.e., delay agglomeration. The dispersion stability is measured by using zeta potential [68]. The biochar samples are tested on an a Malvern ZetaSizer Nano ZS instrument equipped with a 4 mW HeNe laser operating at 632.8 nm and a scattering detector at 173 degrees.

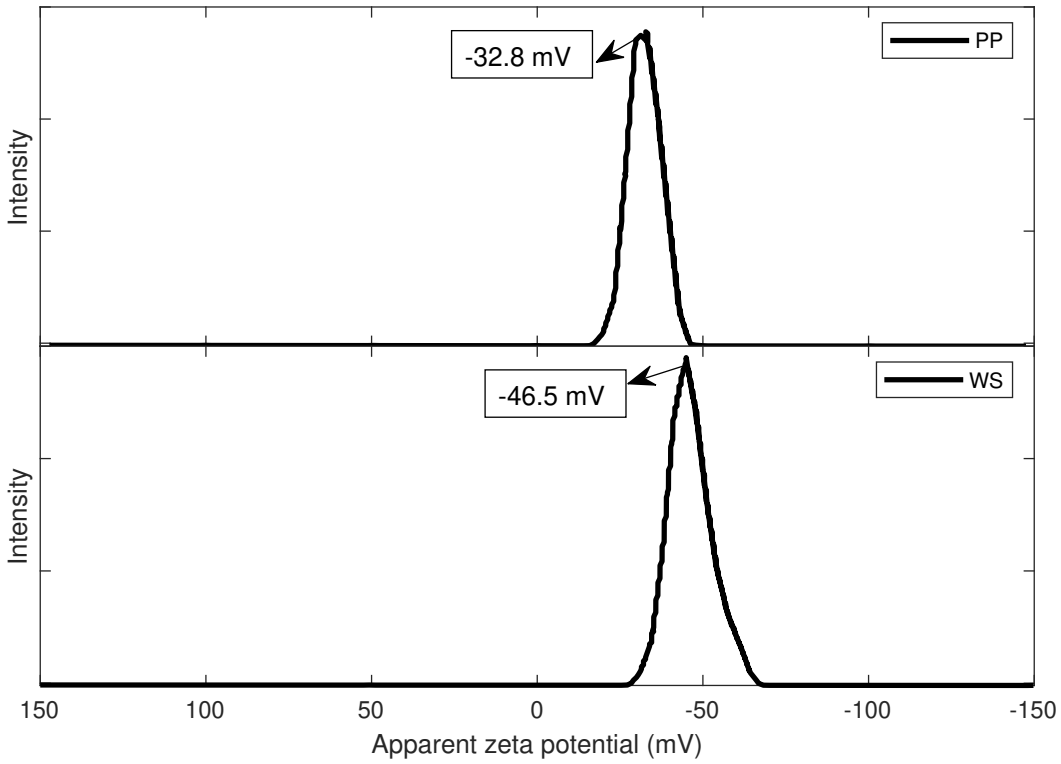

Figure 4.4: Zeta potential of (a) PP and (b) WS biochar dispersions in water

Figure 4.4 shows the dispersion stability of the PP and WS biochar dispersions with apparent zeta potentials. It is known that a zeta potential $> |\pm 30|$ mV has a good stability [69] while a minimum value of ± 20 mV is desirable [70]. The observed zeta potential for PP dispersion is -32.8 mV with a standard deviation of 4.76 mV, and that of WS dispersion is -46.5 mV with a standard deviation of 6.4 mV. Therefore, both samples show a good degree of stability in dispersion form. On a comparison basis, PP sample is slightly less stable, probably because the pyrolysis temperature is high.

4.2 Optical measurements

Biochar has been found to have excellent physical and chemical properties to be used as a floating solar absorber or as a dispersion. The optical measurements in the solar spectrum are measured using an integrated sphere in a Shimadzu 3600 UV-Vis-NIR spectrophotometer in the range between 200 and 2500 nm for floating type applications, and in the range between 200 to 1100 nm for dispersion liquid form.

Figure 4.5 shows the reflectance and transmittance spectrum of both PP and WS samples. In the solar spectrum range from 200 to 2500 nm, the combined reflectance and transmittance for both samples is less than 8% and 5% for PP

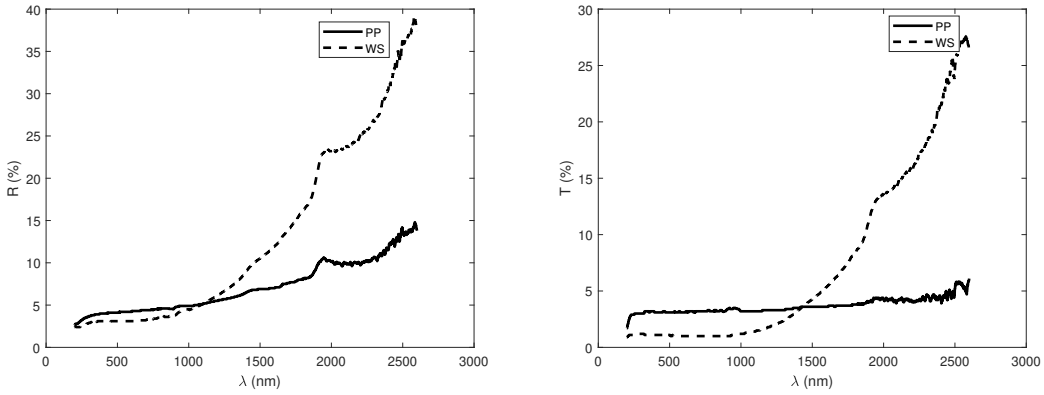

Figure 4.5: optical (a) reflectance and (b) transmittance spectrum of biochar samples

and WS, respectively. This means that the weighted solar absorptance in the solar spectrum for PP is 92% and that for the WS is 94%.

Liquid absorbance strength for both PP and WS dispersions is shown in Fig. 4.6 at a dispersion strength of 1 g/L for a 10 mm path length. The weighted absorbance (Abs) for PP and WS from 200 to 1100 nm solar spectrum is around 2.6 and 3.7, respectively, indicating a total transmittance (TT) of only 0.25% and 0.02%, respectively, for a 10 mm column. The liquid absorbance and the total light transmittance can be related by the equation $Abs = 2 - log_{10}TT\%$. It can likewise be estimated that, in the case of particle dispersions, light absorbance within the fluid might have also been enhanced due to the presence of micro-pores and mesopores [71, 72, 73]. It can be deduced that this concentration leads to a

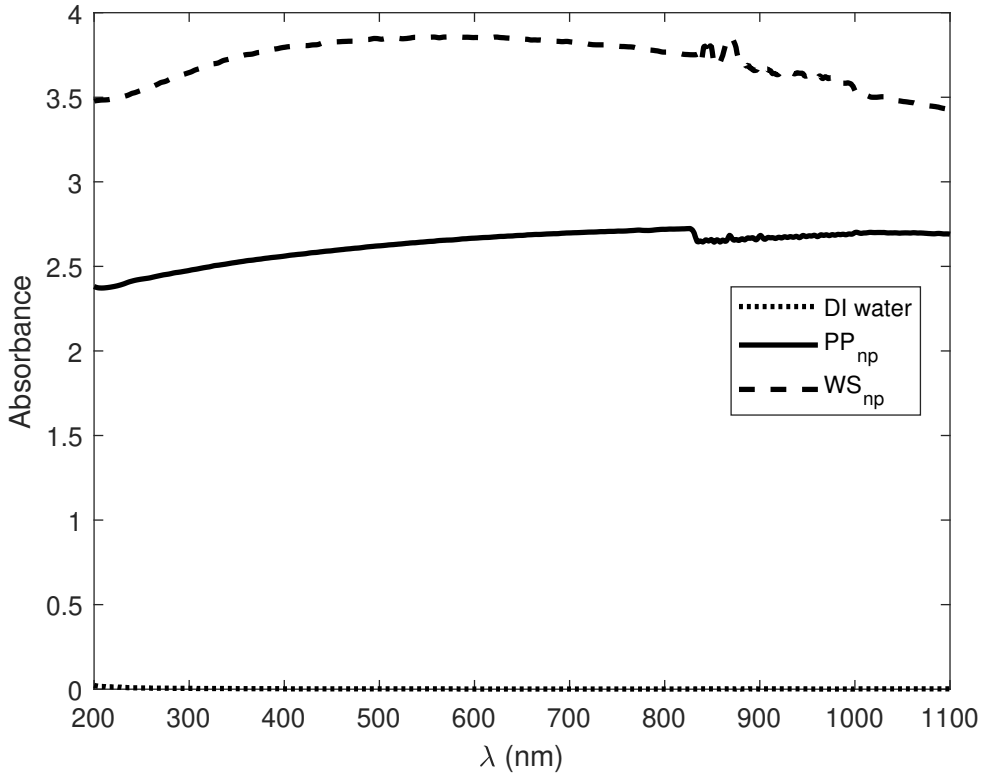

Figure 4.6: Liquid absorbance spectrum of PP and WS dispersion at 1 g/L concentration

very high heat localization near the surface, and concentrations lower than this can also result in strong photo-thermal conversion resulting in enhanced evaporation rates of water as explained previously in Chapter 3.

It is reported in the literature that increasing the pyrolysis temperature increases optical blackness i.e., absorption coefficient of the carbonaceous particle [36]. However, very high pyrolysis temperatures have been found to make the

dispersion unstable [74] along with increased dispersion concentration [75], as previously noted. It is thereby necessary to determine the appropriate pyrolysis condition for the given feed-stock for a strong carbon rich and stable biochar for use in the proposed application.

4.3 Controlled experiments with halogen lamp

A set of experiments were performed where the mass of water evaporated was recorded for an hour under 1 kW/m^2 condition with a halogen lamp used as a solar simulator at 21±1°C ambient temperature and 35% relative humidity, and the experimental setup is shown in Fig. 4.7 (a). Three samples: DI water, biochar (WS) dispersions, and biochar (WS) floating particles were used and the results compared. A 1.25 cm deep petri dish with a 60 ml working volume was used as the sample holder.

Figure 4.7 (b) shows the mass of water evaporated from the surface. In one hour, about 4.3 g of water evaporated from the DI water sample, with meager improvement observed with floating biochar particles. In the case of dispersions, total mass of water evaporated increased by 34% to about 5.85 g in one hour.

The evaporation rate of water with the above samples is shown in Fig. 4.8. With the petri dish basin of 1 cm depth, the mass evaporation rate of water is mea-

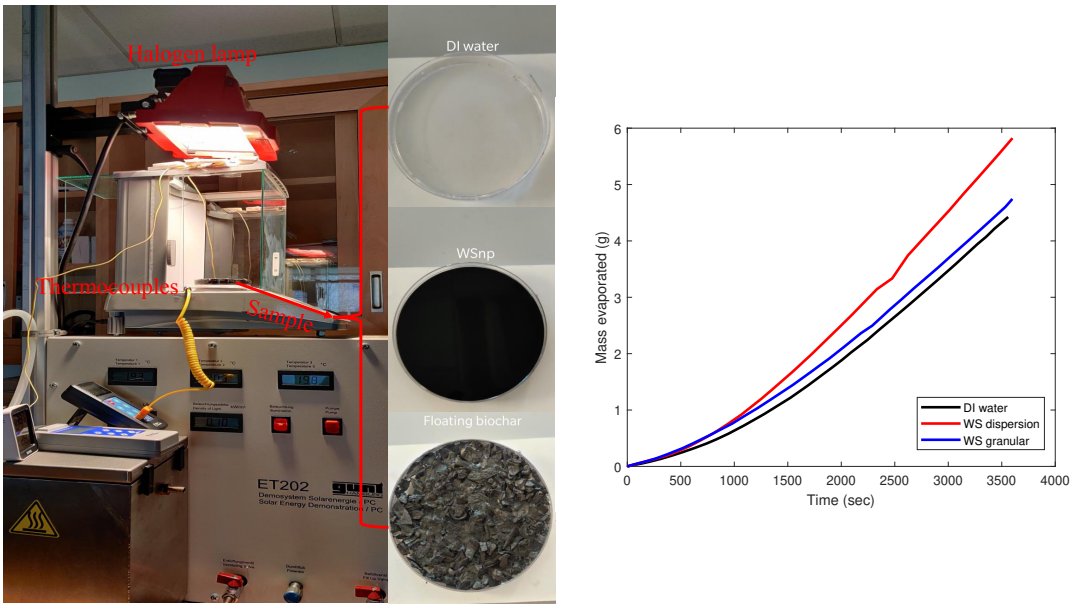

Figure 4.7: (a) Experimental setup for measurement of mass loss of water, (b) Mass of water evaporated from the surface

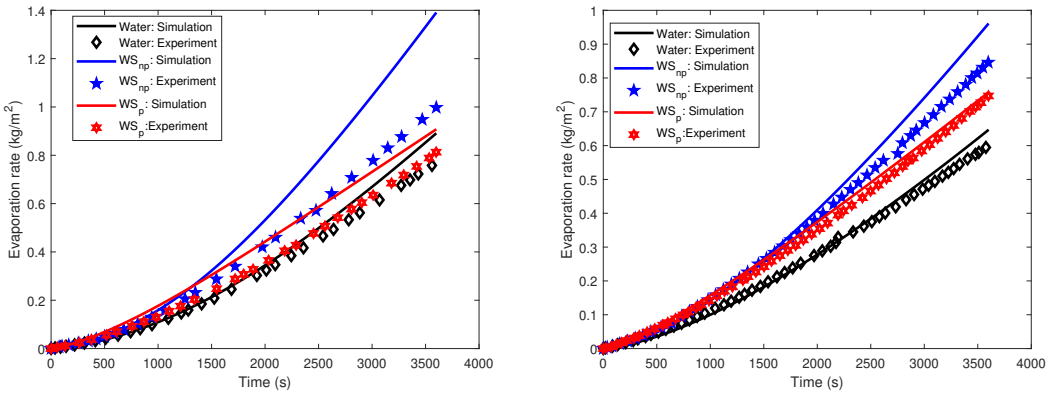

Figure 4.8: Mass evaporation rate of water with (a) 1 cm petri dish basin and (b) 5.5 cm glass flask basin

sured to be around 0.75 kg/m^2-h, while with the floating particles, it is measured to be 0.91 kg/m^2-h is observed. The evaporation rate with biochar dispersions is found to be 1.01 kg/m^2-h. A higher value in water evaporation rate is likely because the peak spectrum of the halogen lamp is much closer to the NIR region where water has good absorption properties. This reduces the actual enhancement in water evaporation rate as would be expected in the solar spectrum. To get an estimate of the performance under 1 sun conditions with solar spectrum, the hourly evaporation rate of water is simulated, first with a 3000 K spectrum of halogen lamp to validate the experiments which is shown with solid lines in Fig. 4.8, and then with airmass 1.5 solar spectrum. For the floating particle case, the simulation was performed with a simplified surface evaporation model assuming a weighted solar absorptivity of 0.92 for 3000 K spectrum intensity, and top surface thermal conductivity of 0.2 W/m-K [66]. With just 1 cm deep basin conditions, the simulations over predict the experimental observations. To confirm the validity of the code, another set of experiments and simulations were performed with a 5.5 cm deep water column in a glass flask, and simulations performed. The model for all the three cases trace the experimental observations with a good degree of accuracy. This was later used to predict the evaporation enhancement in water by using biochar dispersions. The simulation performed with solar spectrum showed a total evaporation rate of 0.21 kg/m^2-h for DI water, 0.85 kg/m^2-h

for floating dispersions and 1.01 kg/m^2-h for biochar dispersions. The predicted evaporation enhancement rate is 380% with biochar dispersions, and 304% with floating particles.

4.4 Solar absorber material cost comparison

The cost of biochar as solar absorbers is estimated and compared with other similar carbon materials published in literature. The cost of procured PP and WS biochar are \$ 15.5/ft^3 (\$ 3/kg) and \$ 9.26/ft^3 (\$ 1.3 /kg), respectively, and this is still expensive when compared to other estimates from commercial sources. The cost of ball milling biochar is estimated to be \$ 23510/ton (\$ 23.5/kg) for PP and \$ 5880/ton (\$ 5.88/kg) for WS, respectively, according to calculations presented by [76].

The cost of biochar particles, both in granular floating and in dispersion form for PP and WS samples is compared to other carbonaceous solar absorber materials published in literature: multi wall carbon nanotubes (MWCNT) [77], single wall carbon nanotube (SWCNT) [51], activated carbon fiber felt (AC felt) [78], carbon particle bulk wood (C-wood) [79], and are shown in Fig. 4.9. The unit cost of vapor produced by C-wood system is comparable to PP biochar while the WS floating biochar particles are cheaper than the other solar absorbers. Even

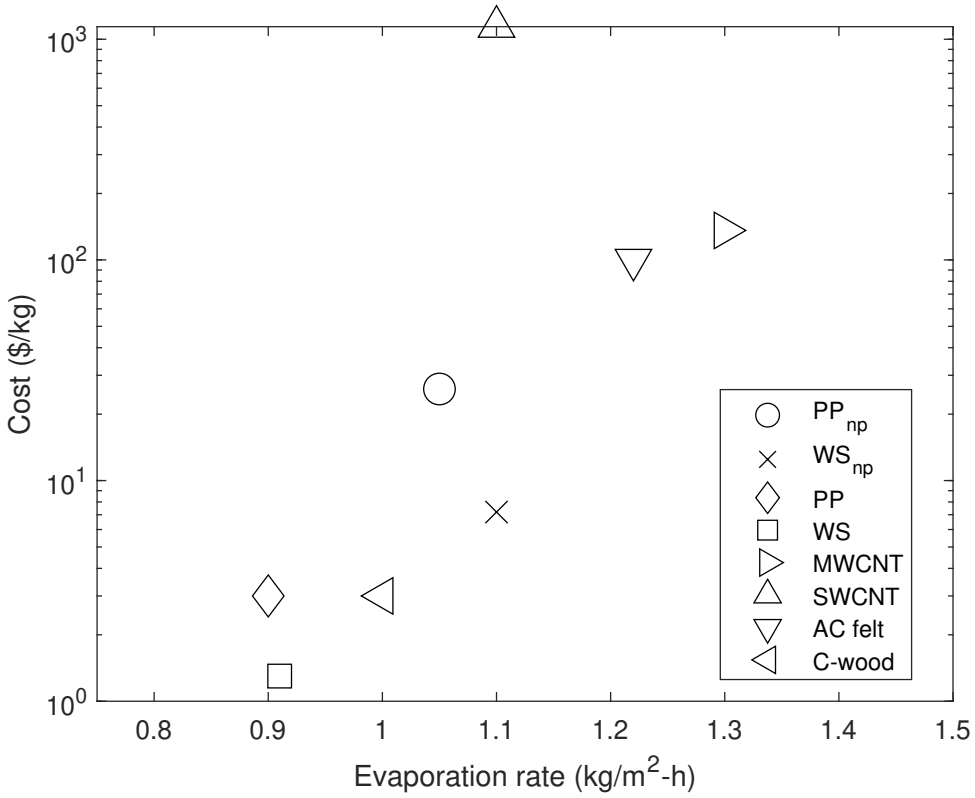

Figure 4.9: Cost per kg of solar absorber material against evaporation rate enhancement of water with biochar in comparison to other carbon materials

in dispersion form, the cost of PP and WS biochars are lower compared to the other systems with similar performance. Biochar dispersions were found to be at least 5-20 times cheaper than MWCNT's and 44-158 times less expensive than SWCNT's. It can thus be determined that biochar offers a highly economical solution for solar water evaporation with competitive evaporation performance in comparison to other proposed carbon based solar absorbers.

4.5 Highlights

- Biochar is characterized as a carbon rich source forming stable dispersions in water.
- Optical characterization showed more than 90% solar absorptivity as a floating solar absorber and less than 1% transmittance as dispersion at 1 g/L concentration for 10 mm path length.
- Outdoor experiments showed evaporation rate enhancement of up to 100% in dispersion form.
- In comparison to other similar solar absorber materials, biochar is an inexpensive material.

Chapter 5

Comparison of solar still for community scale freshwater production with other technologies

The analysis presented in previous chapters pertain to the application of photothermal energy conversion to utilize biochar and other similar black carbon materials in solar stills. The productivity of a single slope solar still depends on the incident solar irradiation with some influence of the ambient temperature and wind conditions. While a shallow still is commonly used, having deeper basins can

increase the nocturnal productivity of the solar still despite having lower daytime productivity. The freshwater productivity rate, depends on the temperature of the evaporating water. Higher temperatures are attained in the water by using strong photo-thermal conversion materials, as explained in Chapter 2. Solar stills are more suitable than other desalination technologies for freshwater requirements lower than 200 m^3/day [7]. The possibility of using solar stills with low-cost carbonaceous materials is investigated by comparing the aspects of daily freshwater productivity rate, total annual CO_{2-eq} emissions avoided and the life time cost of water produced in comparison to other feasible low-productivity technologies such as photovoltaic sea water reverse osmosis (PV-SWRO) and solar flat plate collector integrated humidification and dehumidification (FPC-HDH) system.

5.1 Methodology and modeling

With the aim of producing freshwater for a small community in the range of 1 to 10 m^3/d, a 1000 m^2 solar still basin area is considered assuming 1 kg/m^2-d of freshwater production during winter conditions. For comparison, solar PV and solar flat plate collector area are considered to be the same. The analysis is performed for two coastal regions with high solar irradiance at Big Sur in U.S.A and Chañaral in Chile.

5.1.1 System configuration and input information

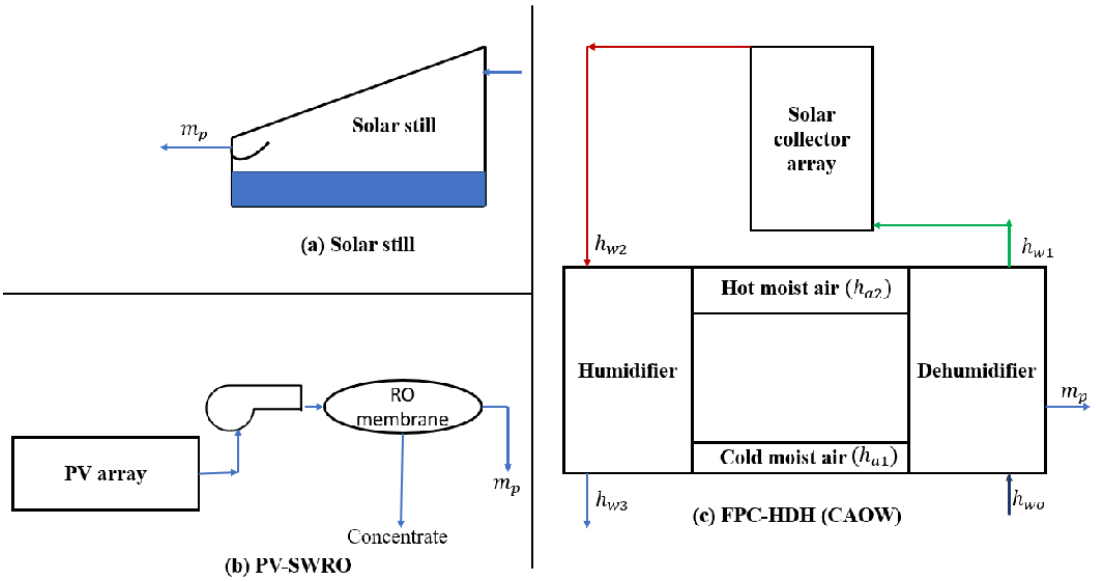

Figure 5.1: Selected configurations for (a) Solar still, (b) PV-SWRO and (c) FPC-HDH (CAOW) desalination systems

The system configurations for freshwater production using a solar still, FPC-HDH and PV-SWRO are shown in Fig. 5.1. A simple single-slope-single-basin solar still is considered for the analysis. For the HDH desalination system, a closed air open water (CAOW) configuration is selected with flat plate collectors as the water heating source. Similarly, the PV system is connected to a pump which increases the feed pressure of the saline water in the SWRO membrane.

The energy analysis is performed by solving a system of heat and mass transfer equations for the desalination systems. Hourly spaced solar irradiation data,

ambient temperature and wind speed information is extracted from the NREL System Advisor Model (SAM) database for the Big Sur location, and a typical meteorological year (TMY) file for Chañaral. The depth of water in the solar still is considered to be 10 cm, to account for nocturnal distillate production. To maintain the same feed conditions, assuming 8 hours of solar irradiation, the mass flow rate of inlet sea water is calculated to be 3.5 kg/s in the FPC-HDH and PV-SWRO systems. The sea water salt concentration is assumed to be 3.5%.

5.1.2 Governing equations for freshwater production

The thermodynamic governing heat and mass transfer equations for the analysis of freshwater production are shown in Table 5.1. The notation used for energy balance of FPC-HDH is consistent with [80], and those for PV-SWRO are consistent with [81, 82, 83]. The thermo-physical properties of water are obtained from [84].

The thermodynamic computations mentioned above are subject to the assumptions outlined below:

1. *Solar still* [85]:

    - Heat capacity of the glass, basin, and the insulation are neglected and the heat losses from the side walls are considered negligible.

Table 5.1: Energy and mass balancing of desalination systems for freshwater productivity

Technology	Governing Equations	Performance metrics
Solar Still [85, 86, 87]	*Glass cover:* $\alpha'_g I + h_{twg}(T_w - T_g) = h_{tga}(T_g - T_{amb})$ *Water mass:* $m_w C_{pw} \frac{dT_w}{dt} = \alpha'_w I + h_{twg}(T_g - T_w) + h_{cbw}(T_b - T_w)$ *Basin:* $\alpha'_b I = h_{cbw}(T_b - T_w) + h_{cba}(T_b - T_{amb})$ $h_{twg} = h_{ewg} + h_{cwg} + h_{rga}$ $h_{cwg} = 0.884\left[(T_w - T_g) + \frac{(P_w - P_g)(T_w(K))}{268900 - P_w}\right]^{1/3}$ $h_{rga} = \epsilon_{wg}\sigma(T_w^2 + T_g^2)(T_w + T_g)$ $h_{ewg} = 0.0163 h_{cwg} \frac{P_w - P_g}{T_w - T_g}$ $h_{cbw} = \frac{Nuk_w}{L_c}$	$Q_{ewg} = h_{ewg} A(T_w - T_g)$ $m_{hour} = \frac{Q_{ewg}}{I(t)A} 3600$ (kg/h) $\eta_{still} = F'_s\left[AT_s - U_{eff}\frac{T_w - T_{amb}}{I(t)}\right]$ $F'_s = \frac{1}{U_{total}} \frac{h_{ewg} h_{twg}}{h_{ewg} + h_{twg}}$ $AT_s = (\alpha\tau)_{eff}(1 - \exp(-at))$ $U_{eff} = U_{total} \exp(-at)$
HDH [80, 88, 89]	*Dehumidifier mass balance* $m_{da}(\omega_{a2} - \omega_{a1}) = m_p$ (kg/s) *Humidifier mass balance* $m_w = m_p + m_b$ *Dehumidifier energy balance* $m_{da}(h_{a2} - h_{a1}) = m_p h_p + m_w(h_{w1} - h_{w0})$ *Humidifier energy balance* $m_{da}(h_{a2} - h_{a1}) = m_w h_{w2} - m_b h_{w3}$ $h_a = h_{da} + \omega h_v$ $Q_{htf} = m_w(h_{w2} - h_{w1})$	$\varepsilon_{dh} = \max\left[\frac{H_{a2} - H_{a1}}{H_{a2} - H_{a,ideal}}, \frac{H_{w0} - H_{w1}}{H_{w0} - H_{w,ideal}}\right]$ $\varepsilon_h = \max\left[\frac{H_{a1} - H_{a2}}{H_{a1} - H_{a,ideal}}, \frac{H_{w2} - H_{w3}}{H_{w2} - H_{w,ideal}}\right]$ $GOR = \frac{m_p h_{fg}}{Q_{htf}}$ $m_{hour} = m_p * 3600$ (kg/h)
RO [81, 90]	*Permeate flow:* $m_p = (A_w\ TCF\ FF) S_e(\Delta\bar{P} - \Delta\bar{\Pi})$ (kg/s) *Salt flow:* $X_p = \frac{(B_s\ TCF) S_e\ CPF(\Delta X - X_p)}{m_p}$ *Water mass balance:* $m_w = m_p + m_b$ *Concentration balance:* $m_w X_w = m_p X_p + m_b X_b$	$m_{hour} = m_p * 3600$ (kg/h) $X_p < 0.5$ (g/kg)

- The solar still is vapor-air leakage proof.
- The temperature of the water mass is considered uniform with no stratification.

2. *HDH unit* [80]:

- The HDH unit operates at steady state and heat losses to the ambient are neglected.
- The fan/blower power is negligible in comparison to that of the solar collector.
- The thermal and hydraulic losses between collector and the HDH unit are ignored.

3. *RO unit* [91]:

- The liquid water is considered to be incompressible with known temperature and pressure conditions.
- The permeate flows at ambient pressure conditions ($P_{atm} = 1$ bar).
- The fouling factor varies with time as mentioned in [83].

The governing equations for the solar still listed in Table 5.1 results in a transient ordinary differential equation of the form:

$$T_w = \frac{\bar{f}(t)}{a}(1 - \exp(-at)) + T_{w0}\exp(-at) \tag{5.1}$$

where, T_w is the basin water temperature. To simplify the analysis, it is assumed that the water basin temperature is uniform, and this condition is justified considering nominal volume fraction of dispersions ($< 0.1\%$ as determined previously), and not very deep basins. f, a are functions of heat effective solar absorptivity and heat loss coefficient and are given as:

$$f(t) = \frac{\alpha_{eff} I(t) + U_{total} T_{amb}}{m_w C_{pw}} \tag{5.2a}$$

$$a = \frac{U_{total}}{m_w C_{pw}} \tag{5.2b}$$

where, the effective absorptivity (α_{eff}) is the aggregated contribution from effective glass absorptivity (α'_g), effective basin fluid absorptivity (α'_w) and effective basin absorptivity (α'_b), given as:

$$\alpha_{eff} = \alpha'_b \frac{h_{cbw}}{h_{cbw} + h_{cba}} + \alpha'_w + \alpha'_g \frac{h_{twg}}{h_{twg} + h_{tga}} \tag{5.3}$$

The corresponding effective glass absorptivity (α'_g), effective basin fluid absorptivity (α'_w) and effective basin absorptivity (α'_b) can be calculated from their absorptivity and reflectivity as:

$$\alpha'_g = \alpha_g (1 - \rho_g) \tag{5.4a}$$

$$\alpha'_w = \alpha_w (1 - \alpha_g)(1 - \rho_g)(1 - \rho_w) \tag{5.4b}$$

$$\alpha'_b = \alpha_b (1 - \alpha_w)(1 - \alpha_g)(1 - \rho_g)(1 - \rho_w) \tag{5.4c}$$

The overall heat transfer coefficient U_{total} is calculated as the sum of resistances from the basin water to the ambient through the cover as top heat transfer coefficient (U_{top}), and from basin water to the ambient through basin and insulation as bottom heat transfer coefficient (U_{bottom}), and are calculated as:

$$U_{top} = \frac{h_{twg} h_{tga}}{h_{twg} + h_{tga}} \tag{5.5a}$$

$$U_{bottom} = \frac{h_{cbw} h_{cba}}{h_{cbw} + h_{cba}} \tag{5.5b}$$

$$U_{total} = U_{top} + U_{bottom} \tag{5.5c}$$

Typically, the side insulation loss, with same insulation thickness as the bottom is much smaller than the bottom heat loss coefficient since the area of the side walls is smaller than the basin area, and thus, can be ignored.

5.1.3 Ambient heat losses and assumed parameters

The solar flat plate collectors are modelled according to traditional heat transfer equations mentioned in [92, 93, 94] and photovoltaic (PV) system modeled according to [95, 96, 97].

Losses from the glass cover occur due to both convection and radiation, and is given as:

$$h_{tga} = h_{cga} + h_{rga} \tag{5.6a}$$

$$h_{cga} = 2.8 + 3u \tag{5.6b}$$

$$h_{rga} = \epsilon_g \sigma (T_g^2 + T_{sky}^2)(T_g + T_{sky}) \tag{5.6c}$$

Where, T_{sky} is the sky temperature, which can be approximated as $T_{sky} = T_\infty - 6K$ [98].

Similarly, the bottom heat loss from the system can be given as linearized function of wind velocity [99]:

$$h_{cba} = 5.7 + 3u \tag{5.7}$$

Some thermo-physical and optical properties are considered as constants for the computations. Those properties are summarized in Table 5.2.

Table 5.2: Thermo-physical and optical constants

Solar Still	**FPC-HDH**	**PV-SWRO**
Glass properties	*Glass properties*	*Glass properties*
$\alpha_g = 0.05$	$\alpha_g = 0.05$	$\alpha_g = 0.05$
$\epsilon_g = 0.9$	$\epsilon_g = 0.9$	$\epsilon_g = 0.9$
Water properties	*Absorber properties*	*PV properties*
$R_w = 0.05$	$\alpha_{abs} = 0.95$	$\alpha_{pv} = 1$
$\epsilon_w = 0.96$	*HDH effectiveness*	$\beta_{pv} = 0.00468$ [100]
Basin properties: non selective	$\varepsilon_h = \varepsilon_{dh} = 0.92$ [80]	*Backsheet properties*
$\alpha_b = 0.6$	$T_p = f(T_{da1}, T_{da2})$ [101]	$\epsilon_b = 0.85$
$R_b = 0.3$	$T_{w0} = T_{amb}$	A_w and B_s for SW30HR-380 [102]

5.2 Solar system efficiency under standard conditions

A characteristic performance equation is often defined to quantify the performance of a solar thermal system as a function of reduced temperature ($T^* = \frac{T-T_{amb}}{I}$), which otherwise is called as instantaneous efficiency. The efficiency curves at standard conditions for solar still and FPC-HDH are traced at standard atmospheric conditions of 27°C ambient temperature, 1 m/s wind speed and 1 sun (1000 W/m^2) conditions, with saline feed flow rate of 1 kg/s, and with the objective of determining the operation characteristics.

5.2.1 Performance curves

Figure 5.2 shows the performance curves of a solar still, solar flat plate collector under typical standard conditions mentioned above. These similar curves can be obtained from the literature and thus are used to validate the heat transfer performance model for the solar flat plate collector and the solar still. The performance curves of the flat plate collector (FPC) deteriorate with T^* as expected. The solar still performance curve on the other hand increases with increasing T^*. The higher the basin water temperature of the basin, higher the vapor mass fraction, and thereby larger temperature difference between the basin water and

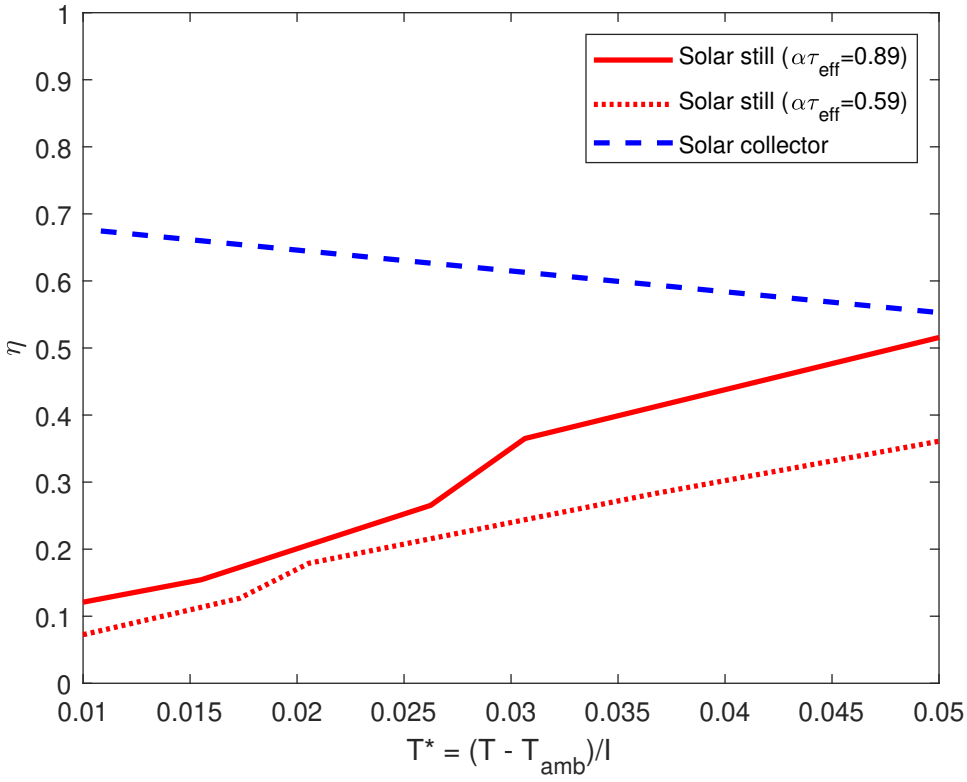

Figure 5.2: Performance curves of solar systems in consideration: solar still and solar flat plate collector

condensing cover, thereby increasing the evaporation efficiency of the solar still. The maximum evaporation efficiency of solar still, as remarked by Clark [103] is about 60 to 70%. Two solar still efficiency curves, at absorptivity-transmissivity product ($\alpha\tau_{eff}$) of 0.59 (basin absorber), and ($\alpha\tau_{eff}$) of 0.89 (black solar absorber) are shown, and clearly, it is evident that a black absorber is preferable to increase

solar absorptivity for higher distillate productivity, as previously explained in Chapter 2 and Chapter 3.

5.2.2 Influence of dispersion concentration on water absorptivity and distillate productivity

As shown in Fig. 5.2, for solar still curves, higher efficiency and thereby, higher distillate production occurs with higher absorptivity-transmissivity product. There will be a slight variation in the distillate productivity if the bottom basin is coated black, especially in deeper basins, where the bottom of the basin becomes hot first leading to unstratified buoyancy heat losses within the fluid while the hot water raises up, while at the same time experiencing bottom heat loss from the system. Low-cost carbon dispersion particles on the other hand, absorb the sun light near the evaporating surface.

It is observed from the Fig. 5.3 (a) that the solar still productivity and the solar still efficiency increase with increasing dispersion concentration, and the water solar absorptivity (attenuation fraction) and distillate productivity follow the same behavior. With no dispersion, the annual productivity is estimated to be of only 743 kg/m^2-yr, while that with dispersion concentration of 0.1%, it increases by 67% to 1241 kg/m^2-yr (irradiation and ambient data correspond to Big Sur). With 1.2-1.3 μm graphite nanoparticle dispersion, Sharshir et. al [19]

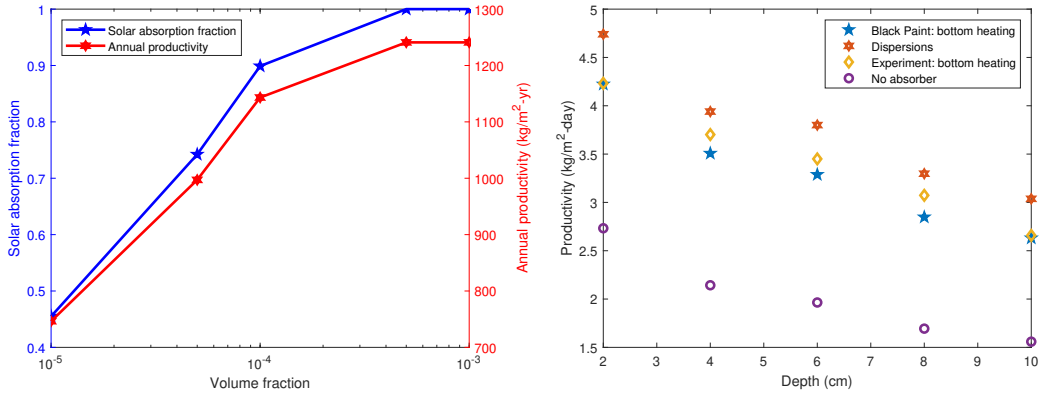

Figure 5.3: (a)Influence of dispersion concentration on solar still distillate productivity: computed annually; (b) Daily increase in freshwater productivity of a solar still with dispersions in comparison to a solar still with black basin and a solar still with no solar absorber

found an increase of distillate productivity of 45%. This concentration fraction is assumed for solar still productivity for the rest of the analysis for high solar absorptivity. Figure 5.3 (b) shows the relative gain in solar still productivity by having dispersions compared to a solar still with a black basin, and a solar still with no solar absorber. It is observed that nanoparticle dispersions have more pronounced effect on increasing the productivity of the solar still than a black basin in comparison to a solar still with just water in the basin. The experimental data pertains to observations recorded by Agarwal et. al [104] with a black basin in the solar still for varying water depths. On an average, the expected increase

in freshwater productivity with nanoparticle dispersions in comparison to black basin is around 0.5 kg/m^2−day.

5.2.3 Variation of hourly freshwater production with solar area

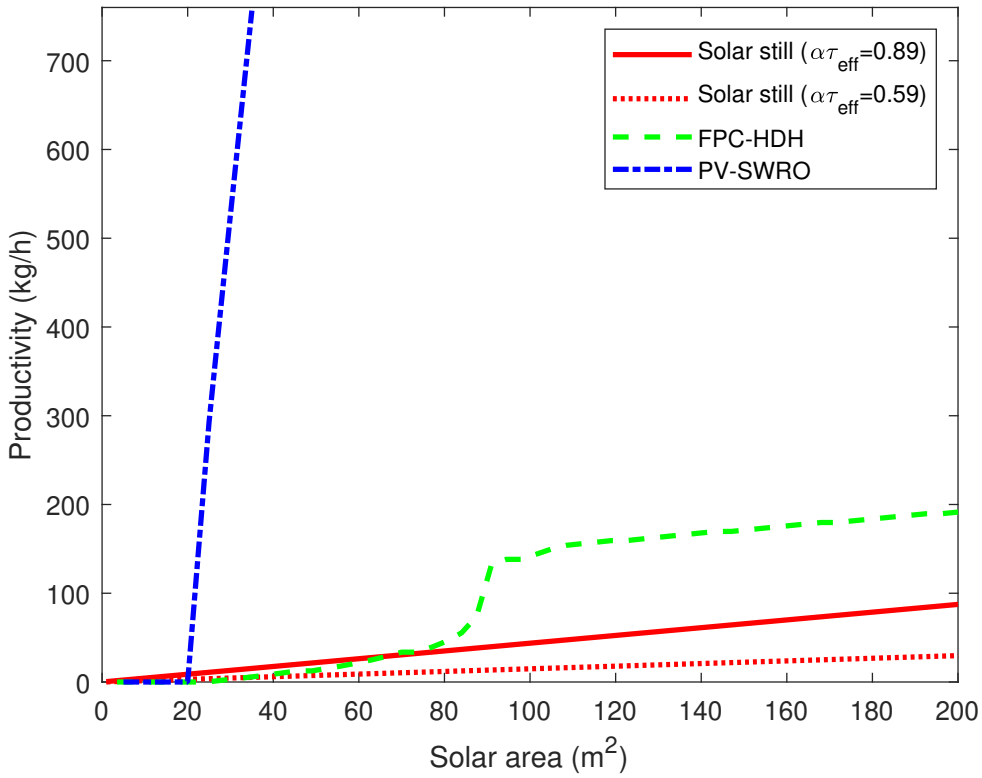

Figure 5.4: Hourly freshwater productivity from desalination systems at standard conditions at increasing area

Figure 5.4 shows the variation of hourly freshwater production of the solar still, FPC-HDH and PV-SWRO at standard conditions. The productivity of solar still increases linearly with area, and black solar absorber particles have higher distillate productivity rate. FPC-HDH have considerably higher distillate productivity rate with solar collection area greater than 80 m^2. The 1 sun condition occurs at mid-day, hence an average of 4 trials is performed with the solar still to obtain a reasonably acceptable initial fluid condition for solar still computation. This may over predict the solar still productivity by a small margin. An SWRO unit requires reaching a threshold feed pressure to separate freshwater from the sea water for acceptable freshwater quality of 0.05% TDS [105]. For the operating conditions, a minimum of 20 m^2 PV area is required to produce the energy needed to drive the PV-SWRO system to obtain the desired permeate quality [6]. The reason being, a minimum threshold pressure of 40 bars is needed to obtain fresh water with acceptable permeate quality. Further increasing the solar area increases the feed pressure thereby increasing the permeate production, until a maximum allowable feed pressure is achieved.

5.3 Freshwater productivity and excess energy from FPC and PV systems

Based on the incident irradiation and ambient conditions, year round freshwater productivity rates are calculated and compared for the three desalination technologies. For FPC-HDH, maximum temperature of feed water in the humidifier is restricted to 90°C in view of scaling due to prevalent boiling conditions. Similarly, maximum feed pressure in the SWRO elements is restricted to 55 bar for safe operation and durability of the membrane.

5.3.1 Year round freshwater productivity

The year round freshwater productivity for solar still, FPC-HDH and PV-SWRO for Big Sur and Chañaral with varying daily solar insolation are shown in Fig. 5.5.

It is observed from Fig. 5.5, that the freshwater productivity rates typically follow the daily solar insolation curves. The mean productivity of the solar still is lower than the other two technologies. HDH systems use the energy from the condensing freshwater to pre-heat saline feed, which is not the case in simple solar stills. Interestingly, it is observed that the seasonal RO productivity in certain seasons is lower than the HDH system, possibly due to the upper limit of 55 bar,

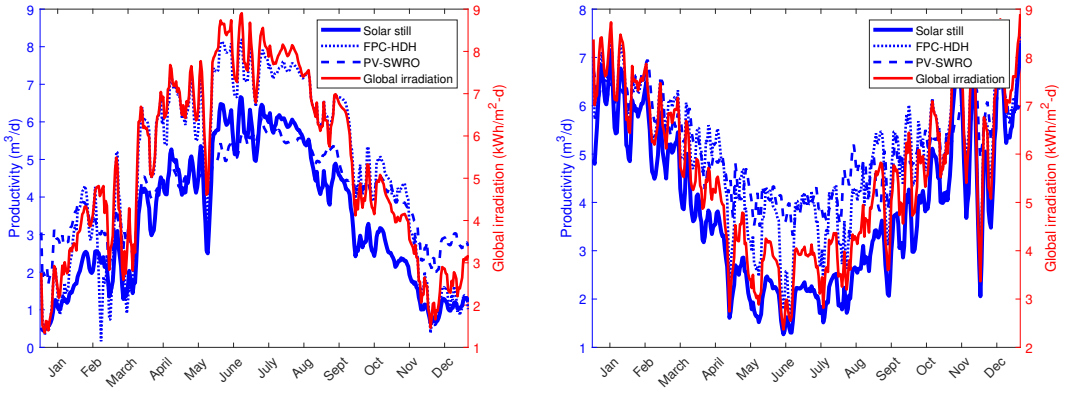

Figure 5.5: Seasonal year round productivity of solar still, FPC-HDH, PV-SWRO in (a) Big Sur (U.S.A) and Chañaral (Chile)

while, the maximum allowable pressure is 84 bar [90]. However, significant excess unused energy is generated, due to the imposed restrictions on the FPC and PV systems, and will be shown later. In Big Sur, the daily mean winter productivity and summer productivity for solar still is 2.25 m^3/d and 5.6 m^3/d, while that for FPC-HDH is 2.4 m^3/d and 6.15 m^3/d, and for PV-SWRO is 3.4 m^3/d and 5.42 m^3/d, respectively. Similarly, in Chañaral, the productivity for summer and winter are: 5.2 m^3/d and 2.3 m^3/d for solar still, 5.25 m^3/d, 2.98 m^3/d for FPC-HDH, and 5.8 m^3/d and 4.18 m^3/d for PV-SWRO, respectively. The annual average for 96% of plant operation i.e., 350 days, along with conventional solar still (CSS) is given in Table. 5.3.

Table 5.3: Average annual productivity

Location	**Solar still** (m^3/d)	**CSS** (m^3/d)	**FPC-HDH** (m^3/d)	**PV-SWRO** (m^3/d)
Big Sur (U.S.A)	3.42	2.13	4.79	4.12
Chañaral (Chile)	3.85	2.38	5.24	5.07

5.3.2 Excess energy

Due to the restrictions of maximum temperature and feed pressure for FPC-HDH and PV-SWRO mentioned above in the day time, excess usable thermal energy from flat plate collectors, and electrical energy from PV system is available. The monthly sum of the total thermal and electrical energy is shown in Fig. 5.6.

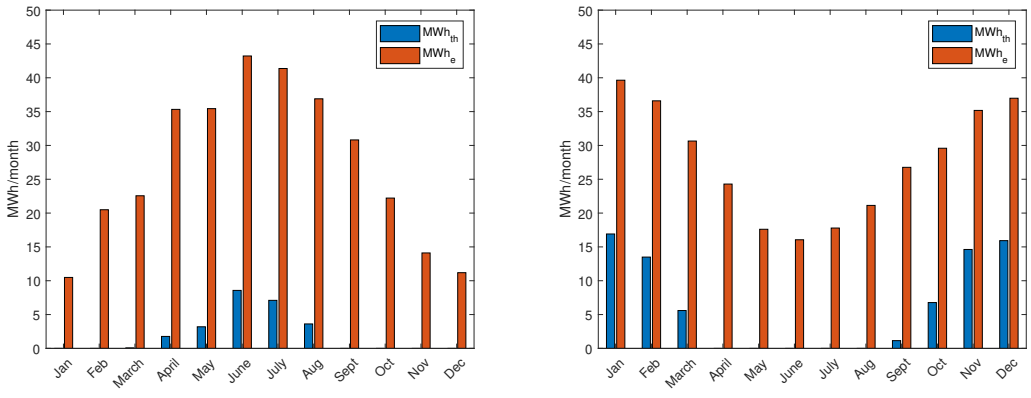

Figure 5.6: Seasonal year round additional thermal and electrical energy in (a) Big Sur (U.S.A) and Chañaral (Chile)

From Figure 5.6, it is observed that additional thermal energy from the flat plate collectors is only available during the summer, while the excess electrical

energy from the PV system is available through out the year. It is already shown that a PV-SWRO has a sharp productivity curve in Fig. 5.4. The electrical energy can be compensated by grid connection according to net surplus compensation (NSC) available locally. The annual average NSC value for California is taken as $ 0.04/kWh and that for Chile is considered to be $ 0.08/kWh [106, 107]. However, this option is not available with thermal energy, hence this excess thermal energy is expected to be stored by a thermal energy storage medium (TES) during the daytime and dispatched in the evening hours for additional desalination of water. Freshwater production by using this TES discharged thermal energy on an average is found to be 52 m^3/yr (3.2% of total distillate) in Big Sur, and 156 m^3/yr (8.5% of total distillate) in Chañaral. Annual net surplus of electrical energy sold to the grid for these two locations is calculated to be 311 MWh and 319 MWh, respectively.

5.4 Greenhouse gas emission mitigation

The energy consumed for desalinating 1 m^3 of water is called specific energy consumption (SEC). For a simple single evaporator system, the specific energy consumption for a thermal desalination process is between 500 and 800 kWh/m^3 [108], because the latent heat of evaporation of 1 kg of water is very high (around

2200 to 2500 kJ/kg). On the other hand, the SEC for the membrane (RO) desalination is lower than 10 kWh/m^3, while for non-optimal conditions, could be around 30-50 kWh/m^3 for sea water elements. If this energy is supplied by a conventional natural gas fired power plant, then the desalination process has associated greenhouse gas CO_{2-eq} emissions. Typically, the energy mix in California and Chile is dominated by the natural gas. The associated emissions and their corresponding characterization factor (GWP) for each emission type are shown in Table. 5.4. The cumulative natural gas emission factor in terms of CO_{2-eq} is 0.231 kg CO_{2-eq}/ kWh of energy produced.

Table 5.4: GHG emission potential of a natural gas fired plant

Emission	**(lb/billion BTU)** [109]	**(kg/kWh)**	**GWP** [110]	**kg $CO_{2\text{-}eq}$/kWh**
CO_2	117000	0.1811	1	0.1811
CO	40	0.619×10^{-4}	1.9	1.176×10^{-4}
NO_x	92	1.42×10^{-4}	298	0.0424
PM	7	10.8×10^{-4}	680	0.0074
Cumulative				0.231

The desalination thermal energy and electrical energy supplied at thermal efficiency of 80% and electrical efficiency of 45% [111] by natural gas power plant is substituted by renewable heat and electrical energy by solar systems which results in eliminating harmful greenhouse gas emissions. The total GHG mitigation for daily freshwater productivity, and the computed SEC is shown in Fig. 5.7.

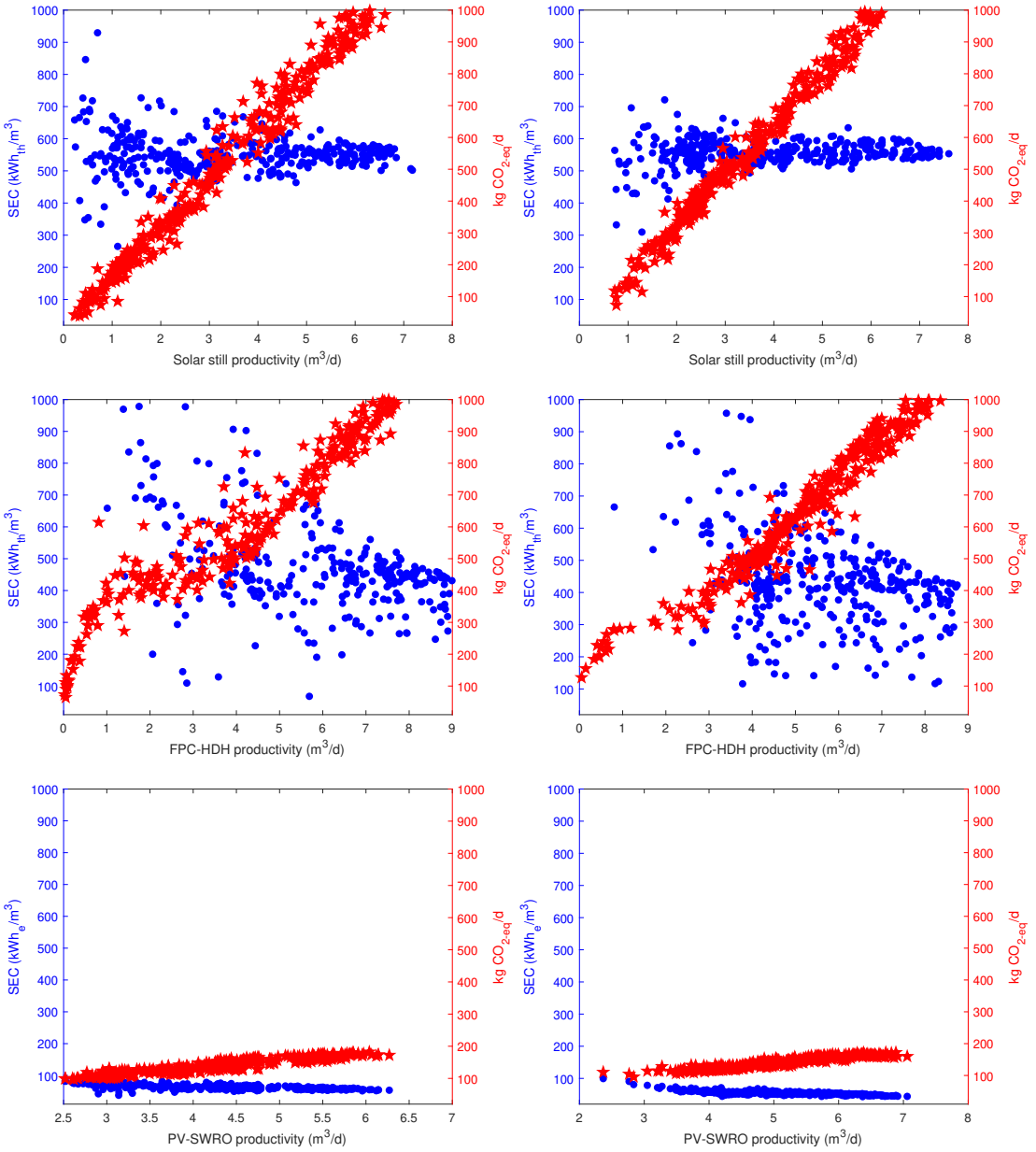

Figure 5.7: Specific energy consumption and daily CO_{2-eq} emissions avoided for freshwater productivity by solar still in (a) Big Sur and (b) Chañaral, FPC-HDH in (c) Big Sur and (d) Chañaral; and PV-SWRO in (e) Big Sur and (f) Chañaral

It is observed from Fig. 5.7 that the specific energy consumption for all the three desalination technologies decreases with increasing productivity until a certain value and then remains almost constant, while the net GHG emissions mitigated daily increases with increasing productivity. The SEC for a solar still is typically around 500 to 600 kWh/m^3 for a productivity greater than 3 m^3/day, which is approximately close to the calculated daily average. The daily CO_{2-eq} mitigation avoided follows a direct linear trend since the solar still directly absorbs and converts the solar energy into desalination energy. On the other hand, for FPC-HDH, lower productivity is not feasible due to very high conversion losses. It is observed that, despite the low solar irradiance, FPC's can reach a thermal efficiency of about 40% or more, but the productivity is low, due to low temperatures resulting in a high SEC. The GHG emissions avoided also follow the same trend as the increasing productivity. PV-SWRO on the other hand has a very low SEC, with most of the points in the range of 50 to 60 kWh/m^3. The daily emissions mitigation also increases with the productivity, similar to other desalination systems. In the location of Big Sur, it is expected that total annual CO_{2-eq} mitigation for solar still, FPC-HDH and PV-SWRO are 197.3 tons CO_{2-eq}, 244.1 tons CO_{2-eq} and 48.8 tons CO_{2-eq}, respectively, while the same at Chañaral are expected to be 227.3 tons CO_{2-eq}, 241.5 tons CO_{2-eq}, and 50.7 tons CO_{2-eq}, re-

spectively. This emissions mitigation results in annual carbon credits, which are assumed to be \$ 65/ ton CO_{2-eq} mitigated [112].

5.5 Cost of freshwater produced

The competitiveness of using a desalination technology is assessed by the cost of the freshwater produced by it. A levelized cost approach that considers life time operation and freshwater production is adopted to calculate the unit cost of freshwater. The levelized cost of water (LCOW) calculation is analogous to that of levelized cost of electricity/ heat, and is given as [113]:

$$LCOW = \frac{CAPEX + (OPEX + annual adjustments) * PVF(d,n)}{Annual\ productivity * PVF(d,n)} \tag{5.8}$$

$CAPEX$ is the overall capital investment in \$ and $OPEX$ is the annual operational cost in \$/yr. Annual adjustments refer to carbon credits, and salvage value is not considered. The present value function (PVF) is the parameter that gives the present worth of the unit, and is calculated as:

$$PVF(i,n) = \frac{(1+d)^n - 1}{d(1+d)^n} \tag{5.9}$$

Typically, solar stills are not widely commercialized due to poor productivity and poor choice of materials. While efficient means of increasing the productivity have been identified, appropriate materials choice determines the cost of the still,

and thereby the cost of the freshwater produced. One of the inherent assumptions is that, the land area is considered to be available at free of cost by BOOT option (BOOT: build, own, operate, transfer), or from local civic body [108]. A wide range of materials are usable, and a solar still made of concrete and stainless steel basin, window glass and silicone sealant showed the cost of the solar still can be only \$ 46/m^2. A similar solar still made of concrete by Madani and Zaki [114] was only \$ 19/m^2. In this analysis, a typical solar still cost of \$ 80 /m^2 is assumed, which is the cost of some of the tested solar stills in U.S.A [114]. For FPC-HDH, the cost of the solar FPC's are dominant, and can be divided into area dependant costs and area independent cost. Area independent cost is the cost of piping, pump, electrical and other ancillary instruments, and in this case is assumed to be \$ 50000 [115]. Solar FPC cost is considered to be \$ 350/m^2 based on the applicable correlations [116, 117]. Similarly, for PV-SWRO, recent estimate of PV system cost of \$ 2.25/W is considered [118]. In the decade of 2010-2020, PV system cost of \$ 1.25/W to \$ 9/W has been utilized in the literature [81, 119, 120, 121].

The total direct capital cost associated with the solar still, FPC-HDH and PV-SWRO is determined to be \$ 72,796, \$ 444,300, and \$ 556,470, respectively. The corresponding share of different direct capital costs associated with the desalination units is shown in Fig. 5.8. Solar components, i.e., solar still, flat

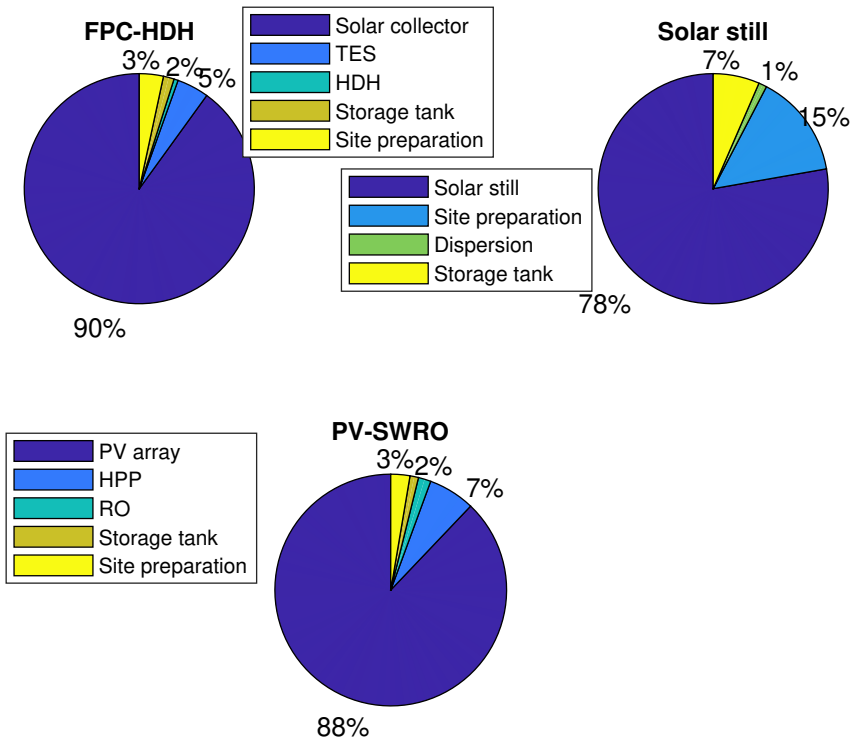

Figure 5.8: Capital cost share of different solar desalination components

plate collectors and the PV arrays, take up the biggest share of direct capital costs. The cost of thermal energy storage is considered to be \$20/kWh. The cost of high pressure pump (HPP) can be approximated by the correlation [122] $HPP = 52(Q_{f,h}P_f)$, where $Q_{f,h}$ is the hourly feed flow rate in m^3/h and P_f is the feed pressure in bar.

The indirect costs associated are assumed to be 10% of direct capital for contingency and 5% of direct capital cost for freight and insurance [108]. Annual

operation and maintenance cost is assumed to be 1.5% of total capital cost excluding annualized replacement of the parts, which are estimated to be 10% for the thermal energy storage (TES), 10% for the high pressure pump and 20% for RO membranes. Labor costs differed between the regions due to differences in standards of payments at contractual basis. The annual labor for Big Sur is considered as $25,000, while that for Chañaral is $ 15,000. The inexpensive dispersions are assumed to be replaced every 4 months as a conservative approach, while it is expected that they can be washed and reused. The discount rate is assumed to be 5%, with the desalination plant life of 25 years.

5.5.1 LCOW in Big Sur and Chañaral

The unit cost of water, levelized for the plant life time and discount rate for the three desalination systems is shown in Table. 5.5. The unit LCOW of conventional solar still with no nano/micro-particle dispersion is shown for comparison purpose. For the chosen conditions, which is commonly expected during cost estimations, the solar still system is found to be more economical than the other two technologies. The cost of water produced in Big Sur is more in comparison to Chañaral, because of lower annual productivity, and higher labor costs with regards to all the three systems. In addition, for the PV-SWRO case, the NSC grid compensation rate in Big Sur is lower than Chañaral. The lowest

estimates correspond to discount rate of 3% and attractive $CAPEX$ and $OPEX$ costs, corresponding to the left hand side data lables in Fig. 5.9. Similarly, the highest estimate correspond to a pessimistic discount rate of 8%, with $CAPEX$ and $OPEX$ costs corresponding to the right most data labels in Fig. 5.9.

Table 5.5: LCOW estimates for desalination of water

	Big Sur				Chañaral			
LCOW	**PV-SWRO**	**Solar still**	**CSS**	**FPC-HDH**	**PV-SWRO**	**Solar still**	**CSS**	**FPC-HDH**
Typical ($/m^3)	33.25	18.99	25.68	41.58	25.57	10.33	12.11	34.6
High ($/m^3)	48.67	48.41	77.74	63.03	37.59	49.4	78.33	52.01
Low ($/m^3)	23.98	12.92	20.71	31.17	18.3	3.74	5.85	22.87

5.5.2 Sensitivity analysis

The cost of water is expected to be sensitive to the $CAPEX$, $OPEX$ and discount rate. In this analysis, one parameter is varied at a time while others are kept constant. While it is not necessary that the extreme points are the most optimistic or pessimistic values, but they show a trend that can be extrapolated for other expected values. Figure 5.9 shows the sensitivity analysis of the three desalination technologies at both selected locations. In the case of solar stills, if poor choice of materials leads to a high solar still cost of \$ 500/m^2, the $LCOW$ increases significantly to more than \$ 40/m^3. Likewise, $OPEX$ also influences the $LCOW$, but in the actual application, it is anticipated that the operations and maintenance of the solar stills will be smaller than the other two complex

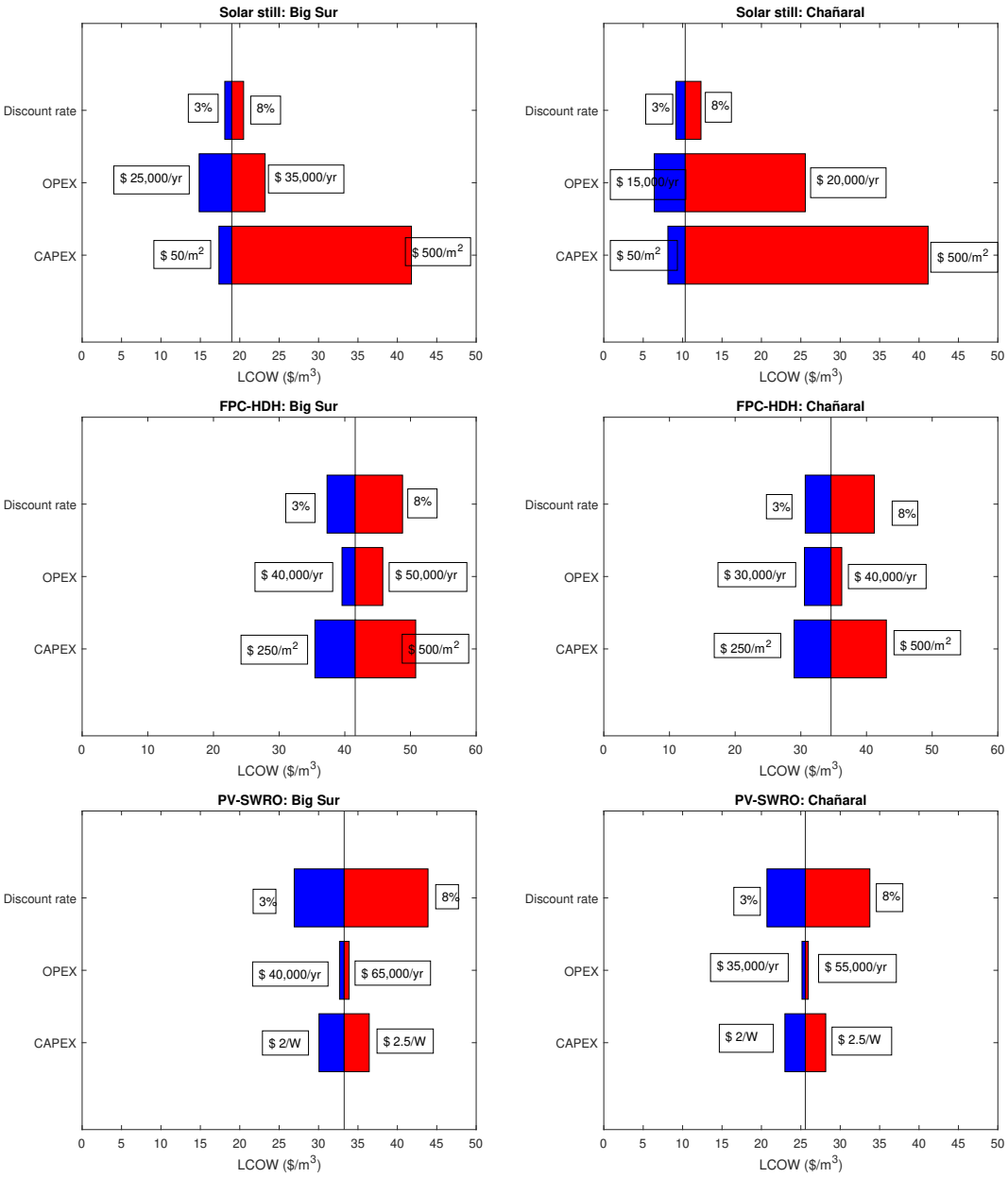

Figure 5.9: LCOW sensitivity analysis of solar still system in (a) Big Sur, (b) Chañaral; FPC-HDH in (c) Big Sur, (d) Chañaral; PV-SWRO in (e) Big Sur, (f) Chañaral

technologies. In the case of FPC-HDH system, $CAPEX$ and discount rate have shown to affect the $LCOW$ of the system, while, around 10-20% change in the $OPEX$ costs have some small influence in the $LCOW$. In the case of PV-SWRO system, interestingly, highest influence is asserted by the discount rate, with a high discount rate of 8% increasing the $LCOW$ to \$ 43.89/m^3 in Big Sur and to \$ 33.76/m^3 in Chañaral. System $CAPEX$ is found to have some influence in the $LCOW$, while, around 20% change in $OPEX$ shows negligible affect.

5.5.3 Parametric influence of solar system area

It can be envisaged that a smaller PV system area might be sufficient to produce almost the same amount of desalinated water from the SWRO elements as a lot of excess electricity is being sold at the grid. A brief look at the grid compensation rates and the PV system prices show that the system capital cost can be brought down significantly for little to no compromise in freshwater production capacity. On the other hand, in summer, solar flat plate collectors also produce a small of amount of excess thermal energy, as demonstrated earlier, and possibly, a smaller solar flat plate collector area might produce freshwater at a cost lower than that of a 1000 m^2 FPC area. A parametric influence of solar collection area on the freshwater cost (LCOW) for FPC-HDH and PV-SWRO is performed in this analysis to observe if lower costs are attainable for these systems.

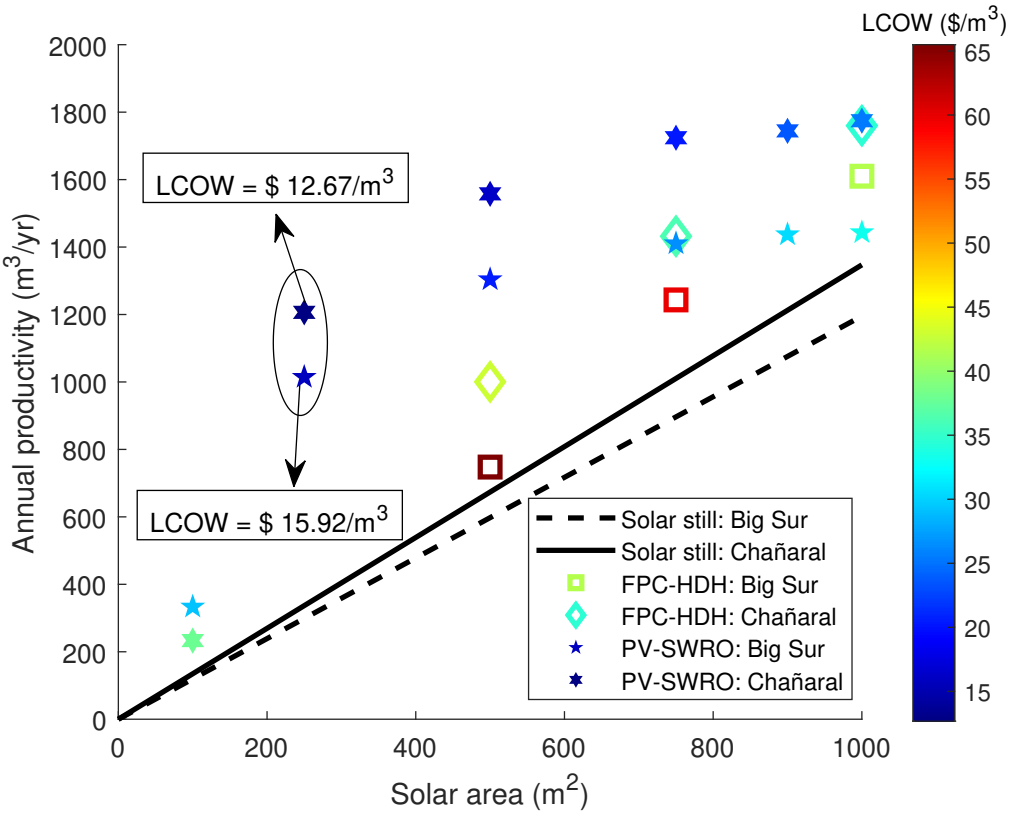

Figure 5.10: Parametric influence of solar collection area on freshwater LCOW for FPC-HDH and PV-SWRO

Figure 5.10 shows the influence of solar collection area for FPC-HDH and PV-SWRO on freshwater LCOW. It is observed that there is some influence on freshwater productivity at lower solar areas with PV-SWRO, while the influence is significant with FPC-HDH. It is observed that a minimum 250 m^2 area is needed for producing community scale water greater than 1000 m^3/yr. An LCOW estimation performed on the PV-SWRO system showed that the cost of permeate

decreased with decreasing the area from 1000 m^2 to 250 m^2, At which point, the lowest value of \$ 15.92/m^3 in Big sur and \$ 12.67/m^3 in Chañaral are obtained. Further reducing the area resulted in a much lower distillate production, which increased the LCOW of freshwater produced.

5.6 Highlights

- For the chosen locations of Big Sur (USA) and Chañaral (Chile), under real time conditions with 1000 m^2 solar collection area, solar stills can produce freshwater at a rate of 3.42m^3/d to 3.85 m^3/d.
- Under similar conditions, FPC-HDH system can produce freshwater at a rate of 4.79 m^3/d to 5.24 m^3/d and PV-SWRO can production rate of freshwater is 4.12 m^3/d to 5.07 m^3/d with over 310 MWH annual excess electricity.
- For a 25 year plant life, the estimated levelized cost of freshwater ($LCOW$) produced from the solar still, FPC-HDH and PV-SWRO are \$ 18.99/m^3, \$ 41.58/m^3, \$ 33.25/m^3 in Big Sur, \$ 10.33/m^3, \$ 34.6/m^3, \$ 25.57/m^3 in Chañaral for the given range of 1 to 10 m^3/d.
- In lieu of excess energy produced by the PV-SWRO system, for an optimal PV area of 250 m^2, the $LCOW$ reduces to \$ 15.92/m^3 in Big Sur and \$ 12.67/m^3 in Chañaral.

Chapter 6

Environmental impacts and economic feasibility of solar stills

One of the major barriers for commercialization of solar stills is its low productivity rate per unit area in comparison to newer thermal desalination technologies such as MSF or MED. While these are not feasible for smaller community scale desalination requirements lower than 100 m^3/d, solar stills can be independently installed in suitable locations as stand alone units, especially in poor remote rural communities. For these small scale freshwater requirements, solar stills are already found to be competitive compared the other solar powered desalination systems. Solar still performance is mainly dependent only on solar irradiation, and almost independent of the solar still materials, as long as the solar still com-

ponent requirements are satisfied. In this chapter, with the aim of determining the feasibility of low-cost solar stills as freshwater production systems, solar still materials combination for lower environmental impact and costs are identified, and the levelized cost of freshwater (LCOW) produced is calculated for feasibility analysis. The state of California is chosen as a reference geographical location for the analysis.

6.1 Solar still components

A solar still consists of a condensing cover, typically made of a high transmitting glass, a basin to hold water, thermal insulation, and an outer still body, which is usually made of the same material as the basin. Sealants are used to seal the air gaps. The idea behind solar stills is to construct them from locally available, durable and inexpensive materials [123]. Each component has a particular set of requirements to be satisfied for use as solar still materials. The common requirements are:

1. Withstand high temperatures, at least 80°C.

2. Resistance to water corrosion, and UV degradation, possibly at least 25 years.

3. Outside materials should be strong enough to sustain extreme weather conditions such as strong winds.

6.1.1 Condensing cover

The condensing section in a simple solar still involves the condensation of evaporating water on the transmitting cover, and for that purpose, this component should have high high transmissivity to the incoming solar irradiation, high thermal capacity, and low reflectivity (ρ) and absorptivity (α). These properties depend on the optical constants i.e., refractive index (n) and absorption coefficient (k) of the glass (cover) material. The surface reflectivity (ρ) can be estimated as a function of n as $\rho = (\frac{n-1}{n+1})^2$. To limit this to below 5%, the value of n should be less than 1.6, which is typically satisfied by glass materials. The absorptivity depends on the absorption coefficient (k) and the depth of light travel, i.e., the thickness of the cover material. Usually, this value is kept around 3 mm to 4 mm to lower the size of the glass cover. k is usually spectrally dependant on the incident sun light, and absorptivity is calculated as

$$\alpha = \frac{4\pi k}{\lambda} y \tag{6.1}$$

Where, the term $\frac{4\pi k}{\lambda}$ is the extinction coefficient of the glass (β_{ext}). The spectral absorption coefficient of glass cover materials is shown in Fig. 6.1.

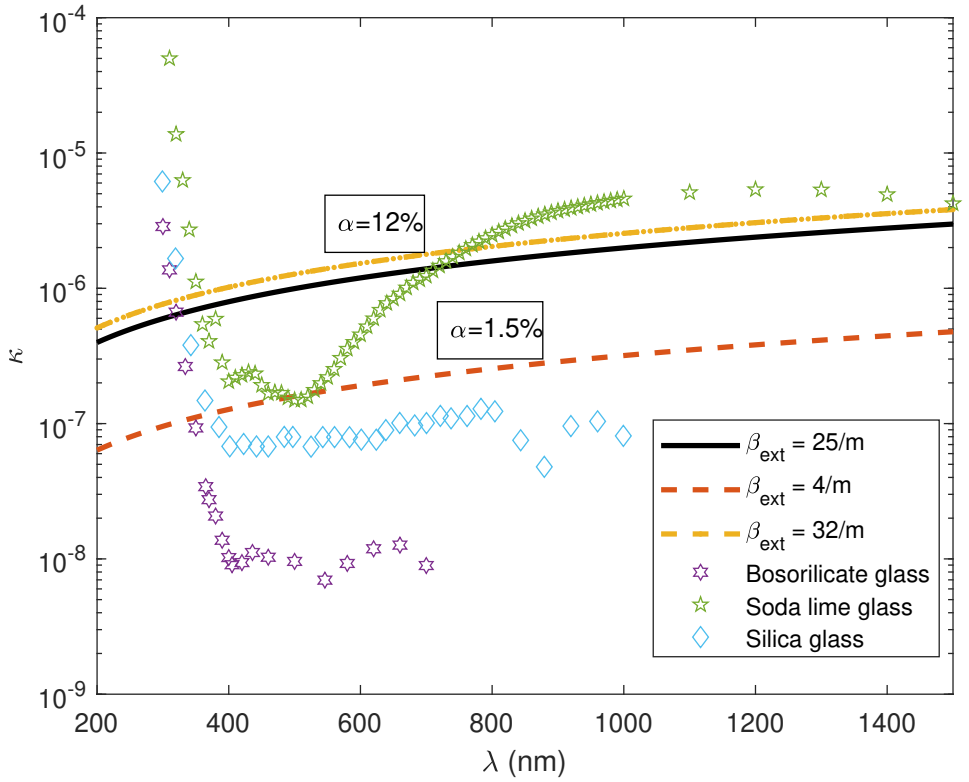

Figure 6.1: Absorption coefficient of glass cover materials

The extinction coefficient for a transmitting glass usually falls between 4/m to 32/m [124], shown as dotted lines in Fig. 6.1, and the calculated corresponding absorptivity is 1.5% and 12%, respectively. The spectral optical constants are extracted from the web source [1], which contains a collection of optical constants for many different materials. From the Fig. 6.1, it is observed that these glass materials have a very low absorption coefficient, mostly below the higher bound

[1] https://refractiveindex.info/

of 12% solar absorptivity spectral curve. The solid line represents the spectral absorption coefficient for extinction coefficient of 25/m, which corresponds to the average value for most of the commercial transmitting glass materials.

6.1.2 Basin and thermal insulation

The solar still basin holds the saline feed water, and in traditional practice, is usually painted black or contains low-cost black materials for strong solar absorption. A thermal insulation is added to restrict heat loss from the bottom, since the basin is usually around the same temperature as the salt water inside. The distillate production can be improved by about 30%, by having a good thermal insulation [125]. The solar still basin and the thermal insulation form a series thermal resistance network, as mathematically represented in the governing equations Table 5.1 in Chapter 5. The thickness determines the heat transfer loss coefficient from the bottom of the basin to the ambient through the bottom insulation.

Figure 6.2 shows the influence of bottom heat transfer resistance (inverse of bottom heat transfer coefficient), and the thickness dependency of the solar still basin and the thermal insulation. Figure 6.2(a) shows the variation of solar still performance with the bottom heat transfer resistance, which is calculated as $R = \frac{1}{\frac{\delta_b}{k_b}+\frac{\delta_{ins}}{k_{ins}}}$, for 3 cm, 6 cm and 9 cm depth of water in the basin. The daily solar still efficiency is calculated as $\eta_{day} = \frac{Q_{evap}}{I}$, where Q_{evap} is the evaporation

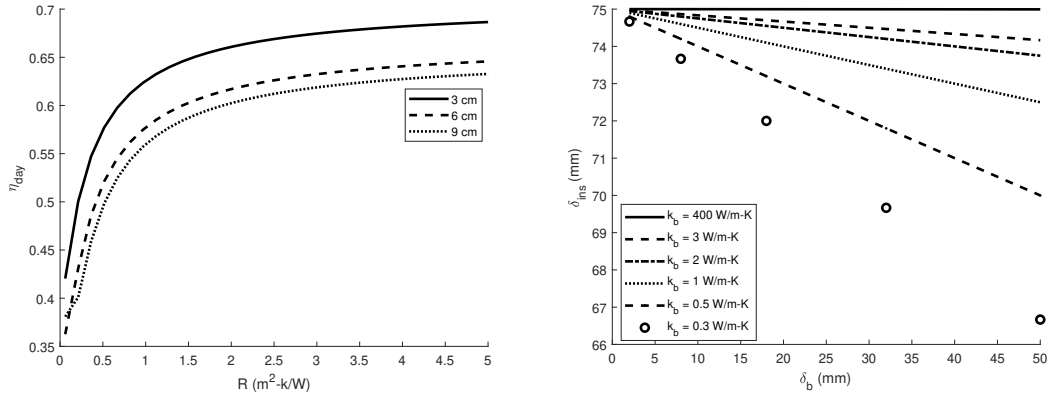

Figure 6.2: Variation of solar still performance with (a) bottom heat transfer resistnc for basin water depth of 3 cm, 6 cm and 9 cm; (b) Corresponding variation of insulation thickness with basin thickness for ($R = 1.5$ m^2-K/W)

heat transfer rate. It is observed that an optimum bottom heat transfer resistance (R) of 1.5 m^2-K/W is desirable for high solar still performance. The corresponding inter-dependency of the solar still basin thickness and solar still insulation is shown in Fig. 6.2(b). A thermal conductivity for the insulation of 0.05 w/m-K is considered here, while the basin conductivity can be anywhere from 0.3 W/m-K to 400 W/m-K based on the material considered [126]. Interestingly, it is observed that increasing the basin thickness from 1 mm to 5 mm does not change the required insulation thickness by much, even for low basin thermal conductivity, indicating the influence of the basin is less on the bottom heat transfer coefficient. For 0.05 W/m-k, a thermal insulation thickness of 3" (7.5 cm) is desirable. If

a more practical value of 0.038 W/m-K is used, the required thermal insulation thickness must be at least 2" (≈5 cm).

6.2 Candidate solar still materials

Based on the above mentioned conditions and the relevant literature, the following materials are considered to be suitable for the components of the solar still.

1. Cover (4 mm thick): Borosilicate glass, sodalime glass, silica glass.

2. Basin (gauge 26): stainless steel (SS), galvanized steel (GS), brass, copper, granite (8 mm tile), sand stone (10 mm tile), and glass FRP (GFRP) 4 mm thick (these are some of the smallest commercially available sizes).

3. Thermal insulation (R=1.5 m^2-K/W): Expanded polystyrene (EPS), extruded polystyrene (PS), polyurethane foam (pUF), glass wool (GW), rock wool (RW), fiber glass (FG), wood fiber (WF), sheep wool (SW), and cork.

4. Body : Concrete, granite, sandstone, limestone, wood, and GFRP.

5. Sealant: silicone epoxy (0.5 kg/m^2), glass putty (1 kg/m^2), and EPDM gasket (4 m/m^2).

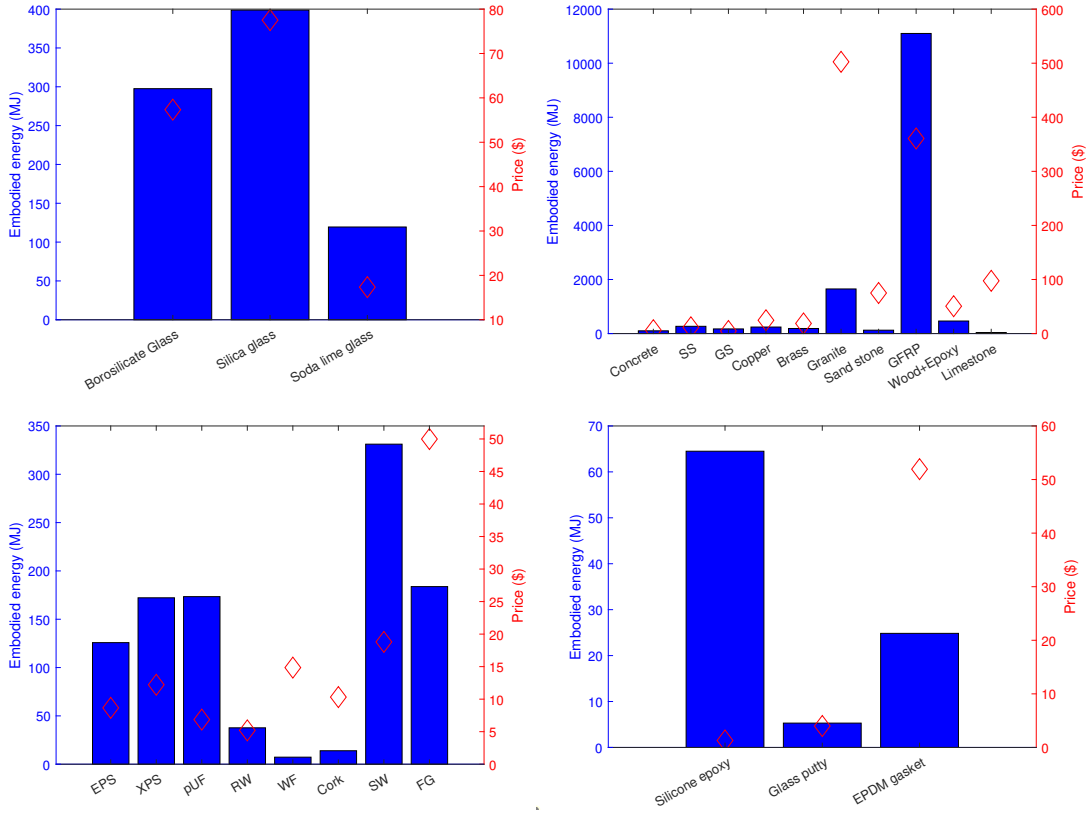

Figure 6.3: Embodied energy and cost of candidate (a) cover, (b) Basin and body, (c) thermal insulation and (d) sealant materials for constructing a 1 m^2 solar still

Embodied energy (EE) is the energy consumed to produce a unit component, and here it is scaled for a 1 m^2 solar still. The embodied energy of the material, and its corresponding cost for making a 1 m^2 solar still is shown in Fig. 6.3. It is expected that the total solar still embodied energy and the cost linearly increase with the solar still area due to the increase in the system weight. The material properties for the cover, basin and body, and sealants are taken from

[126, 127, 128]. The corresponding embodied energy and cost of the thermal insulation material are considered from [129, 130, 131, 132, 133, 134, 135, 136]. It is observed that glass fiber reinforced plastic is commonly used in the literature, despite being more energy intensive compared to other alternatives for basin and solar still body materials.

6.2.1 Life cycle energy conversion

The net annual energy for desalination (E_{out}) is the product of total annual distillate produced and the latent heat of energy. The life time energy conversion of the system is thus the ratio of net life time energy output and the solar energy input, as:

$$LCEC = \frac{E_{out} * n - EE}{Q_{solar} * n} \tag{6.2}$$

where, n is the solar still life in years. The net $CO_{2-\text{eq}}$ emission mitigation (ϕ_{CO_2}) can be calculated as:

$$\phi_{CO_2} = (E_{out} * n - EE) * EF \tag{6.3}$$

Where, EF is the emission factor of natural gas mix, which is 0.0694 kg $CO_{2-\text{eq}}$/MJ [130]. An annual CO_2 mitigation credit of $ 15/ton can be applied as emission mitigation which is multiplied with ϕ_{CO_2}. This carbon credits cost is applied only in the optimistic case, which will be discussed in the following sections. The

energy payback time of the solar still can be calculated as:

$$EPBT = \frac{E_{out}}{EE} \tag{6.4}$$

6.2.2 Results: Low-cost materials combination

All possible combinations from the candidate materials are investigated to yield a low cost solar still and faster energy payback time where the results are shown in Table 6.1.

Table 6.1: Resulting prices and $EPBT$ for different solar still material combinations

Cover	**Basin**	**Thermal insulation**	**Body/ frame**	**Sealant**	**Solar still cost ($/m^2)**	$EPBT(years)$
Sodalime glass	GS	RW	Concrete	Silicone	32.55	0.25
Sodalime glass	GS	pUR	Concrete	Silicone	34.22	0.33
Sodalime glass	GS	RW	Concrete	putty	35.25	0.25
Sodalime glass	GS	EPS	Concrete	Silicone	36.01	0.31
Avoid combination below						
Silica glass	Granite tile	Cork	Granite	Gasket	731.16	1.11
Borosilicate glass	Granite tile	FG	Granite	Gasket	742.18	1.01
Silica glass	Granite tile	FG	Granite	Gasket	762.36	1.05

It is observed that, with careful selection of materials, a solar still costing less than $ 35/m^2 can be deployed as a stand alone desalination unit, with an $EPBT$ of only 0.25 to 0.3 years. The cost of dispersions at 0.1% concentration with biochar are expected to be inconsequential at around only $ 0.05-0.1/m^2. The reason is, commercial biochar could be purchased at only $ 150/ton. Even at a high conservative cost of $ 1000/ton of crushed biochar, the amount of biochar needed for 1 m^2 solar still for the said concentration is only about 40 grams for

40 liters of water (at 1 g/L concentration, as the biochar density is between 1500 kg/m^3 to 2000 kg/m^3), indicating the cost of biochar used in the solar still to be only \$ 0.04/m^2. For the lowest annual freshwater productivity scenario, the computed annual carbon credits for a system generating only 700 L/m^2-yr ($\approx$2 L/m^2-day) is approximately \$ 7.8/m^2-yr. The last three rows shows possible material combinations that result in a high system CAPEX, and thus must be avoided.

6.3 Distillate production in California

Solar still distillate production is calculated from the theoretical heat and mass transfer equations mentioned earlier in Chapter 5. The solar irradiation, ambient temperature and wind velocity data are obtained from the Cooperative Institute for Meteorological Satellite Studies (CMISS) public repository [2]. These data are derived from GOES-West satellite imagery using the Daytime Cloud Optical and Microphysical Properties Algorithm (DCOMP) [137]. The annual mean daily global irradiance in kW/m^2/day, mean ambient temperature, and mean wind velocity are shown in Fig. 6.4.

Figure 6.5(a) shows the estimated annual freshwater productivity rate in California for 96% plant availability. The productivity varies between 974.1 and

[2] ftp://ftp.ssec.wisc.edu/clavr/

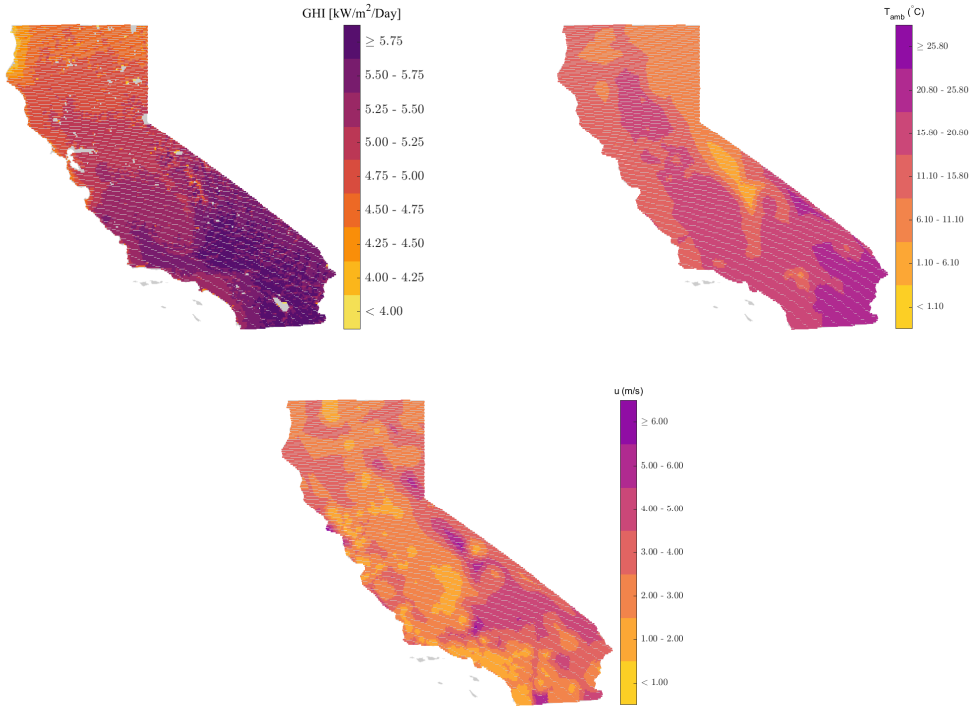

Figure 6.4: Annual mean (a) daily global irradiance, (b) ambient temperature and (c) wind velocity in the state of California

1080.3 L/m^2-year with a median productivity of 1012.5 L/m^2-year (2.9 L/m^2-day). While, the freshwater productivity rate is predominantly dependant on the incident solar irradiation, it can be observed from the Fig. 6.4 that the ambient temperature and wind velocity influence the freshwater productivity rate, as also noted by [138]. For example, in the south Californian region where the estimated solar irradiation and ambient temperature are high, the low wind velocity in most of the region does not cool the cover compared to the small region where the

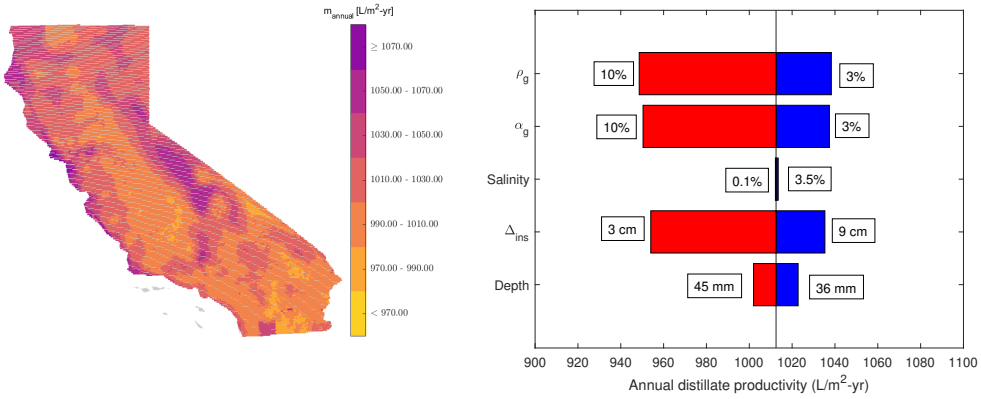

Figure 6.5: (a) Annual solar still productivity in California (b) Parametric sensitivity of variables influencing solar still productivity

wind velocity is high, thereby, the freshwater productivity is most of the region is low. Likewise, same inference can be drawn from the mountainous region (Eastern side) of the state. The moderate temperatures and global irradiation along the coastal regions of the state and wind speeds higher than 2 m/s could give rise to a high temperature difference between the evaporating pool and the condensing cover, thereby increasing the productivity. However, the total variation in annual freshwater productivity is only 106.2 L/m^2-year, hence, it can be estimated that the freshwater production through the state is almost uniform. The mass of water evaporating from the water pool is about 0.7%, with some seasonal variation. The parametric sensitivity influence of solar still productivity is analyzed for several parameters. The solar still productivity is independent of material prop-

erties except for cover absorptivity and reflectivity which seem to influence the productivity the most. For 10% cover abosrptivity and reflectivity, the median solar still productivity is estimated at around 950 L/m^2-year, which is 6.2% lower than the base case median estimate. A value of 3% increases freshwater median productivity to 1038 L/m^2-year, which is a gain of 2.1%. Smaller insulation thickness of 3 cm increases heat losses, therefore the productivity drops to about 954 L/m^2-year (by 5.77%), and since 6 cm thickness is about optimal, increasing the insulation thickness to 9 cm has less influence on productivity gain, which is estimated to be 1035.3 L/m^2-year (by 2.2% only). Depth has some small influence, where increasing the depth to 45 mm reduces the productivity by only 1.03% to 1002 L/m^2-year, and reducing the depth to 36 mm increases the productivity by only 1.01% to 1022.8 L/m^2-year. Feed water salinity has negligible influence in solar still productivity.

6.4 Economic feasibility

Solar still freshwater production rate is a linear function of the basin area. Among cost components, some vary linearly with area, but several cost variables vary non-linearly with area or productivity.

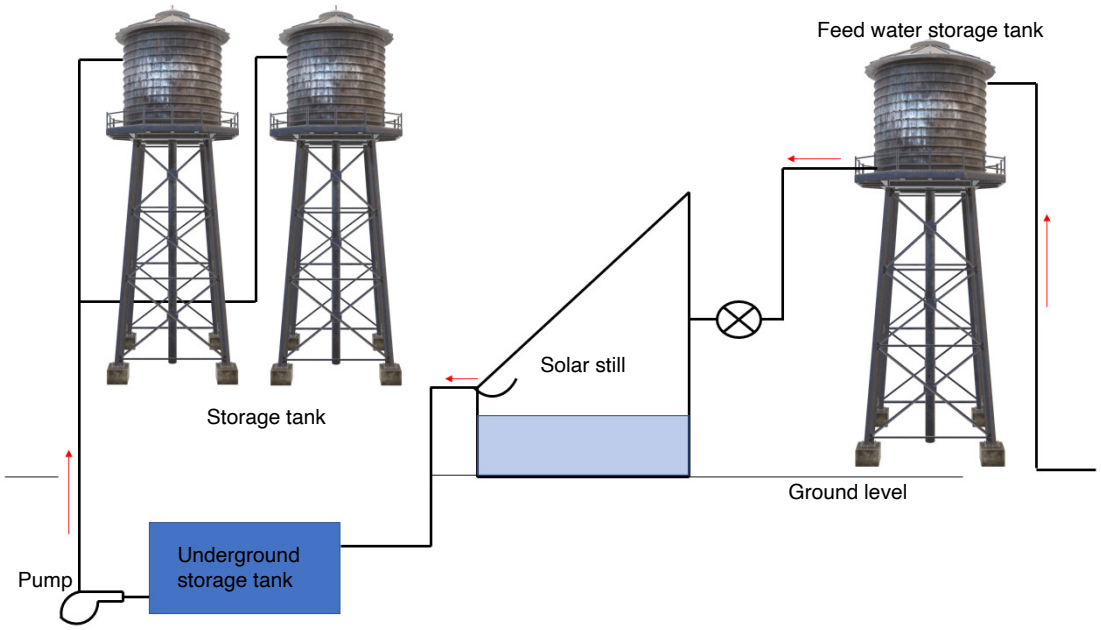

Figure 6.6: Solar still system configuration

The solar still desalination system configuration considered is shown in Fig. 6.6. The cost items are shown in Table 6.2. Cost variations of commercial items of storage tanks and excavation cost vary with productivity, and so power law-relationships are developed as a function of productivity (m_{annual}). As a conservative approach, a solar still cost of \$ 40/m^2 is considered.

Figure 6.7 shows the variation of *LCOW* with solar still size and productivity. As expected, the *LCOW* decreases with increasing size, with a small 10 m^2 solar still yielding an *LCOW* of \$ 59.47/m^3 (for 900 L/m^2-year) and \$ 49.11 /m^3 (for 1100 L/m^2-year), decreasing to \$ 7.71 /m^3 (for 900 L/m^2-year) and \$ 6.36/m^3 (for 1100 L/m^2-year) for a 10000 m^2 solar still. For a given area, the *LCOW* is low

Table 6.2: System cost for solar still desalination plant for the chosen configuration

Cost element	**Cost**	**Comments**	**Reference**
Saline feed pump	\$ 750	72 m^3/h pumping rate, 1 year warranty	[139]
Fresh water pump	\$ 150	3.6 m^3/h pumping rate, 1 year warranty	[140]
Feed storage tank	\$ $1610.1 * m_{annual}^{0.6373}$	Power law as function of volume > 50 m^3 [141]	[142]
Distillate storage tank	\$ $1680.8 * m_{annual}^{0.6085}$	Power law as function of volume < 50 m^3 [141]	[142]
Underground storage tank	\$ $411.78 * m_{annual}^{0.8693}$	Power law as function of volume [141]	[143]
Excavation	\$ $646.33 * m_{annual}^{0.624}$	Power law as function of volume [141]	[144]
Piping	\$ 1500	\$ 1.5/ foot for CPVC pipe	[145]
Labor maintenance	\$ 0.5/m^2	value between \$ 0.1-0.6/m^2	[146]

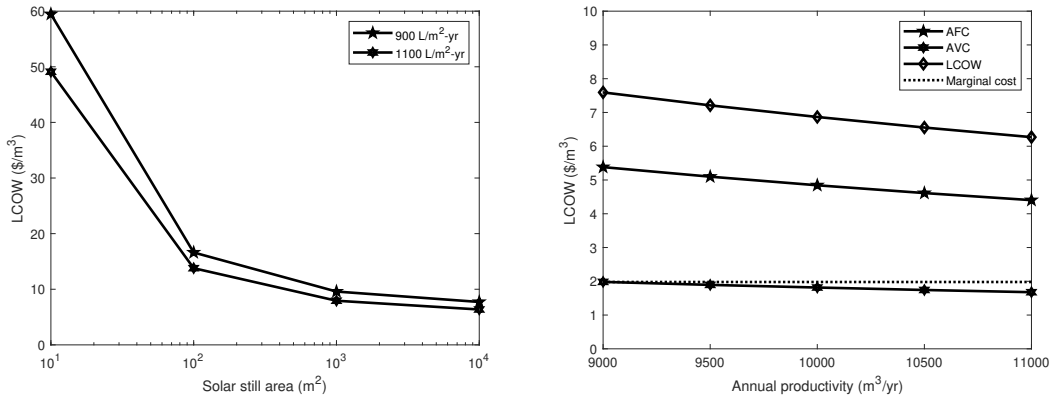

Figure 6.7: (a) Variation of *LCOW* with solar still size, (b) Variation of *LCOW* and with annual productivity for 10000 m^2 solar still

with higher productivity as shown in Fig. 6.7 (b). For a closer inspection, the cost components are divided into average fixed cost (AFC) and average variable cost (AVC). While it is expected that the average fixed cost remains constant, here the value changes with productivity since some capital cost components do not linearly vary with the solar still size but vary according to the cost correlation mentioned above. For the nominal cost parameters of 5% discount rate and 25 years plant

life, the *LCOW* is found to be higher than the marginal cost of water supplied at 1.5% of mean household income (MHI) [147], but still within acceptable limit reported by [146].

6.4.1 Parametric sensitivity of cost components

It has been previously shown that the cost of water produced by a solar still is highly sensitive towards the capital cost, hence the need to verify the sensitivity of cost variation of solar stills. In addition, discount rate, labor costs and ancillary components are other cost components that feature in the cost of water calculation, and so their influence must also be verified.

Figure 6.8 shows parametric sensitivity of cost components on the *LCOW*. As noted, capital cost has the highest influence on the *LCOW*, with the cost of water being as high as \$ 13.06/m^3 for a solar still costing \$ 100/m^2. The next highest influence is from discount rate, which at a high value of 8%, the *LCOW* increases from the base line value of \$6.89/m^3 to \$ 8.47/m^3. Availing carbon credits at \$ 15/*ton* of $CO_{2\text{-eq}}$ emissions abated, the *LCOW* in fact decreases to \$ 5.21/m^3. The labor cost, ancillary components such as tanks and excavation, salvage value have been found to have some influence on the cost of water.

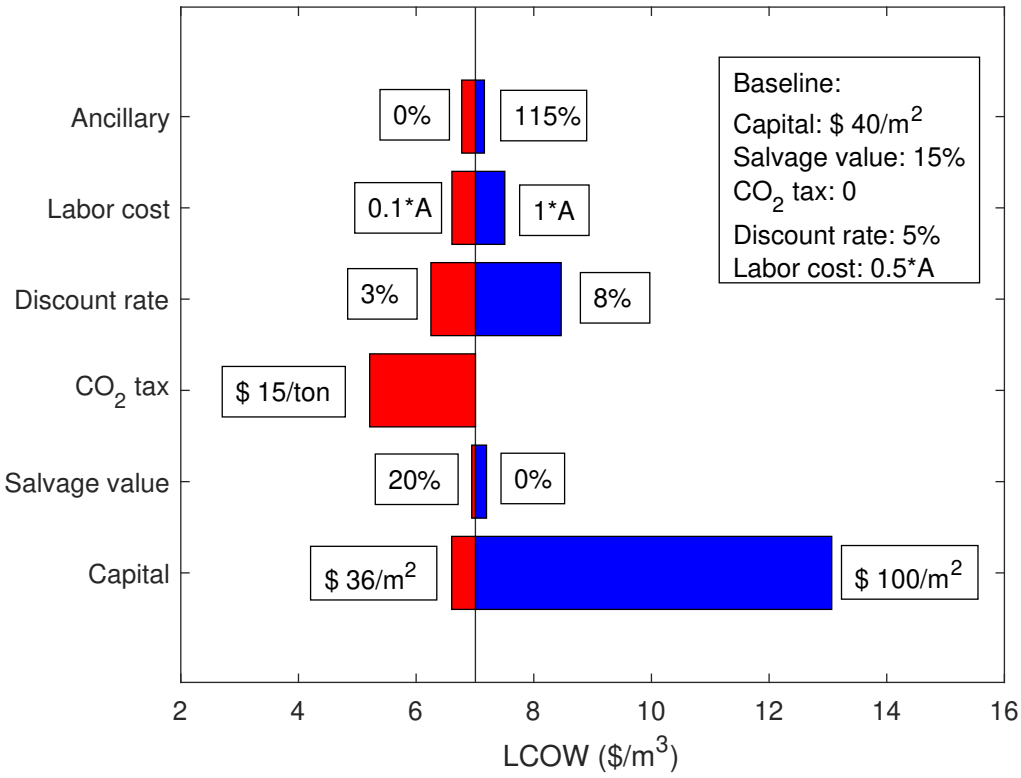

Figure 6.8: Parametric sensitivity analysis on cost of water

6.4.2 Results: cost of water produced

The feasibility of solar still is evaluated by determining the cost of water produced from the solar still system, for three cases. The optimistic case refers to a feasible operational conditions with discount and other cost components mentioned in the left side values in Fig. 6.8, and a condition where the low-cost solar absorber particles are replaced once every 10 years. This is a feasible option since

these particles can be washed and reused. Similarly, the pessimistic scenario refers to the condition with the values in the right side box in Fig. 6.8.

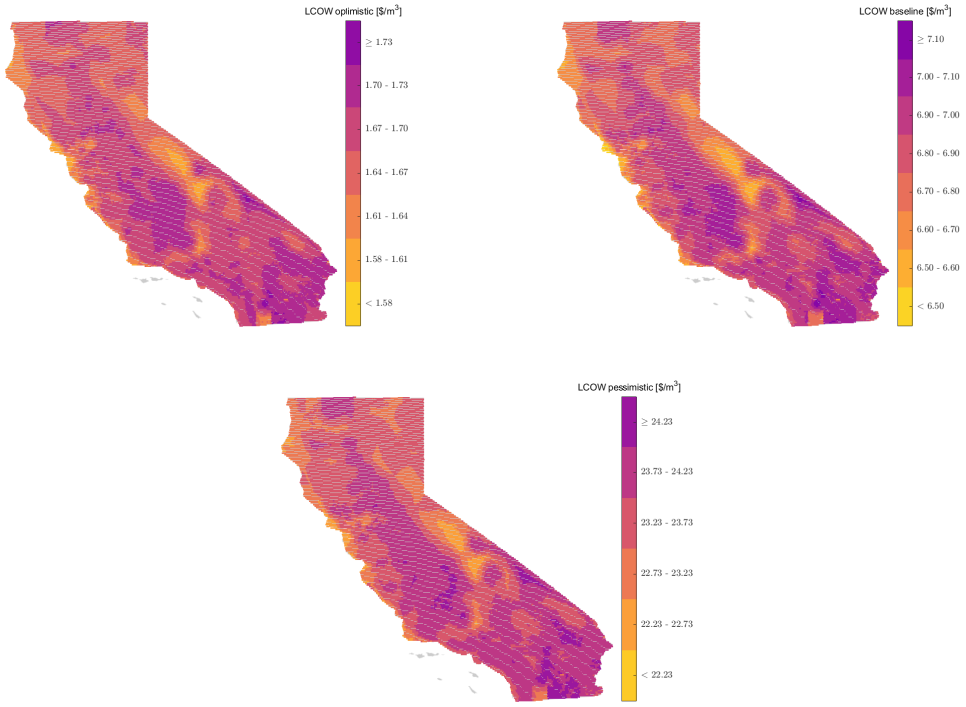

Figure 6.9: *LCOW* distribution map in California for (a) optimistic case; (b) baseline case; and (c) pessimistic case

Figure 6.9 shows the map of *LCOW* distribution of solar still from the production perspective for the three cases (a) optimistic, (b) baseline case and (c) pessimistic case. In the base case, the *LCOW* varies between \$ 6.47/m^3 and 7.14/m^3 with a median of \$ 6.88/m^3. In the optimistic case, which incorporates realistic elements, the *LCOW* varies between \$ 1.58/m^3 and 1.74/m^3, which is

lower than the marginal cost of water supplied at 1.5% MHI, which is \$ 1.98/m^3. The estimated median of cost of water produced is \$ 1.68/m^3. It is to be noted that the *LCOW* presented here is for the desalination process only, and that the other cost elements of feed water intake, pre-treatment and post-treatment are not included. One advantage here is that there is no requirement for continuous brine disposal since the solar still basin and the feed water storage tanks can hold water for a long time until the plant maintenance. In the pessimistic scenario, the *LCOW* varies between \$ 22.62/m^3 and 24.62/m^3. This is still acceptable given the size of freshwater production, while comparing with the other alternative desalination technologies.

6.4.3 Comparison to alternative PV-RO technology

In Chapter 5, it is shown that a solar still can produce water at costs lower than or comparable to widely used photovoltaic-reverse osmosis (PV-RO) technology. Similar comparison is performed here to assess the scope of using solar stills over PV-RO, since a recent report suggests that PV-RO is the most preferable option for desalination [148]. For this purpose, 1000 m^2 solar PV area is considered to produce freshwater at similar rates of production. In the cost assessment, feed water storage tank, excavation and underground storage tank costs are not considered.

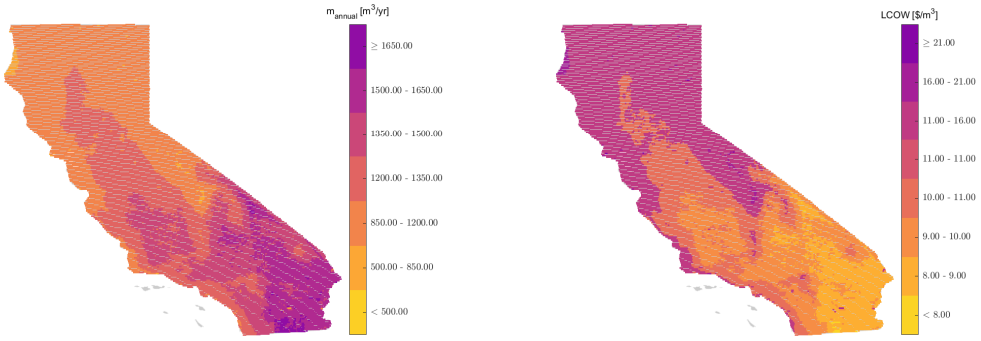

Figure 6.10: (a)Annual distillate productivity of a PV-RO system, (b) corresponding *LCOW* from the PV-RO system

It is observed that, from the PV-RO system, annual distillate productivity has a wide range from 578.53 to 1739.7 m^3/year with a median of 1264.3 m^3/year. The reason for this wide range could be due to the PV performance being susceptible to the ambient conditions, while another assumption is that the feed water temperature is the same as that of the ambient temperature. If RO membrane pressure does not reach the minimum threshold of 40 bar, permeate is not produced. It is observed that PV-RO has less productivity in northern Californian region, but high productivity for the same size in southern Californian region. Based on this productivity, the estimated *LCOW* for the PV-RO technology is between $ 7.7/m^3 and 23.1/m^3 with a median value of $ 10.6/m^3.

Figure 6.11 shows the direct cost of water produced from the solar still and the PV-RO system. It is observed that the cost of water produced from the solar stills

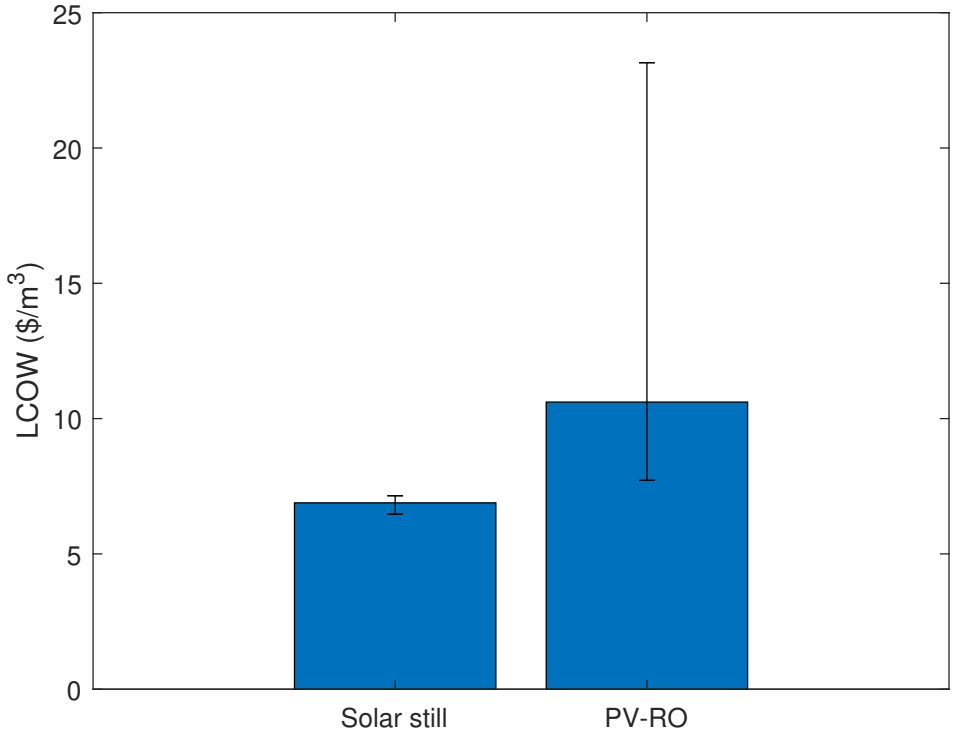

Figure 6.11: Comparison of cost of water between solar still and PVRO

is lower than the PV-RO system, while also being more uniform in comparison the the PV-RO system. Along with the system capital cost that is significantly different between the solar stills and the PV-RO system, the anticipated operational cost in the case of solar stills is only around $ 34,229/year as compared to $ 95,642/year with PV-RO system. The main reasons for differences in the operational costs is because of the expert operational supervision required by the PV-RO as opposed to less maintenance oversight in the solar still system, and the

annualized high replacement costs for the PV-RO system as already discussed in Chapter 5. In addition to the cost of water produced, other cost elements such as brine intake, brine and freshwater treatment costs, and brine disposal costs are considered while calculating the final cost of water supplied. PV-RO system requires continuous brine disposal which could potentially increase the final cost of water supplied [149], while the solar still basin water replacement rate is significantly lower until it's salinity reaches a higher value of around 8%, at which point, it was observed by Hoque et. al [5] that the solar still performance drops by 7.28% at salinity higher than this.

6.5 Brine management strategy and cost

With make up water from the feed water tank compensating the evaporated mass in the solar still, using salt concentration balance equations, it is estimated that the solar still system takes about 2 weeks to reach a salinity levels close to 7.9% in the basin. As salt concentration approaches 8% in the solar still, the saline water in the basin can be disposed of using brine management techniques. With this limitation, the brine disposal for solar stills is expected to be carried out for 25 times in a year, while for the PV-RO system, the brine disposal occurs continuously.

Several disposal methods have been identified in literature such as deep well injection, sewer disposal, surface water disposal, evaporation pond or zero liquid discharge [150]. Evaporation ponds and deep-well injection, and surface water discharge might be economical methods for brine management, especially for small plants [151]. Evaporation ponds are easy to construct and maintain, but they require large areas, which might not be available at the plant locations.

Cost of brine management for both systems is determined using the appropriate cost models proposed by Mickley [152]:

$$CAP_{ep,unit} = 5406 + 465t_l + 1.07C_l + 0.931C_c + 217.5d_h \tag{6.5a}$$

$$CAPEX_{dw,inj} = 1000(-288 + 145.9d_t + 0.754D) \tag{6.5b}$$

Where, $CAP_{ep,unit}$ and $CAPEX_{dw,inj}$ are capital cost of setting of the evaporation pond per unit area (in acres) and total capital cost of deep well injection. t_l, C_l, C_c and d_h are the thickness of the clay liner, land cost, land clearing cost and the dike height in the evaporation pond. While it is assumed that the land is already available, the corresponding values for other parameters are: 50 mils (1 mils = 1/1000 of an inch) clay liner, land clearing cost of $ 1000/acre [153] and dike height of 10 ft [152]. In the case of the deep well injection system, d_t and D are the diameter of the tube and well depth. It is recommended by Mickley [152] that the recommended brine injection velocity be 3 m/s. A well depth of 1000

ft was assumed here as a nominal value presented by [152]. Based on the above equations, in the case of PV-RO system, if an evaporating pond is constructed to accommodate brine for at least 1 year, then for a 10 ft dike height, total capital costs are around $ 323,972 with only 0.5% of this cost required for operational management. Likewise, for the solar still, the expected cost to setup the evaporation pond is $ 257,272. The cost of brine disposal with this method is expected to be around $ 1.44/m^3 for both the systems. Literature shows the typical cost of disposal observed with this practise is between $ 1.18and 10.04/m^3 [150, 154]. On the other hand, in the case of deep-well injection, the calculated cost is $ 9.1/m^3 for solar stills and $ 7.2/m^3 for PV-RO system. This is higher than what is observed by [150]. While it is observed that the cost of disposal by evaporation pond is significantly lower than the deep-well injection, it must be emphasized that the land area required to have evaporation ponds is in the order of 8 to 10 acres (32000 to 40000 m^2), thereby consuming significant land area. In the case of brine disposal to the nearby water source, if a 12" pipe is used to transport brine and operated by a pump of 75% efficiency, the disposal cost assuming $ 0.15/kWh for electricity is expected to be $ 0.14/m^3/km of brine transport distance for PV-RO system. In the case of a solar still, the same is expected to be $ 0.1/m^3/km of brine transport, excluding the piping costs. Ziolkowska and Reyes noted that the cost of brine disposal could be between $ 0.33-0.66/m^3 [150].

The possibility of disposal to the open water sources and sewers could potentially displace the natural eco-habitat of the accepting water source, hence, appropriate permissions and licenses must be taken from the local water management body. Zero liquid discharge with brine concentrator and crystallizer integrated with the PV-RO system results in brine disposal cost of $ 14/m^3 with the system costs mentioned in [155]. In crystallizers, the brine is supersaturated with respect to all salts, thereby the byproduct is only commercial grade salts [155]. From the literature, cost of brine disposal for liquid discharge between $ 0.66 and 26.41/m^3 is observed [150, 154].

With the analysis performed, it is seen that the cost of water produced from the solar still is lower than that of the PV-RO system, while the cost brine disposal for both the systems could be comparable to one another. Since the solar still is a simple mechanical structure compared to the PV-RO system which has complex parts, maintenance of the solar stills relatively much simpler than the PV-RO system as they require continuous supervision. In an actual application standpoint, with regards to the rural regions, it is easier to install, operate and maintain a solar still system, while also being able to produce water at lower costs for the community, thereby increasing access to freshwater in the rural regions.

6.6 Highlights

- Solar still can be constructed from easily available materials such as soda-lime glass, galvanized steel sheet, concrete at costs lower than \$ 35/m^2 with thermal insulation such as rock wool, polyurethane foam, and expanded polystyrene.

- Sensitivity analysis of operational parameters showed that cover absorptivity and reflectivity assert the most influence on freshwater production rate at around 6%.

- Uniform cost of freshwater production can be obtained from solar stills at a nominal cost of \$ 6.47/m^3 to \$ 7.14/m^3, and with favorable incentives, the cost of freshwater production can be only \$ 1.58/m^3 to 1.74/m^3.

- In the context of actual application in the rural regions, it is much simpler to install, operate and maintain the solar still, compared to the complex PV-RO system which requires continuous expert supervision.

Chapter 7

Conclusions and Recommendations

7.1 Conclusions

The photo-thermal effect of carbon dispersions such as biochar and activated carbon in water is investigated with the purpose of enhancing water evaporation. This effect can be utilized in solar stills used for increasing access to clean water for small low-income communities.

Enhancement in photo-thermal conversion is analyzed according to Rayleigh scattering, Mie scattering and geometric optics for the respective size of the particle dispersion. For small particles, optical constants have a significant influence

on this phenomenon, and parameters such as particle size and dispersion concentration can be chosen in order to maximize the performance. In most cases where the refractive index (n) of carbon is around 1.5, and the absorption coefficient (k) is between 0.01 and 0.1, the optimal dispersion concentration is around 0.1% for full solar absorption, and high heat localization. When the volumetric heat source term resulting from this photo-thermal conversion is included, water evaporation enhancement rate is observed. While, the evaporation efficiency of water is nominally only around 10%, the evaporation efficiency increases to almost 43% by adding these dispersion particles.

This increase in evaporation rate of water by particles is experimentally observed by using two biochar particles, ponderosa pine (PP) and walnut shell (WS). They are physico-chemically and optically characterized showing high carbon content forming stable dispersions in water and high solar absorptivity. Outdoor experiments indicate that the total evaporation rate of water can be more than 1 kg/m$^2-$h by using these particles, while, that for pure water, it is only 0.55 kg/m$^2-$h.

Thermal performance and economic assessment of using these low-cost carbon dispersions in solar stills for small scale community desalination is performed. Two coastal locations were selected, Big sur (U.S.A) in northern hemisphere and Chañaral (Chile) in southern hemisphere. The productivity, annual greenhouse

gas emissions abated and cost of water produced for a 1000 m^2 solar area is computed and compared against photovoltaic seawater reverse osmosis (PV-SWRO) and solar flat plate collector integrated humidification dehumidificaion (FPC-HDH) system. It is observed that the productivity of the solar still is around 3.5 m^3/day, while that of the other two systems is around 4.5-5 m^3/day. However, the cost of water produced from the solar still is found to be lower than the other two systems, since the capital investment ($CAPEX$) and the operational expenditure ($OPEX$) incurred from the solar still is far lower than the other two systems.

The analysis of solar stills has weak dependence on the materials as long as suitable insulation and high cover transmittance are provided. Several materials combination are investigated to yield a low-cost solar still such that the capital cost of the system is very low, while also having faster payback time (low embodied energy of the system). It is identified that several combinations of materials can be used to yield a solar still costing $< \$\ 35/m^2$ with almost no compromise in productivity. The feasibility of producing a low-cost community scale freshwater (for about 100 households) is investigated by using a new solar still system, including tanks and excavation for a 25 year plant life with a low-cost solar still. A conservative estimate showed that the cost of water produced can be expected to be between \$ 6.47/m^3 and 7.14/m^3 in California, while, with feasible invest-

ment options, the cost of water produced can be as low as \$ 1.58/m^3 to 1.74/m^3. It is expected that the total cost of water supplied is around the marginal cost of water at 1.5% mean household income, which is around \$ 1.98/m^3 in California. Likewise, solar stills being simple to install, operate and maintain makes it more advantageous over other competing desalination technologies for producing low-cost freshwater in the rural regions. An overall life cycle greenhouse gas assessment (LCA) for a particular low-cost system discussed in Appendix B showed that the emissions for producing 1 m^3 of water is only 1.33 kg $CO_{2\text{-eq}}/m^3$, and is competitive with a more matured PV-RO system, whose life cycle emissions are around 1.53 kg $CO_{2\text{-eq}}/m^3$.

With this analysis, it is suggested that solar stills, incorporating low-cost carbon dispersion particles as solar absorbers, can enhance the solar still productivity and at a low cost.

7.2 Future recommendations

Several potential research gaps were identified during the course of this dissertation.

Under 1 sun (1000 W/m^2) condition, the maximum theoretical evaporation rate of water is around 1.4 kg/m^2-h. Several researchers have developed efficient

solar absorber materials with high absorptivity, and have reported evaporation rates in the range of 1.1-1.3 kg/m^2-h. Since this is almost the upper limit, the focus should be on the cost of the solar absorber material, which is one of key aspects of this work. The term low-cost black carbon is broadly used with some references to locally available activated carbon, and biochar materials. These black carbon materials are pyrolyzed biomass, and so the solar absorptivity depends on the processing conditions. In addition to increasing the solar absorptivity content, the hydrophilic and hydrophobic character must be suitably modified. When used as floating strucutres, careful analysis should be performed with regards to the water affinity and pore sizes, since some discrepancy is observed in the literature with regards to whether hydrophilic character or hydrophobic character is better. In dispersion form, which is the focus of this dissertation, appropriate pyrolysis condition must be identified. It is observed that a very high temperature results in a less stable carbon, but high temperature is needed for high solar absorptivity. It is imperative to identify the optimal pyrolysis conditions for a given biomass composition.

While analyzing the performance of a solar still, several assumptions were made. One such aspect is with regards to treating the basin fluid as having uniform temperature, rather than identifying temperature distribution along the column for a given dispersion concentration. This assumption might be justified

for shallow basins, but as water depth increases in the basin, temperature distribution exists due to heat conduction and so, a distinction in the governing equation between the evaporating surface and the water mass must be applied. Further research could be directed towards identifying appropriate convective heat and mass transfer correlations. While several correlations exits, most of them are limited by their zone of applicability such as temperature limits or dimensionless group limitations. A general convective heat and mass transfer correlation accounting for thermo-physical-optical properties of the solar still, geometrical configuration and operational parameters must be developed.

The cost analysis in this work refers to the cost of water desalinated only following the procedural guidelines laid by several researchers. However, the result will underestimate the cost of actual system deployed, since water intake costs, treatment costs and brine disposal costs must be included. Appropriate size and cost correlations must be developed in that regard for different scales of water productivity from liters per day (LPD) to million liters per day (MLD) and to million cubic meters per day (MMD), and for different technologies like membrane system or thermal system.

Along with the cost scenario, one of the important aspects of renewable integrated desalination is that the system is environmentally friendly. Although the process of desalination is greenhouse gas emissions free, it is important that the

system has low overall emissions impact during its life cycle from cradle-to-grave. Some preliminary results are presented in Appendix B, but a more concrete analysis must be carried out. Also, it is identified that the discussion is limited to greenhouse gas emissions abatement at this point. However, considering the desalination system produces freshwater, it is important to account for the water footprint also.

Similar to the black absorbers increasing the distillate productivity by 66% for just 10 to 15% increase in system capital cost, if another improvement is identified, the possible integration must be investigated for furthering the scope of solar stills as low-cost desalination option.

Bibliography

[1] E. Jones, M. Qadir, M. T. van Vliet, V. Smakhtin, S. mu Kang, The state of desalination and brine production: A global outlook, Science of The Total Environment 657 (2019) 1343 – 1356. doi:https://doi.org/10.1016/j.scitotenv.2018.12.076.

[2] J. Schewe, J. Heinke, D. Gerten, I. Haddeland, N. W. Arnell, D. B. Clark, R. Dankers, S. Eisner, B. M. Fekete, F. J. Colón-González, S. N. Gosling, H. Kim, X. Liu, Y. Masaki, F. T. Portmann, Y. Satoh, T. Stacke, Q. Tang, Y. Wada, D. Wisser, T. Albrecht, K. Frieler, F. Piontek, L. Warszawski, P. Kabat, Multimodel assessment of water scarcity under climate change, Proceedings of the National Academy of Sciences 111 (9) (2014) 3245–3250. doi:10.1073/pnas.1222460110.

[3] Sebastian, Timeline of water desalination (2018).
URL `https://timelines.issarice.com/wiki/Timeline_of_water_desalination`

[4] H. Rabiee, K. R. Khalilpour, J. M. Betts, N. Tapper, Chapter 13 - energy-water nexus: Renewable-integrated hybridized desalination systems, in: K. R. Khalilpour (Ed.), Polygeneration with Polystorage for Chemical and Energy Hubs, Academic Press, 2019, pp. 409 – 458. doi:https://doi.org/10.1016/B978-0-12-813306-4.00013-6.

[5] Asiful Hoque, Ashif Hasan Abir, Kironmoy Paul Shourov, Solar still for saline water desalination for low-income coastal areas, Applied Water Science 9 (104). doi:https://doi.org/10.1007/s13201-019-0986-9.

[6] M. W. Shahzad, M. Burhan, L. Ang, K. C. Ng, Energy-water-environment nexus underpinning future desalination sustainability, Desalination 413 (2017) 52 – 64. doi:https://doi.org/10.1016/j.desal.2017.03.009.

[7] S. A. Kalogirou, Seawater desalination using renewable energy sources, Progress in Energy and Combustion Science 31 (3) (2005) 242 – 281. doi:https://doi.org/10.1016/j.pecs.2005.03.001.

[8] S. Kandasamy, M. Vellingiri, S. S. J. Balasundaram, Performance correlation for single-basin double-slope solar still, International Journal of Energy and Environmental Engineering 4 (4) (2013) 1–6. doi:https://doi.org/10.1186/2251-6832-4-4.

[9] K. Kalidasa Murugavel, S. Sivakumar, J. Riaz Ahamed, K. K. S. K. Chockalingam, K. Srithar, Single basin double slope solar still with minimum basin depth and energy storing materials, Applied Energy 87 (2) (2010) 514 – 523. doi:https://doi.org/10.1016/j.apenergy.2009.07.023.

[10] G. M. ZAKI, A. Al-TURKI, M. AL-FATANI, Experimental investigation on concentrator-assisted solar-stills, International Journal of Solar Energy 11 (3-4) (1992) 193–199. doi:10.1080/01425919208909739.

[11] P. Joshi, G. N. Tiwari, Effect of cooling condensing cover on the performance of n-identical photovoltaic thermal-compound parabolic concentrator active solar still: a comparative study, International Journal of Energy and Environmental Engineering 9 (2018) 473–498. doi:https://doi.org/10.1007/s40095-018-0276-6.

[12] A. Madhlopa, Development of an advanced passive solar still with separate condenser, Ph.D. thesis, University of Strathclyde (2009).

[13] A. E. Kabeel, Z. M. Omara, F. A. Essa, Enhancement of modified solar still integrated with external condenser using nanofluids: An experimental approach, Energy Conversion and Management 78 (2014) 493 – 498. doi:https://doi.org/10.1016/j.enconman.2013.11.013.

[14] H. E. S. Fath, M. El-Samanoudy, K. Fahmy, A. Hassabou, Thermal-economic analysis and comparison between pyramid-shaped and single-slope solar still configurations, Desalination 159 (1) (2003) 69 – 79. doi:https://doi.org/10.1016/S0011-9164(03)90046-4.

[15] T. Arunkumar, R. Velraj, D. Denkenberger, R. Sathyamurthy, K. Vinothkumar, K. Porkumaran, A. Ahsan, Effect of heat removal on tubular solar desalting system, Desalination 379 (2016) 24 – 33. doi:https://doi.org/10.1016/j.desal.2015.10.007.

[16] A. F. Muftah, K. Sopian, M. A. Alghoul, Performance of basin type stepped solar still enhanced with superior design concepts, Desalination 435 (2018) 198 – 209, desalination using Renewable Energy. doi:https://doi.org/10.1016/j.desal.2017.07.017.

[17] Z. M. Omara, A. E. Kabeel, M. M. Younes, Enhancing the stepped solar still performance using internal reflectors, Desalination 314 (2013) 67 – 72. doi:https://doi.org/10.1016/j.desal.2013.01.007.

[18] D. D. W. Rufuss, S. Iniyan, L. Suganthi, P. Davies, Solar stills: A comprehensive review of designs, performance and material advances, Renewable and Sustainable Energy Reviews 63 (2016) 464 – 496. doi:https://doi.org/10.1016/j.rser.2016.05.068.

[19] S. W. Sharshir, G. Peng, L. Wu, N. Yang, F. Essa, A. H. Elsheikh, S. I. T. Mohamed, A. E. Kabeel, Enhancing the solar still performance using nanofluids and glass cover cooling: Experimental study, Applied Thermal Engineering 113 (2017) 684 – 693. doi:https://doi.org/10.1016/j.applthermaleng.2016.11.085.

[20] T. Elango, A. Kannan, K. Kalidasa Murugavel, Performance study on single basin single slope solar still with different water nanofluids, Desalination 360 (2015) 45 – 51. doi:https://doi.org/10.1016/j.desal.2015.01.004.

[21] M. K. Gnanadason, P. S. Kumar, V. H. Wilson, G. Hariharan, N. S. Vinayagamoorthi, et al., Design and performance analysis of an innovative single basin solar nanostill, Smart Grid and Renewable Energy 4 (01) (2013) 88.

[22] S. W. Sharshir, A. Kandeal, M. Ismail, G. B. Abdelaziz, A. Kabeel, N. Yang, Augmentation of a pyramid solar still performance using evacuated tubes and nanofluid: Experimental approach, Applied Thermal Engineering 160 (2019) 113997. doi:https://doi.org/10.1016/j.applthermaleng.2019.113997.

[23] L. Sahota, S. Arora, H. P. Singh, G. Sahoo, Thermo-physical characteristics of passive double slope solar still loaded with mwcnts and al2o3-water based nanofluid, Materials Today: Proceedings 32 (2020) 344–349, innovative Advancement in Engineering & Technology. doi:https://doi.org/10.1016/j.matpr.2020.01.600.

[24] S. Sharshir, G. Peng, L. Wu, F. Essa, A. Kabeel, N. Yang, The effects of flake graphite nanoparticles, phase change material, and film cool-

ing on the solar still performance, Applied Energy 191 (2017) 358–366. doi:https://doi.org/10.1016/j.apenergy.2017.01.067.

[25] O. Neumann, C. Feronti, A. D. Neumann, A. Dong, K. Schell, B. Lu, E. Kim, M. Quinn, S. Thompson, N. Grady, P. Nordlander, M. Oden, N. J. Halas, Compact solar autoclave based on steam generation using broadband light-harvesting nanoparticles, Proceedings of the National Academy of Sciences 110 (29) (2013) 11677–11681. doi:10.1073/pnas.1310131110.

[26] A. Zeiny, H. Jin, G. Lin, P. Song, D. Wen, Solar evaporation via nanofluids: A comparative study, Renewable Energy 122 (2018) 443 – 454. doi:https://doi.org/10.1016/j.renene.2018.01.043.

[27] M. F. Modest, Chapter 12 - radiative properties of particulate media, in: M. F. Modest (Ed.), Radiative Heat Transfer (Third Edition), third edition Edition, Academic Press, Boston, 2013, pp. 387 – 439. doi:https://doi.org/10.1016/B978-0-12-386944-9.50012-1.

[28] K. H. Won, B. J. Lee, Effect of light scattering on the performance of a direct absorption solar collector, Frontiers in Energy 12 (1) (2018) 169–177. doi:https://doi.org/10.1007/s11708-018-0527-5.

[29] T. B. Gorji, A. Ranjbar, A review on optical properties and application of nanofluids in direct absorption solar collectors (dascs), Renewable and Sustainable Energy Reviews 72 (2017) 10–32. doi:https://doi.org/10.1016/j.rser.2017.01.015.

[30] S.-K. Chae, H. S. Lee, Determination of radiative transport properties of particle suspensions by a single-scattering experiment, Aerosol Science and Technology 18 (4) (1993) 389–402. doi:10.1080/02786829308959612.

[31] Y.-J. Dai, Y.-Q. Tang, W.-Z. Fang, H. Zhang, W.-Q. Tao, A theoretical model for the effective thermal conductivity of silica aerogel composites, Applied Thermal Engineering 128 (2018) 1634–1645. doi:https://doi.org/10.1016/j.applthermaleng.2017.09.010.

[32] J. I. Larruquert, L. V. R. de Marcos, J. A. Méndez, P. J. Martin, A. Bendavid, High reflectance ta-c coatings in the extreme ultraviolet, Opt. Express 21 (23) (2013) 27537–27549. doi:10.1364/OE.21.027537.

[33] Y. Shen, P. Zhou, Q. Q. Sun, L. Wan, J. Li, L. Y. Chen, D. W. Zhang, X. B. Wang, Optical investigation of reduced graphene oxide by spectroscopic el-

lipsometry and the band-gap tuning, Applied Physics Letters 99 (14) (2011) 141911. doi:10.1063/1.3646908.

[34] M. R. Querry, Optical constants (1985).

[35] H.-c. Chang, T. T. Charalampopoulos, Determination of the wavelength dependence of refractive indices of flame soot, Proceedings of the Royal Society of London. Series A: Mathematical and Physical Sciences 430 (1880) (1990) 577–591. doi:10.1098/rspa.1990.0107.

[36] C. Jäger, H. Mutschke, T. Henning, Optical properties of carbonaceous dust analogues, Astronomy & Astrophysics 332 (1998) 291–299.

[37] R. Johansson, T. Gronarz, R. Kneer, Influence of Index of Refraction and Particle Size Distribution on Radiative Heat Transfer in a Pulverized Coal Combustion Furnace, Journal of Heat Transfer 139 (4). doi:10.1115/1.4035205.

[38] M. Kuwahara, Y. Kim, R. Azumi, Measurement of the optical properties of a transparent, conductive carbon nanotube film using spectroscopic ellipsometry, Japanese Journal of Applied Physics 54 (7) (2015) 078001. doi:10.7567/jjap.54.078001.

[39] 911Metallurgist, Difference between crushing and grinding, \footnotesizehttps://www.911metallurgist.com/difference-between-crushing-grinding/ (2017).

[40] A. Mills, Mass Transfer, Prentice Hall, 2001.

[41] H.-J. Steeman, C. T'Joen, M. Van Belleghem, A. Janssens, M. De Paepe, Evaluation of the different definitions of the convective mass transfer coefficient for water evaporation into air, International Journal of Heat and Mass Transfer 52 (15) (2009) 3757 – 3766. doi:https://doi.org/10.1016/j.ijheatmasstransfer.2009.01.047.

[42] M. Shaker, E. Birgersson, A. S. Mujumdar, Extended maxwell model for the thermal conductivity of nanofluids that accounts for nonlocal heat transfer, International Journal of Thermal Sciences 84 (2014) 260 – 266. doi:https://doi.org/10.1016/j.ijthermalsci.2014.05.010.

[43] B. C. Pak, Y. I. Cho, Hydrodynamic and heat transfer study of dispersed fluids with submicron metallic oxide particles, Experimental Heat Transfer 11 (2) (1998) 151–170. doi:10.1080/08916159808946559.

[44] M. Quinn Brewster, Evaporation of water at high mass-transfer rates by natural convection air flow with application to spent-fuel pools, International Journal of Heat and Mass Transfer 116 (2018) 703 – 714. doi:https://doi.org/10.1016/j.ijheatmasstransfer.2017.08.035.

[45] M. T. Pauken, An experimental investigation of combined turbulent free and forced evaporation, Experimental Thermal and Fluid Science 18 (4) (1998) 334 – 340. doi:https://doi.org/10.1016/S0894-1777(98)10038-9.

[46] V. Ohri, V. Khullar, Using Solar Energy for Water Purification Through Nanoparticles Assisted Evaporation, Journal of Solar Energy Engineering 141 (1). doi:10.1115/1.4041099.

[47] S. Ishii, R. P. Sugavaneshwar, K. Chen, T. D. Dao, T. Nagao, Solar water heating and vaporization with silicon nanoparticles at mie resonances, Opt. Mater. Express 6 (2) (2016) 640–648. doi:10.1364/OME.6.000640.

[48] G. Ni, N. Miljkovic, H. Ghasemi, X. Huang, S. V. Boriskina, C.-T. Lin, J. Wang, Y. Xu, M. M. Rahman, T. Zhang, G. Chen, Volumetric solar heating of nanofluids for direct vapor generation, Nano Energy 17 (2015) 290 – 301. doi:https://doi.org/10.1016/j.nanoen.2015.08.021.

[49] M. M. Ghafurian, H. Niazmand, E. Ebrahimnia-Bajestan, H. Elhami Nik, Localized solar heating via graphene oxide nanofluid for direct steam generation, Journal of Thermal Analysis and Calorimetry 135 (2) (2019) 1443–1449. doi:10.1007/s10973-018-7496-0.

[50] X. Liu, X. Wang, J. Huang, G. Cheng, Y. He, Volumetric solar steam generation enhanced by reduced graphene oxide nanofluid, Applied Energy 220 (2018) 302 – 312. doi:https://doi.org/10.1016/j.apenergy.2018.03.097.

[51] X. Wang, Y. He, G. Cheng, L. Shi, X. Liu, J. Zhu, Direct vapor generation through localized solar heating via carbon-nanotube nanofluid, Energy Conversion and Management 130 (2016) 176 – 183. doi:https://doi.org/10.1016/j.enconman.2016.10.049.

[52] E. T. Ulset, P. Kosinski, B. V. Balakin, Solar steam in an aqueous carbon black nanofluid, Applied Thermal Engineering 137 (2018) 62 – 65. doi:https://doi.org/10.1016/j.applthermaleng.2018.03.038.

[53] W. Chen, C. Zou, X. Li, H. Liang, Application of recoverable carbon nanotube nanofluids in solar desalination system:

An experimental investigation, Desalination 451 (2019) 92–101. doi:https://doi.org/10.1016/j.desal.2017.09.025.

[54] X. Wang, G. Ou, N. Wang, H. Wu, Graphene-based recyclable photoabsorbers for high-efficiency seawater desalination, ACS Applied Materials & Interfaces 8 (14) (2016) 9194–9199. doi:10.1021/acsami.6b02071.

[55] D. Woolf, J. Amonette, F. Street-Perrott, J. Lehmann, S. Joseph, Sustainable biochar to mitigate global climate change, Nat. Commun. 1 (2010) 56. doi:10.1038/ncomms1053.

[56] S. Jeffery, F. G. A. Verheijen, M. van der Velde, A. C. Bastos, A quantitative review of the effects of biochar application to soils on crop productivity using meta-analysis, Agriculture, Ecosystems & Environment 144 (1) (2011) 175 – 187. doi:https://doi.org/10.1016/j.agee.2011.08.015.

[57] J. Lehmann, S. Joseph, Chapter 1 - biochar for environmental management: an introduction, in: J. L. . S. Joseph (Ed.), Biochar for Environmental Management Science, Technology and Implementation, Taylor & Francis Group, 2009, pp. 1–14.

[58] R. K. Gupta, M. Dubey, P. Kharel, Z. Gu, Q. H. Fan, Biochar activated by oxygen plasma for supercapacitors, Journal of Power Sources 274 (2015) 1300 – 1305. doi:https://doi.org/10.1016/j.jpowsour.2014.10.169.

[59] H. Li, X. Dong, E. B. da Silva, L. M. de Oliveira, Y. Chen, L. Q. Ma, Mechanisms of metal sorption by biochars: Biochar characteristics and modifications, Chemosphere 178 (2017) 466 – 478. doi:https://doi.org/10.1016/j.chemosphere.2017.03.072.

[60] T. M. Huggins, A. Haeger, J. C. Biffinger, Z. J. Ren, Granular biochar compared with activated carbon for wastewater treatment and resource recovery, Water Research 94 (2016) 225 – 232. doi:https://doi.org/10.1016/j.watres.2016.02.059.

[61] R. Chintala, J. Mollinedo, T. E. Schumacher, S. K. Papiernik, D. D. Malo, D. E. Clay, S. Kumar, D. W. Gulbrandson, Nitrate sorption and desorption in biochars from fast pyrolysis, Microporous and Mesoporous Materials 179 (2013) 250 – 257. doi:https://doi.org/10.1016/j.micromeso.2013.05.023.

[62] S. Jiang, T. A. H. Nguyen, V. Rudolph, H. Yang, D. Zhang, Y. S. Ok, L. Huang, Characterization of hard- and softwood biochars pyrolyzed at

high temperature, Environmental Geochemistry and Health 39 (2) (2017) 403–415. doi:10.1007/s10653-016-9873-6.

[63] C. E. Brewer, K. Schmidt-Rohr, J. A. Satrio, R. C. Brown, Characterization of biochar from fast pyrolysis and gasification systems, Environmental Progress & Sustainable Energy 28 (3) (2009) 386–396. doi:10.1002/ep.10378.

[64] S. Link, S. Arvelakis, H. Spliethoff, P. De Waard, A. Samoson, Investigation of biomasses and chars obtained from pyrolysis of different biomasses with solid-state 13c and 23na nuclear magnetic resonance spectroscopy, Energy & Fuels 22 (5) (2008) 3523–3530. doi:10.1021/ef800305g.

[65] R. Chintala, T. E. Schumacher, S. Kumar, D. D. Malo, J. A. Rice, B. Bleakley, G. Chilom, D. E. Clay, J. L. Julson, S. K. Papiernik, Z. R. Gu, Molecular characterization of biochars and their influence on microbiological properties of soil, Journal of Hazardous Materials 279 (2014) 244 – 256. doi:https://doi.org/10.1016/j.jhazmat.2014.06.074.

[66] K. Weber, P. Quicker, Properties of biochar, Fuel 217 (2018) 240 – 261. doi:https://doi.org/10.1016/j.fuel.2017.12.054.

[67] J. Wang, Z. Liu, X. Dong, C.-E. Hsiung, Y. Zhu, L. Liu, Y. Han, Microporous cokes formed in zeolite catalysts enable efficient solar evaporation, J. Mater. Chem. A 5 (2017) 6860–6865. doi:10.1039/C7TA00882A.

[68] V. L. Gaikwad, P. B. Choudhari, N. M. Bhatia, M. S. Bhatia, Chapter 2 - Characterization of pharmaceutical nanocarriers: in vitro and in vivo studies, in: A. M. Grumezescu (Ed.), Nanomaterials for Drug Delivery and Therapy, William Andrew Publishing, 2019, pp. 33 – 58. doi:https://doi.org/10.1016/B978-0-12-816505-8.00016-3.

[69] M. Gumustas, C. T. Sengel-Turk, A. Gumustas, S. A. Ozkan, B. Uslu, Chapter 5 - effect of polymer-based nanoparticles on the assay of antimicrobial drug delivery systems, in: A. M. Grumezescu (Ed.), Multifunctional Systems for Combined Delivery, Biosensing and Diagnostics, Elsevier, 2017, pp. 67 – 108. doi:https://doi.org/10.1016/B978-0-323-52725-5.00005-8.

[70] V. Gupta, P. Trivedi, Chapter 15 - in vitro and in vivo characterization of pharmaceutical topical nanocarriers containing anticancer drugs for skin cancer treatment, in: A. M. Grumezescu (Ed.), Lipid Nanocarriers for Drug Targeting, William Andrew Publishing, 2018, pp. 563 – 627. doi:https://doi.org/10.1016/B978-0-12-813687-4.00015-3.

[71] J. Lou, Y. Liu, Z. Wang, D. Zhao, C. Song, J. Wu, N. Dasgupta, W. Zhang, D. Zhang, P. Tao, W. Shang, T. Deng, Bioinspired multifunctional paper-based rgo composites for solar-driven clean water generation, ACS Applied Materials & Interfaces 8 (23) (2016) 14628–14636. doi:10.1021/acsami.6b04606.

[72] G. Hu, Y. Cao, M. Huang, Q. Wu, K. Zhang, X. Lai, J. Tu, C. Tian, J. Liu, W. Huang, L. Ding, Salt-resistant carbon nanotubes/polyvinyl alcohol hybrid gels with tunable water transport for high-efficiency and long-term solar steam generation, Energy Technology 8 (1) (2020) 1900721. doi:https://doi.org/10.1002/ente.201900721.

[73] L. Chen, S. Zhao, Q.-M. Hasi, X. Luo, C. Zhang, H. Li, A. Li, Porous carbon nanofoam derived from pitch as solar receiver for efficient solar steam generation, Global Challenges 4 (5) (2020) 1900098. doi:https://doi.org/10.1002/gch2.201900098.

[74] M. Hong, L. Zhang, Z. Tan, Q. Huang, Effect mechanism of biochar's zeta potential on farmland soil's cadmium immobilization, Environmental Science and Pollution Research 26 (19) (2019) 19738–19748. doi:10.1007/s11356-019-05298-5.

[75] M. M. Ghafurian, H. Niazmand, E. Ebrahiminia-Bajestan, Improving steam generation and distilled water production by volumetric solar heating, Applied Thermal Engineering 158 (2019) 113808. doi:https://doi.org/10.1016/j.applthermaleng.2019.113808.

[76] Honghong Lyu and Zebin Yu and Bin Gao and Feng He and Jun Huang and Jingchun Tang and Boxiong Shen, Ball-milled biochar for alternative carbon electrode, Environmental Science and Pollution Research 26 (2018) 14693–14702. doi:https://doi.org/10.1007/s11356-019-04899-4.

[77] M. M. Ghafurian, H. Niazmand, F. T. Dastjerd, O. Mahian, A study on the potential of carbon-based nanomaterials for enhancement of evaporation and water production, Chemical Engineering Science 207 (2019) 79 – 90. doi:https://doi.org/10.1016/j.ces.2019.05.043.

[78] H. Li, Y. He, Y. Hu, X. Wang, Commercially available activated carbon fiber felt enables efficient solar steam generation, ACS Applied Materials & Interfaces 10 (11) (2018) 9362–9368. doi:10.1021/acsami.7b18071.

[79] X. Luo, C. Huang, S. Liu, J. Zhong, High performance of carbon-particle/bulk-wood bi-layer system for solar steam generation, International Journal of Energy Research 42 (15) (2018) 4830–4839. doi:10.1002/er.4239.

[80] G. P. Narayan, M. H. Sharqawy, J. H. L. V, S. M. Zubair, Thermodynamic analysis of humidification dehumidification desalination cycles, Desalination and Water Treatment 16 (1-3) (2010) 339–353. doi:10.5004/dwt.2010.1078.

[81] M. A. Jones, I. Odeh, M. Haddad, A. H. Mohammad, J. C. Quinn, Economic analysis of photovoltaic (pv) powered water pumping and desalination without energy storage for agriculture, Desalination 387 (2016) 35 – 45. doi:https://doi.org/10.1016/j.desal.2016.02.035.

[82] N. Ahmad, A. K. Sheikh, P. Gandhidasan, M. Elshafie, Modeling, simulation and performance evaluation of a community scale pvro water desalination system operated by fixed and tracking pv panels: A case study for dhahran city, saudi arabia, Renewable Energy 75 (2015) 433 – 447. doi:https://doi.org/10.1016/j.renene.2014.10.023.

[83] N. Al-Bastaki, A. Abbas, Long-term performance of an industrial water desalination plant, Chemical Engineering and Processing: Process Intensification 43 (4) (2004) 555 – 558. doi:https://doi.org/10.1016/S0255-2701(03)00083-7.

[84] C. O. Popiel, J. Wojtkowiak, Simple formulas for thermophysical properties of liquid water for heat transfer calculations (from 0°c to 150°c), Heat Transfer Engineering 19 (3) (1998) 87–101. doi:10.1080/01457639808939929.

[85] G. N. Tiwari, S. K. Shukla, I. Singh, Computer modeling of passive/active solar stills by using inner glass temperature, Desalination 154 (2) (2003) 171 – 185. doi:https://doi.org/10.1016/S0011-9164(03)80018-8.

[86] S. Kumar, G. N. Tiwari, Analytical expression for instantaneous exergy efficiency of a shallow basin passive solar still, International Journal of Thermal Sciences 50 (12) (2011) 2543 – 2549. doi:https://doi.org/10.1016/j.ijthermalsci.2011.06.015.

[87] M. Feilizadeh, M. R. K. Estahbanati, A. Ahsan, K. Jafarpur, A. Mersaghian, Effects of water and basin depths in single basin solar stills: An experimental and theoretical study, Energy Conversion and Management 122 (2016) 174 – 181. doi:https://doi.org/10.1016/j.enconman.2016.05.048.

[88] S. Dehghani, A. Date, A. Akbarzadeh, Performance analysis of a heat pump driven humidification-dehumidification desalination system, Desalination 445 (2018) 95 – 104. doi:https://doi.org/10.1016/j.desal.2018.07.033.

[89] M. H. Sharqawy, M. A. Antar, S. M. Zubair, A. M. Elbashir, Optimum thermal design of humidification dehumidification desalination systems, Desalination 349 (2014) 10 – 21. doi:https://doi.org/10.1016/j.desal.2014.06.016.

[90] Dupont, Filmtec^{TM} reverse osmosis membranes technical manual (January 2020).

[91] A. Al-Zahrani, J. Orfi, Z. Al-Suhaibani, B. Salim, H. Al-Ansary, Thermodynamic analysis of a reverse osmosis desalination unit with energy recovery system, Procedia Engineering 33 (2012) 404 – 414, sWEE'11. doi:https://doi.org/10.1016/j.proeng.2012.01.1220.

[92] W. A. B. John A. Duffie, Flat-Plate Collectors, John Wiley & Sons, Ltd, 2013, Ch. 6, pp. 236–321. doi:10.1002/9781118671603.ch6.

[93] S. K. Hota, J. Perez, G. Diaz, Effect of geometric configuration and back plate addition in minichannel solar collectors, in: ASME 2018 International Mechanical Engineering Congress and Exposition, American Society of Mechanical Engineers Digital Collection, 2018, pp. IMECE2018–87852: 1–7.

[94] S. K. Hota, V. Duong, G. Diaz, Two-phase flow performance prediction for minichannel solar collectors, Heat and Mass Transfer 56 (2020) 109–120. doi:https://doi.org/10.1007/s00231-019-02686-y.

[95] T. W. Neises, S. A. Klein, D. T. Reindl, Development of a Thermal Model for Photovoltaic Modules and Analysis of NOCT Guidelines, Journal of Solar Energy Engineering 134 (1). doi:10.1115/1.4005340.

[96] G. M. Tina, S. Scrofani, Electrical and thermal model for pv module temperature evaluation, in: MELECON 2008 - The 14th IEEE Mediterranean Electrotechnical Conference, 2008, pp. 585–590. doi:10.1109/MELCON.2008.4618498.

[97] M. Hammami, S. Torretti, F. Grimaccia, G. Grandi, Thermal and performance analysis of a photovoltaic module with an integrated energy storage system, Applied Sciences 7 (11) (2017) 1107. doi:10.3390/app7111107.

[98] C. Elango, N. Gunasekaran, K. Sampathkumar, Thermal models of solar still—a comprehensive review, Renewable and Sustainable Energy Reviews 47 (2015) 856 – 911. doi:https://doi.org/10.1016/j.rser.2015.03.054.

[99] S. A. LAWRENCE, S. P. GUPTA, G. N. TIWARI, Experimental validation of thermal analysis of solar still with dye, International Journal of Solar Energy 6 (5) (1988) 291–305. doi:10.1080/01425918808914235.

[100] W. D. Soto, S. A. Klein, W. A. Beckman, Improvement and validation of a model for photovoltaic array performance, Solar Energy 80 (1) (2006) 78 – 88. doi:https://doi.org/10.1016/j.solener.2005.06.010.

[101] J. A. Miller, J. H. L. V, Impact of extraction on a humidification–dehumidification desalination system, Desalination 313 (2013) 87 – 96. doi:https://doi.org/10.1016/j.desal.2012.12.005.

[102] Y.-Y. Lu, Y.-D. Hu, X.-L. Zhang, L.-Y. Wu, Q.-Z. Liu, Optimum design of reverse osmosis system under different feed concentration and product specification, Journal of Membrane Science 287 (2) (2007) 219 – 229. doi:https://doi.org/10.1016/j.memsci.2006.10.037.

[103] J. A. Clark, The steady-state performance of a solar still, Solar Energy 44 (1) (1990) 43 – 49. doi:https://doi.org/10.1016/0038-092X(90)90025-8.

[104] A. Agrawal, R. S. Rana, P. K. Srivastava, Heat transfer coefficients and productivity of a single slope single basin solar still in indian climatic condition: Experimental and theoretical comparison, Resource-Efficient Technologies 3 (4) (2017) 466 – 482. doi:https://doi.org/10.1016/j.reffit.2017.05.003.

[105] WHO, Total dissolved solids in Drinking-water: Background document for development of WHO Guidelines for Drinking-water Quality (1996).

[106] E. Seybert, G. Petlin, K. Wu, M. Charles, Introduction to the California Net Energy Metering Ratepayer Impacts Evaluation, Tech. rep., California Public Energy Commission: Energy Division (October 2013).

[107] Weblink:, Net-Metering/Billing in Chile (2015).
URL `https://energypedia.info/wiki/Net-Metering_/_Billing_in_Chile`

[108] H. T. El-Dessouky, H. M. Ettouney, Chapter 10 - economic analysis of desalination processes, in: H. T. El-Dessouky, H. M. Ettouney (Eds.), Fundamentals of Salt Water Desalination, Elsevier Science B.V., Amsterdam, 2002, pp. 503 – 524. doi:https://doi.org/10.1016/B978-044450810-2/50012-9.

[109] EIA, Natural gas 1998: Issues and trends, Tech. Rep. DOE/EIA-0560(98), EIA: Office of Oil & Gas, U.S. Department of Energy, Washington, DC

(April 1999).
URL https://www.eia.gov/naturalgas/archive/056098.pdf

[110] M. Brander, G. Davis, Greenhouse gases, co_2, co_{2e}, and carbon: What do all these terms mean, Tech. rep., Econmetrica (August 2012).
URL https://ecometrica.com/assets/GHGs-CO2-CO2e-and-Carbon-What-Do-These-Mean-v2.1.pdf

[111] R. Semiat, Energy issues in desalination processes, Environmental Science & Technology 42 (22) (2008) 8193–8201, pMID: 19068794. doi:10.1021/es801330u.

[112] Y. Yang, M. Hagerty, A. Palmarozzo, M. Celebi, M. Chupka, H. Sheffield, The Future of Cap-and-Trade Program in California: Will Low GHG Prices Last Forever, Tech. rep., The Brattle Group (2017).

[113] M. Alhaj, S. G. Al-Ghamdi, Why is powering thermal desalination with concentrated solar power expensive? assessing economic feasibility and market commercialization barriers, Solar Energy 189 (2019) 480 – 490. doi:https://doi.org/10.1016/j.solener.2019.07.046.

[114] A. A. Madani, G. M. Zaki, Yield of solar stills with porous basins, Applied Energy 52 (2) (1995) 273 – 281, fifth Arab International Solar Energy Conference. doi:https://doi.org/10.1016/0306-2619(95)00044-S.

[115] S. Karki, K. R. Haapala, B. M. Fronk, Technical and economic feasibility of solar flat-plate collector thermal energy systems for small and medium manufacturers, Applied Energy 254 (2019) 113649. doi:https://doi.org/10.1016/j.apenergy.2019.113649.

[116] D. Trier, C. K. Skov, S. S. Sørensen, F. Bava, Solar District Heating Trends and Possibilities - Characteristis of Ground-Mounted Systems for Screening of Land Use Requirements and Feasibility, Tech. rep., SHC: Solar Heat and Energy Economics in Urban Environments (2018).

[117] Z. Tian, B. Perers, S. Furbo, J. Fan, Thermo-economic optimization of a hybrid solar district heating plant with flat plate collectors and parabolic trough collectors in series, Energy Conversion and Management 165 (2018) 92 – 101. doi:https://doi.org/10.1016/j.enconman.2018.03.034.

[118] D. Feldman, R. Margolis, Q2/Q3 2020 Solar Industry Update, Tech. rep., NREL (December 2020).

[119] A. M. Bilton, R. Wiesman, A. Arif, S. M. Zubair, S. Dubowsky, On the feasibility of community-scale photovoltaic-powered reverse osmosis desalination systems for remote locations, Renewable Energy 36 (12) (2011) 3246–3256. doi:https://doi.org/10.1016/j.renene.2011.03.040.

[120] G. D. P. da Silva, D. A. C. Branco, Modelling distributed photovoltaic system with and without battery storage: A case study in belem, northern brazil, Journal of Energy Storage 17 (2018) 11–19. doi:https://doi.org/10.1016/j.est.2018.02.009.

[121] J. F. Servert, E. Cerrajero, E. L. Fuentealba, Synergies of solar energy use in the desalination of seawater: A case study in northern chile, AIP Conference Proceedings 1734 (1) (2016) 140002. doi:10.1063/1.4949232.

[122] A. Malek, M. N. A. Hawlader, J. C. Ho, Design and economics of ro seawater desalination, Desalination 105 (3) (1996) 245 – 261. doi:https://doi.org/10.1016/0011-9164(96)00081-1.

[123] V. Belessiotis, S. Kalogirou, E. Delyannis, Chapter Three - Solar Distillation—Solar Stills, in: V. Belessiotis, S. Kalogirou, E. Delyannis (Eds.), Thermal Solar Desalination, Academic Press, 2016, pp. 103 – 190. doi:https://doi.org/10.1016/B978-0-12-809656-7.00003-9.

[124] R. E. Parkin, A note on the extinction coefficient and absorptivity of glass, Solar Energy 114 (2015) 196 – 197. doi:https://doi.org/10.1016/j.solener.2015.01.004.

[125] H. Zheng, Chapter 4 - Traditional Solar Desalination Units, in: H. Zheng (Ed.), Solar Energy Desalination Technology, Elsevier, Amsterdam, 2017, pp. 259 – 321. doi:https://doi.org/10.1016/B978-0-12-805411-6.00004-X.

[126] M. F. Ashby, Appendix A - Data for Engineering Materials, in: Materials Selection in Mechanical Design (Fourth Edition), fourth edition Edition, Butterworth-Heinemann, Oxford, 2011, pp. 495 – 523. doi:https://doi.org/10.1016/B978-1-85617-663-7.00018-7.

[127] S. Kumar, G. N. Tiwari, Life cycle cost analysis of single slope hybrid (pv/t) active solar still, Applied Energy 86 (10) (2009) 1995 – 2004. doi:https://doi.org/10.1016/j.apenergy.2009.03.005.

[128] A. B. Mande, P. Manickam, Enhanced solar still productivity using transparent walls with an integral trough and organic porous absorber ma-

terial, International Journal of Green Energy 16 (3) (2019) 211–227. doi:10.1080/15435075.2018.1549995.

[129] A. Kecebas, M. Kayfeci, Effect on optimum insulation thickness, cost and saving of storage design temperature in cold storage in Turkey, Energy Education Science and Technology Part A: Energy Science and Research 25 (2010) 117–127.

[130] Roman Kunič, Carbon footprint of thermal insulation materials in building envelopes, Energy Efficiency 10 (2017) 1511–1528. doi:https://doi.org/10.1007/s12053-017-9536-1.

[131] M. F. Alsayed, R. A. Tayeh, Life cycle cost analysis for determining optimal insulation thickness in palestinian buildings, Journal of Building Engineering 22 (2019) 101 – 112. doi:https://doi.org/10.1016/j.jobe.2018.11.018.

[132] S. Schiavoni, F. D'Alessandro, F. Bianchi, F. Asdrubali, Insulation materials for the building sector: A review and comparative analysis, Renewable and Sustainable Energy Reviews 62 (2016) 988 – 1011. doi:https://doi.org/10.1016/j.rser.2016.05.045.

[133] V. Annibaldi, F. Cucchiella, P. D. Berardinis, M. Rotilio, V. Stornelli, Environmental and economic benefits of optimal insulation thickness: A lifecycle cost analysis, Renewable and Sustainable Energy Reviews 116 (2019) 109441. doi:https://doi.org/10.1016/j.rser.2019.109441.

[134] M. Braulio-Gonzalo, M. D. Bovea, Environmental and cost performance of building's envelope insulation materials to reduce energy demand: Thickness optimisation, Energy and Buildings 150 (2017) 527 – 545. doi:https://doi.org/10.1016/j.enbuild.2017.06.005.

[135] C. Hill, A. Norton, J. Dibdiakova, A comparison of the environmental impacts of different categories of insulation materials, Energy and Buildings 162 (2018) 12 – 20. doi:https://doi.org/10.1016/j.enbuild.2017.12.009.

[136] D. Kumar, P. X. Zou, R. A. Memon, M. M. Alam, J. G. Sanjayan, S. Kumar, Life-cycle cost analysis of building wall and insulation materials, Journal of Building Physics 43 (5) (2020) 428–455. doi:10.1177/1744259119857749.

[137] A. Walther, A. K. Heidinger, Implementation of the Daytime Cloud Optical and Microphysical Properties Algorithm (DCOMP) in PATMOS-x, Journal of Applied Meteorology and Climatology 51 (7) (2012) 1371–1390. doi:10.1175/JAMC-D-11-0108.1.

[138] H. Al-Hinai, M. Al-Nassri, B. Jubran, Effect of climatic, design and operational parameters on the yield of a simple solar still, Energy Conversion and Management 43 (13) (2002) 1639–1650. doi:https://doi.org/10.1016/S0196-8904(01)00120-0.

[139] SAER-USA, SAER Heavy Duty Centrifugal Water Pump (2020).
URL https://www.pumpsupermarket.com/product/saer-usa-6bp7-109-1ph-threaded-centrifugal-pump-19200-gph-3-hp-3in-ports-230-volts/

[140] SAER-USA, SAER Heavy Duty Centrifugal Water Pump (2020).
URL https://www.pumpsupermarket.com/product/saer-usa-6bp4-110-threaded-centrifugal-pump-9480-gph-1-5-hp-2in-ports/

[141] M. Meratizaman, S. Monadizadeh, M. Tohidi Sardasht, M. Amidpour, Techno economic and environmental assessment of using gasification process in order to mitigate the emission in the available steam power cycle, Energy 83 (2015) 1 – 14. doi:https://doi.org/10.1016/j.energy.2015.01.112.

[142] S. of Michigan, Tanks Section UIP 11 (2003).
URL https://www.michigan.gov/documents/Vol2-35UIP11Tanks_121080_7.pdf

[143] U. W. C. TANKS, National Tank Outlet (2003).
URL https://www.ntotank.com/underground-water-tanks

[144] homewyse, Cost to Excavate Land (2020).
URL https://www.homewyse.com/services/cost_to_excavate_land.html

[145] U. S. P. Corp, HI-Temp CPVC Pipe Schedule 40 & 80 (2020).
URL https://www.usplastic.com/catalog/item.aspx?itemid=23484&catid=521

[146] K. E. Thomas, Overview of village scale, renewable energy powered desalination, Tech. Rep. NREL/TP-440-22083, National Renewable Energy Laboratory (4 1997). doi:10.2172/463614.

[147] G. Achari, M. H. I. Dore, A. Janzen, Towards equity in water pricing in small water systems: An alberta case study, International Journal of Water Resources and Environmental Engineering 10 (6) (2018) 64 – 75. doi:https://doi.org/10.5897/IJWREE2018.0786.

[148] J. J. Dooley, Bounding the marginal cost of producing potable water including the use of seawater desalinization as a backstop potable water production

technology, Tech. Rep. DE-AC05-76RL01830, U.S. Department of Energy (2014).

[149] V. B. Jensen, J. L. Darby, Brine disposal options for small systems in california's central valley, Journal AWWA 108 (5) (2016) E276–E289. doi:https://doi.org/10.5942/jawwa.2016.108.0045.

[150] J. Ziolkowska, R. Reyes, Chapter 3.1.3 - prospects for desalination in the united states—experiences from california, florida, and texas, in: J. R. Ziolkowska, J. M. Peterson (Eds.), Competition for Water Resources, Elsevier, 2017, pp. 298–316. doi:https://doi.org/10.1016/B978-0-12-803237-4.00017-3.

[151] M. Mickly, Review of concentrate management options, ground water report 363, technical papers, case studies and desalination technology resource, The Future of Desalination in Texas 2.

[152] M. C. Mickley, Membrane Concentrate Disposal: Practices and Regulations (Second Edition), Tech. rep., U.S. Department of the Interior Bureau of Reclamation (April 2006).

[153] R. A. Foldager, Economics of desalination concentrate disposal methods in inland regions: deep-well injection, evaporation ponds and salinity gradient solar ponds, Master's thesis, New Mexico State University (2003).

[154] P. Sahu, A comprehensive review of saline effluent disposal and treatment: conventional practices, emerging technologies, and future potential, Journal of Water Reuse and Desalination 911 (1) (2021) 33–65. doi:https://doi.org/10.2166/wrd.2020.065.

[155] Graham Juby and Adam Zacheis and Winnie Shih and Parameshwaran Ravishanker and Behrooz Mortazavi and Michael D. Nusser, Evaluation and Selection of Available Processes for a Zero-Liquid Discharge System for the Perris, California, Ground Water Basin, Tech. rep., U.S. Department of the Interior Bureau of Reclamation (April 2008).

[156] R. Dev, G. N. Tiwari, Characteristic equation of a passive solar still, Desalination 245 (1) (2009) 246 – 265, engineering with Membranes 2008. doi:https://doi.org/10.1016/j.desal.2008.07.011.

[157] A. Agarwal, R. S. Rana, Theoretical and experimental performance evaluation of single-slope single-basin solar still with

multiple v-shaped floating wicks, Heliyon 5 (2019) e01525. doi:https://doi.org/10.1016/j.heliyon.2019.e01525.

[158] V. Sivakumar, E. G. Sundaram, M. Sakthivel, Investigation on the effects of heat capacity on the theoretical analysis of single slope passive solar still, Desalination and Water Treatment 57 (20) (2016) 9190–9202. doi:10.1080/19443994.2015.1026284.

[159] A. Johnson, L. Mu, Y. H. Park, D. J. Valles, H. Wang, P. Xu, K. Kota, S. Kuravi, A thermal model for predicting the performance of a solar still with fresnel lens, Water 11 (9) (2019) 1860. doi:10.3390/w11091860.
URL `http://dx.doi.org/10.3390/w11091860`

[160] R. V. Dunkle, Solar Water Distillation, The Roof Type Solar Still and a Multi Effect Diffusion Still, in: A.S.M.E Proc. International Development in Heat Transfer, Vol. 5, 1961, pp. 895–902.

[161] M. Malik, G. N. Tiwari, A. Kumar, M. Sodha, Solar distillation: a practical study of a wide range of stills and their optimum design, construction, and performance, Pergamon press Oxford, 1982.

[162] Z. G. X. Chen, X. Sun, L. Bar, Y. X. Miao, Natural convection heat transfer across air layers at various angles of inclination, in: Engineering Thermophysics, 1984, pp. 211–220.

[163] R. S. Adhikari, A. Kumar, A. Kumar, Estimation of mass-transfer rates in solar stills, International Journal of Energy Research 14 (7) (1990) 737–744. doi:10.1002/er.4440140705.

[164] G. N. Tiwari, S. A. Lawrence, New heat and mass transfer relations for a solar still, Energy Conversion and Management 31 (2) (1991) 201 – 203. doi:https://doi.org/10.1016/0196-8904(91)90073-R.

[165] K. G. T. Hollands, T. E. Unny, G. D. Raithby, L. Konicek, Free Convective Heat Transfer Across Inclined Air Layers, Journal of Heat Transfer 98 (2) (1976) 189–193. doi:10.1115/1.3450517.

[166] S. Kumar, G. N. Tiwari, Estimation of convective mass transfer in solar distillation systems, Solar Energy 57 (6) (1996) 459 – 464. doi:https://doi.org/10.1016/S0038-092X(96)00122-3.

[167] M. Corcione, Effects of the thermal boundary conditions at the sidewalls upon natural convection in rectangular enclosures heated from below and

cooled from above, International Journal of Thermal Sciences 42 (2) (2003) 199 – 208. doi:https://doi.org/10.1016/S1290-0729(02)00019-4.

[168] N. Rahbar, J. A. Esfahani, Estimation of convective heat transfer coefficient in a single-slope solar still: a numerical study, Desalination and Water Treatment 50 (1-3) (2012) 387–396. doi:10.1080/19443994.2012.720442.

[169] P. T. Tsilingiris, The influence of binary mixture thermophysical properties in the analysis of heat and mass transfer processes in solar distillation systems, Solar Energy 81 (12) (2007) 1482 – 1491. doi:https://doi.org/10.1016/j.solener.2007.02.005.

[170] N. Setoodeh, R. Rahimi, A. Ameri, Modeling and determination of heat transfer coefficient in a basin solar still using cfd, Desalination 268 (1) (2011) 103 – 110. doi:https://doi.org/10.1016/j.desal.2010.10.004.

[171] G. N. Tiwari, A. Minocha, P. B. Sharma, M. E. Khan, Simulation of convective mass transfer in a solar distillation process, Energy Conversion and Management 38 (8) (1997) 761 – 770. doi:https://doi.org/10.1016/S0196-8904(96)00082-9.

[172] B. Jamil, N. Akhtar, Effect of specific height on the performance of a single slope solar still: An experimental study, Desalination 414 (2017) 73 – 88. doi:https://doi.org/10.1016/j.desal.2017.03.036.

[173] T. L. Bergman, A. S. Lavine, F. P. Incropera, D. P. Dewitt, Chapter 6 - introduction to convection, in: Fundamentals of Heat and Mass Transfer, John Wiley & Sons, Ltd, 2011, pp. 377–417.

[174] A. T. Shawaqfeh, M. M. Farid, New development in the theory of heat and mass transfer in solar stills, Solar Energy 55 (6) (1995) 527 – 535. doi:https://doi.org/10.1016/0038-092X(95)00069-4.

[175] Z. Hongfei, Z. Xiaoyan, Z. Jing, W. Yuyuan, A group of improved heat and mass transfer correlations in solar stills, Energy Conversion and Management 43 (18) (2002) 2469 – 2478. doi:https://doi.org/10.1016/S0196-8904(01)00185-6.

[176] M. E. V. da Silva, K. Schwarzer, B. Hoffschmidt, F. P. Rodrigues, T. Schwarzer, P. A. C. Rocha, Mass transfer correlation for evaporation–condensation thermal process in the range of 70 °c–95 °c, Renewable Energy 53 (2013) 174 – 179. doi:https://doi.org/10.1016/j.renene.2012.11.010.

[177] D. Wang, I. C. Gauld, G. L. Yoder, L. J. Ott, G. F. Flanagan, M. W. Francis, E. L. Popov, J. J. Carbajo, P. K. Jain, J. C. Wagner, J. C. Gehin, Study of fukushima daiichi nuclear power station unit 4 spent-fuel pool, Nuclear Technology 180 (2) (2012) 205–215. doi:10.13182/NT12-A14634.

[178] N. Kumar, J. H. Arakeri, Natural convection driven evaporation from a water surface, Procedia IUTAM 15 (2015) 108 – 115, iUTAM Symposium on Multiphase Flows with Phase Change: Challenges and Opportunities. doi:https://doi.org/10.1016/j.piutam.2015.04.016.

[179] A. E. Kabeel, Z. M. Omara, F. A. Essa, Enhancement of modified solar still integrated with external condenser using nanofluids: An experimental approach, Energy Conversion and Management 78 (2014) 493 – 498. doi:https://doi.org/10.1016/j.enconman.2013.11.013.

[180] A. K. Tiwari, G. N. Tiwari, Thermal modeling based on solar fraction and experimental study of the annual and seasonal performance of a single slope passive solar still: The effect of water depths, Desalination 207 (1) (2007) 184 – 204. doi:https://doi.org/10.1016/j.desal.2006.07.011.

[181] A. K. Tiwari, G. N. Tiwari, Annual performance analysis and thermal modelling of passive solar still for different inclinations of condensing cover, International Journal of Energy Research 31 (14) (2007) 1358–1382. doi:10.1002/er.1309.

[182] S. Kumar, A. Tiwari, Design, fabrication and performance of a hybrid photovoltaic/thermal (pv/t) active solar still, Energy Conversion and Management 51 (6) (2010) 1219 – 1229. doi:https://doi.org/10.1016/j.enconman.2009.12.033.

[183] R. G. Raluy, L. Serra, J. Uche, Life cycle assessment of desalination technologies integrated with renewable energies, Desalination 183 (1) (2005) 81 – 93, desalination and the Environment. doi:https://doi.org/10.1016/j.desal.2005.04.023.

Appendix A

Convective heat and mass transfer correlations of a solar still

Several correlations have been proposed in the literature for predicting the convective heat transfer rate and evaporation rate between the evaporating water and the condensing cover, and thereby, the distillate production rate in a solar still. Some of these correlations were empirically obtained, while some of them are curve fitted from experiments or computational fluid dynamics (CFD) simulations. Twelve convective heat transfer correlations, and twelve mass transfer correlations were selected, and all possible combinations were investigated to determine the best possible set of correlations to predict the data. Several experimental data from different sources in the depth range of 1-10 cm were selected and compared.

A.1 Modeling criteria

For estimating distillate productivity of a solar still, several geometrical, ambient and operational inputs are to be provided. A representation of these inputs, and the measured outputs is shown in Fig. A.1.

The inputs given to the solar still model are:

1. Geometrical information: solar still basin size (l, w), tilt (θ) of the cover, distance between cover and basin (height of the solar still) (h) or aspect ratio $(AR = \frac{w}{h})$.

2. Ambient data: Solar irradiation (hourly average) (I), ambient temperature (T_{amb}), wind velocity (u).

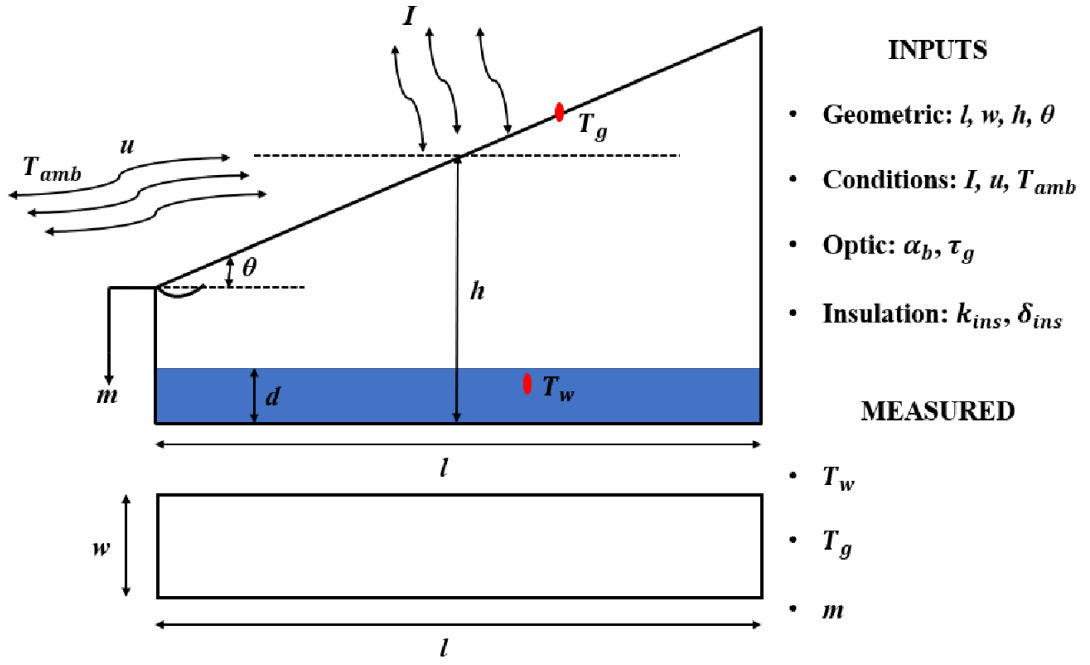

Figure A.1: Representation of input data and measurable outputs for estimating the distillate productivity of a solar still

3. Optical properties: Reflectivity (ρ) and absorptivity (α) of the cover (subscript: g) and basin (subscript: b).

4. Insulation: thickness (δ_{ins}) and thermal conductivity (k_{ins}) if applicable.

The measurable outputs are the basin fluid temperature (T_w), cover temperature (T_g), and distillate production rate (m). Distillate production rate is a function of temperature difference between the basin fluid and the cover temperature: as

$$m = f(\Delta T)^n \tag{A.1}$$

Where, n is typically close of 0.25 for low temperatures and $n = 1/3$ for higher temperatures. For the experimental data chosen for comparing the correlations, major emphasis is placed on the availability of above mentioned input parameters. It can also be mentioned that, even if basin absorptivity is not mentioned, the values are usually around 0.8-0.95. Also, the glass cover thickness is about 3-4 mm and the cover absorptivity and reflectivity are assumed to be 5% each, as is widely found in the literature [156, 157, 104, 158, 159]. Uniform cover temperature is assumed in modeling because the contribution of the glass thermal conductivity

in the overall heat transfer process is very low. For example, if a 4 mm glass with a thermal conductivity of 0.8 W/m-K is used in the solar still, and at any given time and a maximum of 10% of the solar energy at 1 sun (1 kW/m^2) condition is used in conducting heat through the glass, then the temperature difference calculated between the outer glass surface and the inner glass surface is only 0.5°C. The temperature difference between inner glass cover and the outer glass cover observed in these studies typically vary between 0.2-1 °C. The governing equations solved are already mentioned in Chapter 5.

A.2 Convective heat and mass transfer correlations

Twelve convective heat transfer and twelve mass transfer correlations are chosen. To reduce complexity and confusion, the nomenclature is assigned to each of these correlations.

A.2.1 Convective heat transfer correlations

The methodology followed in convection heat transfer is by recognizing the use of dimensionless numbers such as Rayleighs number (Ra), Grashoff number (Gr), Prandtl number (Pr), and Nusselt number (Nu). The definitions and significance of these dimensionless numbers is well reported in the literature. The convective heat transfer coefficient is a direct function of Nusselt number, as $h_{conv} = \frac{Nuk_v}{h}$. A modified temperature difference between the evaporating water pool and condensing cover is used to account for the influence of vapor difference concentration [125], and is given as:

$$\Delta T' = (T_w - T_g) + \frac{(P_w - P_g)T_w K}{\frac{M_a P_{tot}}{M_a - M_w} - P_w} \tag{A.2}$$

Where, P is the vapor pressure, M_a is the molar mass of dry air, and M_w is the molar mass of water. Some of these correlations approximate the term $\frac{M_a P_{tot}}{M_a - M_w}$ to 268900 Pa. It is noted that the modified temperature is difference is dominated by this vapor difference gradient term, especially at high temperature differences. Often the Nusselt number is given as:

$$Ra = Gr * Pr \tag{A.3a}$$

$$Nu = C(Ra)^n \tag{A.3b}$$

Where, C, n are constants, typically derived by experimental regression analysis. The convective heat transfer correlations and their corresponding nomenclature in this work is shown in Table A.1.

Table A.1: Convection heat transfer (h_{cwg}) correlations

Nomenclature	Correlation	Source
C1	$Nu = 0.075(Ra)^{1/3}$ *	[160]
C2	if $10^4 < Gr < 3.2 * 10^5$, then, $C = 0.21, n = 0.25$ else if $3.2 * 10^5 < Gr < 10^7$, then, $C = 0.075, n = 1/3$	[161]
C3	$Nu = 0.26(Ra)^(0.26)$	[162]
C4	if $10^4 < Gr < 2.51 * 10^5$, then, $C = 0.21, n = 0.25$ else if $2.51 * 10^5 < Gr < 10^7$, then, $C = 0.1255, n = 1/3$	[163]
C5	$Nu = 1 + 1.44\left[1 - \frac{1708sin(1.8\beta)^{1.6}}{Racos(\beta)}\right]\left[1 - \frac{1708}{Racos(\beta)}\right]^{+} + \left[(\frac{Racos(\beta)}{5830})^{1/3} - 1\right]^{+}$	[164, 165]
C6	if $1.794 * 10^6 < Gr < 5.724 * 10^6$, then, $C = 0.0322, n = 0.414$	[166]
C7	if $0.66 < AR < 8$, & if $10^3 < Ra < 10^6$, then, $Nu = 0.21AR^{0.09}Ra^{0.25}$	[167]
C8	if $2.5 < AR < 5.5$, & if $5 * 10^6 < Ra < 5 * 10^7$, then, $Nu = 0.28AR^{-0.16}Ra^{0.25}$	[168]
C9	$h_{cwg} = Ck_m(\frac{g\rho_m\beta}{\mu_m\alpha_m})\left[(T_w - T_g) + \frac{T_{wK}(P_w - P_g)(M_a - M_w)}{M_aP_{tot} - P_w(M_a - M_w)}\right]^{1/3}$	[169]
C10	$C = 2.054, n = 0.166$	[170]
C11	if $2 < AR < 10$, & $Ra > 3 * 10^5$, then, $Nu = 0.075\left[\frac{Ra(1+cos(\theta))}{2}\right]^{1/3}$	[171]
C12	if $1.94 < AR < 2.67$, & $10^7 < Ra < 10^11$, then, $Nu = 0.0462AR^{0.15}Ra^{0.34}$	[172]

* Dry air properties

If the conditions are not satisfied, then default C1 correlation is adopted due to its wide usage.

A.2.2 Evaporation mass transfer coefficient

Evaporation mass transfer coefficient is estimated with an approach similar to the convective heat transfer coefficient, by making use of mass transfer dimensionless numbers, such as Grashoff number (Gr), Schmidt number (Sc) and Serwood number (Sh). A similarity concept between the two can be applied as [173]:

$$\frac{Nu}{Pr} = \frac{Sh}{Sc} \tag{A.4}$$

The evaporation heat transfer coefficient considered here, and their respective nomenclature is shown in Table A.2.

Table A.2: Evaporation heat transfer (h_{cwg}) correlations

Nomenclature	**Correlation**	**Source**
E1	$h_{ewg} = 0.0163 h_{cwg} \frac{P_w - P_g}{T_w - T_g}$	[160]
E2	$h_{ewg} = 0.013 h_{cwg} \frac{P_w - P_g}{T_w - T_g}$	[161]
E3	$h_{ewg} = 0.008 h_{cwg} \frac{P_w - P_g}{T_w - T_g}$	[103]
E4	$h_{ewg} = h_{cwg} \frac{M_w h_{fg}}{2 M_{a,v} C_{pv}} \left[\frac{1}{P_{aw}} + \frac{1}{P_{ag}} \right]$	[174]
E5	$h_{ewg} = h_{cwg} \frac{M_w h_{fg}}{M_{mix} C_{p,mix}} \left[\frac{1}{P_{LMTD}} \right] Le^{-2/3}$	[174]
E6	$h_{ewg} = h_{fg} \alpha \Delta T' \frac{P_w - P_g}{T_w - T_g}$	[163]
E7	if $10^3 < Ra < 10^6$, & $35°C < T_w < 86°C$, then,	[175]
E8	$h_{ewg} = h_{cwg} \frac{1}{\rho_v C_{p,v} Le^{-0.74}}$ $h_{ewg} = h_{cwg} \frac{h_{fg}}{C_{pa}} \frac{R_a}{R_v} \frac{P_{tot}}{(P_{tot} - P_w)(P_{tot} - P_g)}$	[169]
E9	if $70°C < T_w < 95°C$, then $Sh = 0.2017 Gr^{0.1072} Sc^{4.9736}$	[176]
E10	$Sh = 0.15 \left(\left[Gr + Gr_m \right] Sc \right)^{1/3}$	[177]
E11	$Sh = 0.26 Ra^{0.306}$	[178]
E12	$h_{ewg} = h_{cwg} \left(4.23 * 10^{-5} * T_i^3 + 2.5 * 10^{-4} * T_i^2 + 0.058 * T_i + 0.035 \right)$	[168]

The basin fluid absorptivity depends on the depth of solar light penetration. The attenuation estimated for 2cm, 4 cm, 6 cm, 8 cm and 10 cm is 0.3244, 0.3815, 0.4145, 0.4352 and 0.4508, respectively, based on the absorption coefficient of water. The experimental data selected for the water depth between 1 cm and 10 cm used for validation of these correlations are shown in Table A.3.

Table A.3: Experimental data selected for validating correlations

depth (cm)	**source**
1	[20, 179]
2	[157, 180]
4	[104, 181]
5	[182]
6	[104]
8	[104]
10	[104, 182]

The comparative plots of experimental measurements (Expt) and their corresponding predicted results (Pred) for the best correlations with the lowest mean absolute error (MAE = $\frac{|\text{Pred}-\text{Expt}|}{\text{Expt}} \times 100\%$) is shown in Table A.4.

Table A.4: Experimental vs predicted output measurements

Mass evaporation rate (kg/m^2-h)	**Water temperature (T_w)**	**Glass temperature (T_g)**
1 cm depth		
C5E2 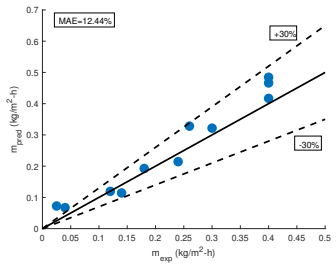	C10E11 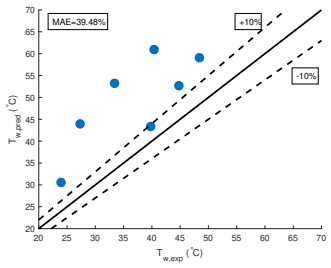	- -
C5E11 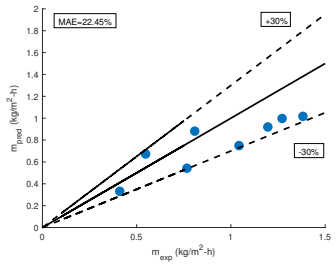	C10E9 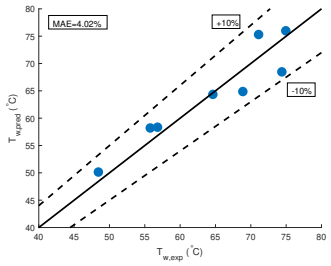	C5E8 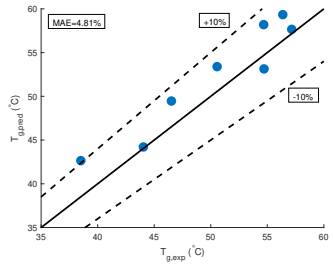
2 cm depth		
C4E9 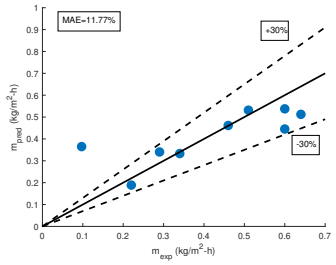	C10E11 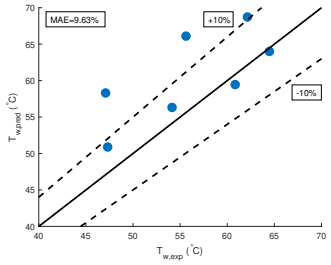	C5E3 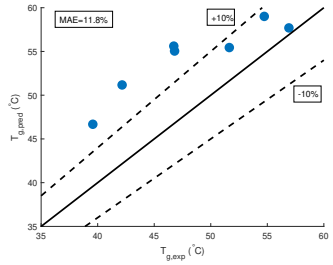
C4E3	C10E11	C5E3

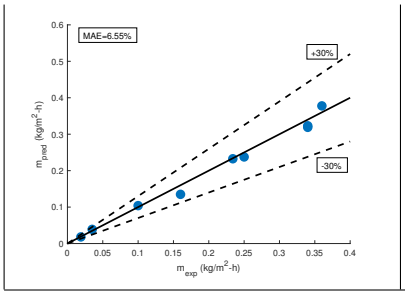

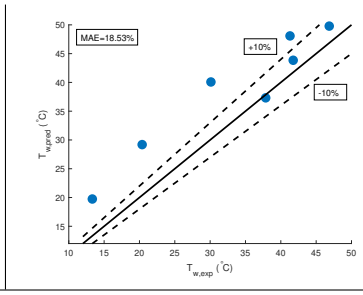

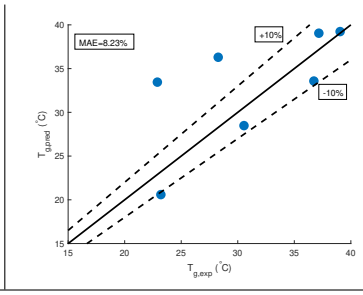

C10E3

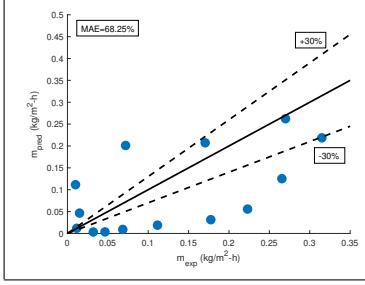

C9E8

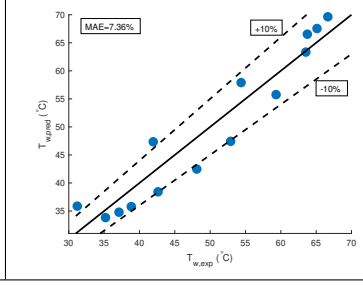

C10E11

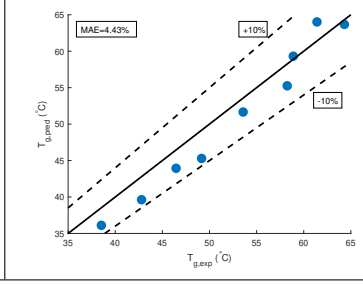

4 cm depth

C1E3

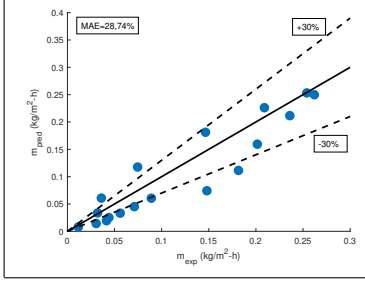

C1E11

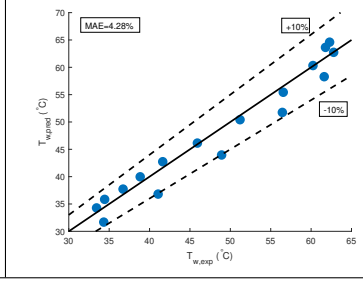

C5E3

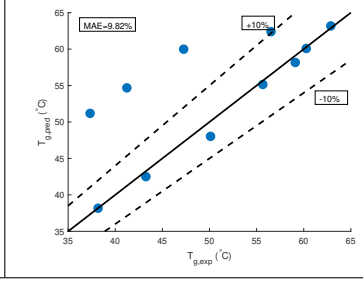

C4E7

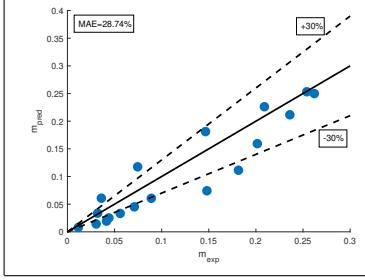

C8E3

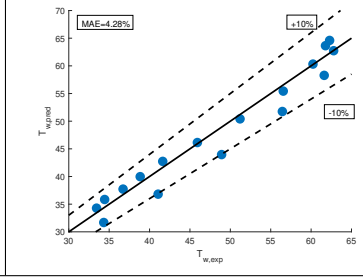

C9E1

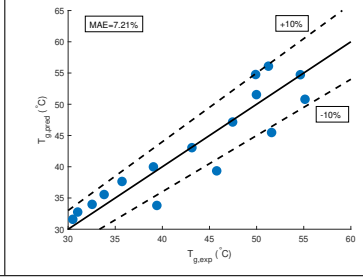

5 cm depth

C8E3 | C5E3 | C8E11

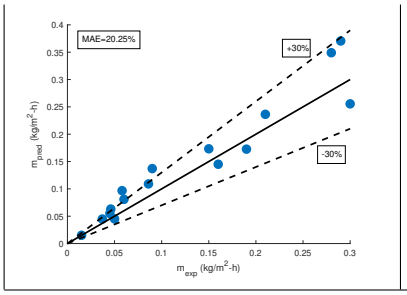

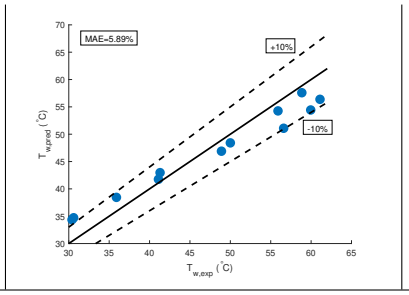

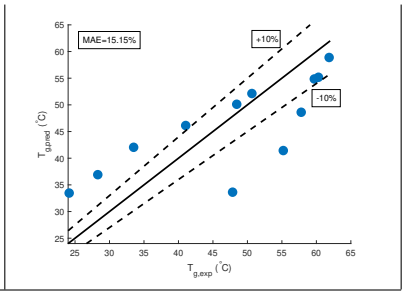

6 cm depth

C8E3

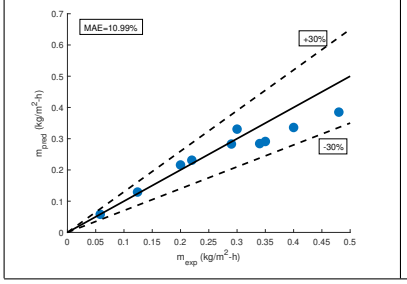

C10E11

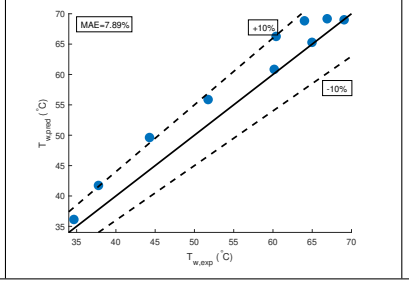

C5E1

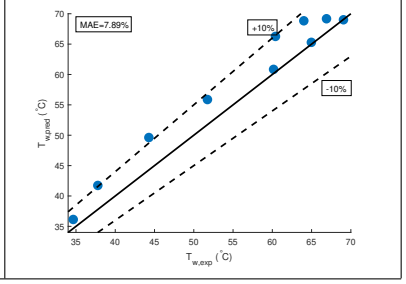

8 cm depth

C2E3

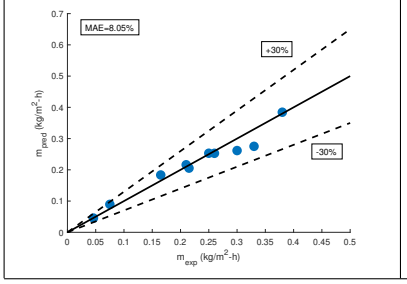

C10E11

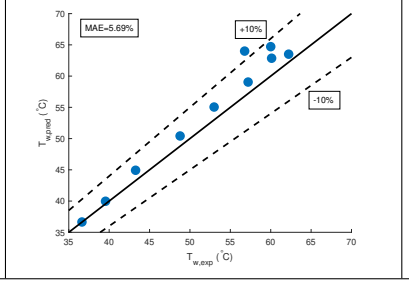

C1E6

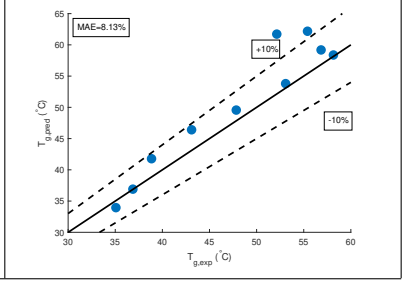

10 cm depth

C8E3

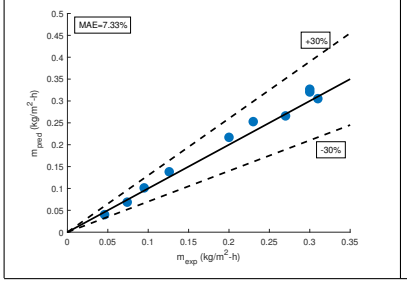

C10E6

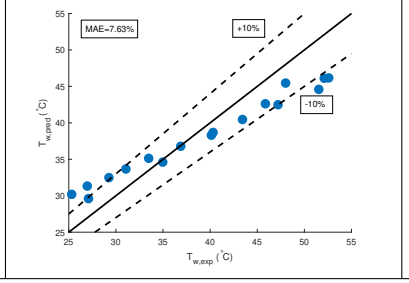

C9E9

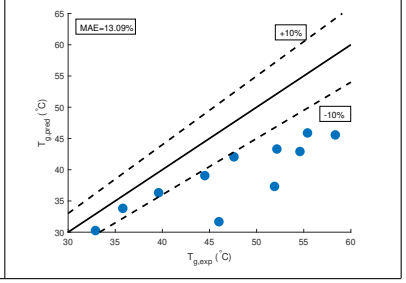

C6E3 C10E11 C5E4

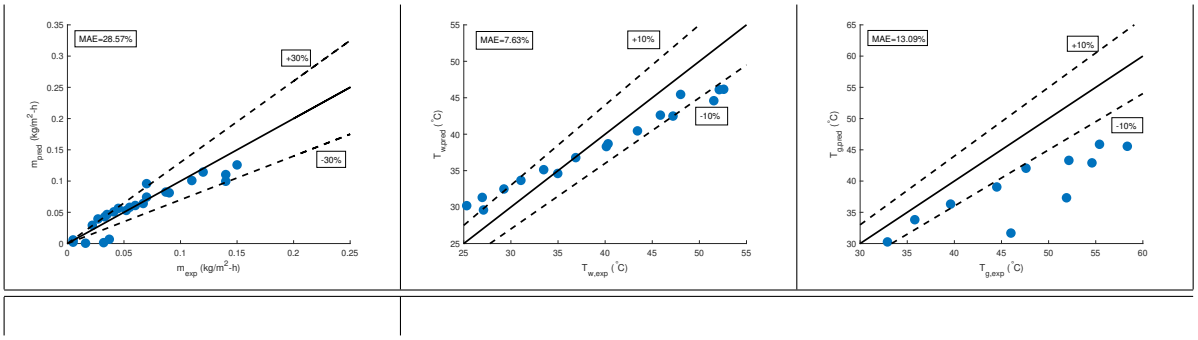
MAE=28.57%
+30%
-30%
m_{pred} (kg/m^2-h)
m_{exp} (kg/m^2-h)
MAE=7.63%
+10%
-10%
$T_{w,pred}$ (°C)
$T_{w,exp}$ (°C)
MAE=13.09%
+10%
-10%
$T_{g,pred}$ (°C)
$T_{g,exp}$ (°C)

Appendix B

Life cycle assessment of a low-cost solar still

One of the key aspects of a solar stills is that they are environmentally friendly. However, the production and end-of-life processing of a solar still systems have associated environmental impacts. A cradle-to-grave life cycle assessment is carried out for the solar still system, for the configuration shown in Fig. 6.6. The low-cost solar still materials are: sodalime glass as condensing cover, galvanized iron (steel) sheet (GS/GI sheet) as the basin, rock wool insulation and concrete as the solar still body. It is shown in Table 6.1 that this combination yields a low-cost solar still with energy payback time of only 0.25 years. Energy payback time includes only the embodied energy of the solar still materials.

B.1 System boundary and methods

Figure B.1 shows the system boundary for the cradle-to-grave assessment of the solar still desalination system. Along with solar still materials, impacts of production of plywood overhead tank, polyethylene underground storage tank, transportation impacts, and end-of-life impacts of components are included. In addition, impacts of electricity consumption for water pumping and excavation are considered, while pumps and piping are excluded with the assumption that they are part of city water supply line and provided by the local administration. Greenhouse gas emissions (climate change) impacts measured in terms of kg $CO_{2\text{-eq}}$ (indicator units) for these processes are characterized by EPA TRACI 2.1 methods and extracted from SimaPro software. The chosen functional unit for normalizing the impacts is 1 m^3 of freshwater produced.

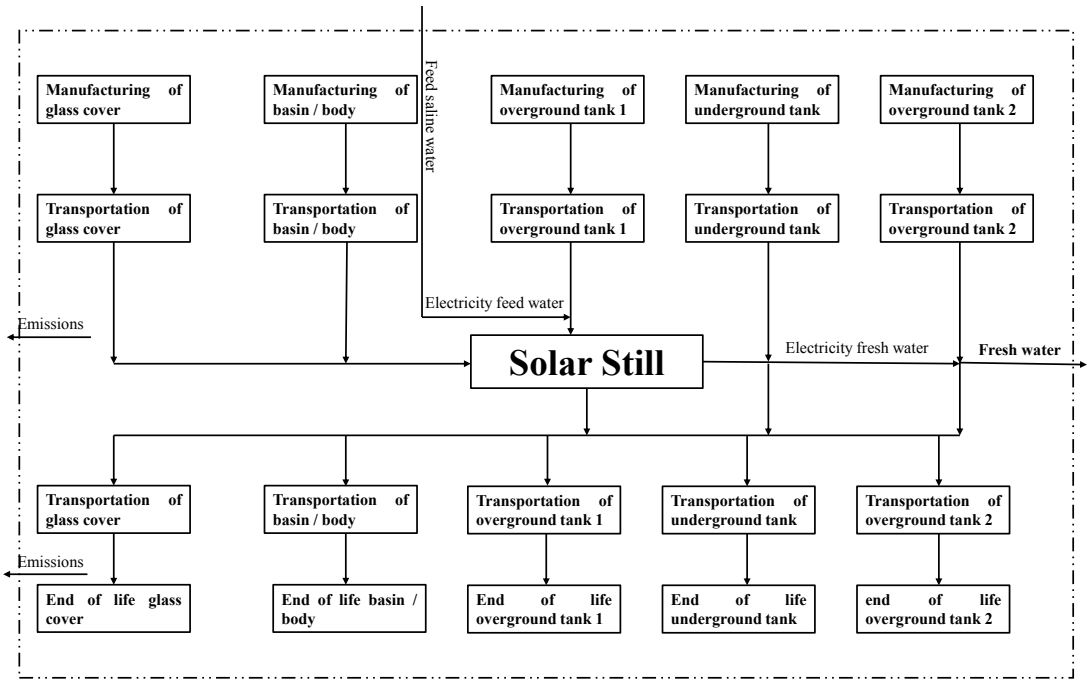

Figure B.1: Cradle-to-grave system boundary of solar still desalination system

B.2 Results and discussions

Figure B.2 shows the baseline life cycle impacts of the solar still system for water productivity rate of 28.9 m^3/day, which is the estimated median for the state of California shown in Fig. 6.5 (a). It is observed that the total life cycle climate change impacts are 1.33 kg $CO_{2\text{-eq}}/m^3$ of freshwater produced. Manufacturing of the glass and the basin contribute to almost 59% of the total impacts, and the share of concrete transportation is 10% for both manufacturing to installation site and installation site to end of life management combined. The other processes contribute to the rest 31% of the impacts.

Parametric sensitivity analysis and Monte-Carlo uncertainty analysis are performed and are shown in Fig. B.3. It is observed that plant life has the highest influence in the total life cycle greenhouse gas emissions impacts from the system. These solar still materials can be expected to last at least 40 years, and it is assumed that the tanks can also last the said time. Since the process of desalination is emission free, for a 40 year solar still system life, more aggregate freshwater is produced, and thus, the life cycle greenhouse gas impacts are lower. The corre-

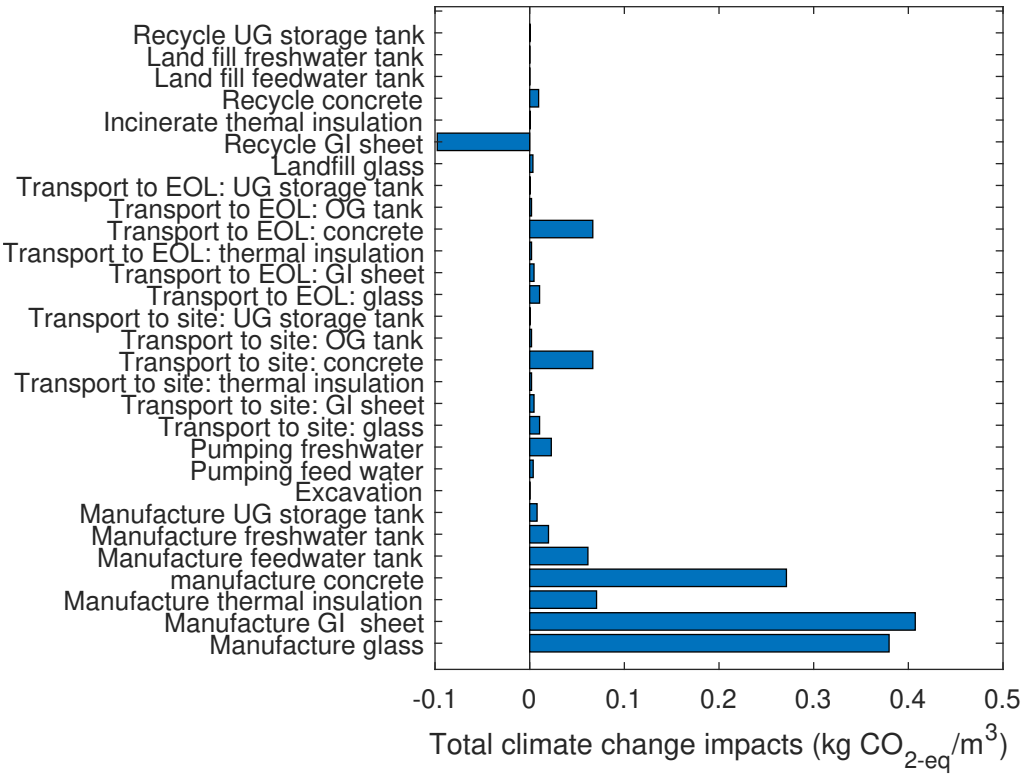

Figure B.2: Baseline Life cycle impacts of solar still system

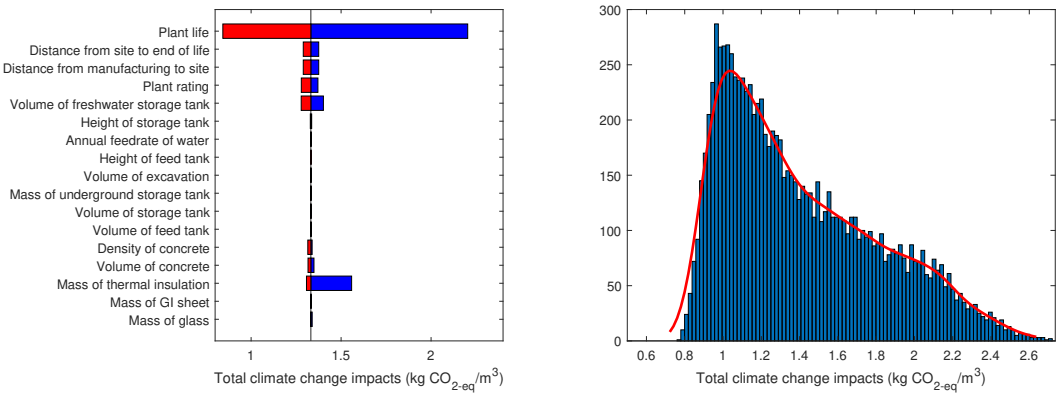

Figure B.3: (a) Sensitivity analysis of parametric variation of the solar still system, (b) Monte-Carlo uncertainty analysis of the solar still system

sponding life cycle impacts are only 0.84 kg $CO_{2\text{-eq}}/m^3$ of freshwater produced. The highest impacts are associated with a plant life of 15 years, and is 2.20 kg $CO_{2\text{-eq}}/m^3$. The cumulative probability that the emissions are lower than 1 kg $CO_{2\text{-eq}}/m^3$ is 16.2%. Very few published works exist on life cycle impacts of desalination for small scale productivity. A highly mature PV-RO system has impacts of 1.53 kg $CO_{2\text{-eq}}/m^3$ (0.9 kg CO_2/m^3 + 2.10 g NO_x/m^3, without accounting for VOC's and SO_x emissions), and a solar thermal powered multi stage flash system producing 45550 m^3/day freshwater has total life cycle greenhouse gas emissions impact of 13.84 kg $CO_{2\text{-eq}}/m^3$ (10.91 kg CO_2/m^3 + 9.82 g NO_x/m^3) [183].